Development of a combined transition and diffraction radiation station for non-invasive beam size monitoring on linear accelerators

Michele Bergamaschi

Department of Physics
Royal Holloway, University of London

A thesis submitted to the University of London for the degree of Doctor of Philosophy

October 2018

Declaration

I confirm that the work presented in this thesis is my own. Where information has been derived from other sources, I confirm that this has been indicated in the document.

Signed:

Date:

I dedicate this thesis to my wife Caterina and to my family

Abstract

Next generation linear colliders such as the Compact Linear Collider (CLIC) or the International Linear Collider (ILC) will accelerate particle beams with extremely small emittance. The high current and small size of the beam (micron-scale) due to such a small emittance require non-invasive, high-resolution techniques for beam diagnostics. Diffraction Radiation (DR), a polarization radiation that appears when a charged particle moves in the vicinity of a medium, is a promising candidate as it is non-invasive. Despite these advantages DR is used less than other techniques mainly due to a challenging target fabrication (micrometer scale slits production) and data extraction. The aim of this thesis is devoted to study the feasibility of an instrument based on DR and the limitation of this technique applied to high energy linear accelerators. Since DR is sensitive to beam parameters other than the transverse profile (e.g. its divergence and position), preparatory simulations have been performed with realistic beam parameters. A new dedicated instrument has been designed, installed and commissioned in the KEK Accelerator Test Facility (ATF2) beam line. At present DR has been observed in the visible wavelength range and in the ultraviolet (down to 250 nm) to optimize sensitivity to small beam sizes. Presented here are the latest results of these DR beam size measurements and simulations showing that this technique allows beams as small as a few microns to be measured.

Acknowledgements

First of all I would like to express my gratitude to my supervisor Dr Pavel Karataev. He encouraged and guided me throughout this study with constructive criticism and important advice without which this thesis work would have been impossible.

I must extend my gratitude to my supervisor at CERN, Dr Stefano Mazzoni for having supported and encouraged me in this project from the real beginning with his willingness to answer to all of my questions about particle accelerator, optics and every doubts I had.

I also would like to thank Dr Thibaut Lefevre for his inspiring ideas and suggestions he provided in every step of the realization of this project. I really appreciated that he led our discussion not only with determination to reach the goals but also with a great enthusiasm, an approach to research that I'll try to keep with me for the future. I also must thank Dr Robert Kieffer with whom I shared a lot of time in Japan at KEK to perform the experiment work. He made it possible to conduct this study not only by helping me but also by sharing with me his experimental experience teaching me a lot. I thank also all the other members of my section at CERN that helped me during these years.

I also would like to acknowledge all the members of the E-Jade collaboration working at ATF2 that shared with me a lot of time in Japan.

A really huge thank to my parents who made this great experience true, encouraging me to start this PhD experience far from home. If I managed to arrive here it's only thanks to you.

My greatest thanks goes to my wife Caterina for her support on every day of my PhD sharing with me the joys and encouraging me when I was facing difficulties. Most importantly I would like to thank her for never let me feel alone even if I was literally on the other side of the world.

Contents

List of Figures

List of Tables

Chapter 1

Introduction

The main aim of this thesis was to develop a combined transition and diffraction radiation station for non-invasive beam size monitoring for linear accelerators, specifically for the future generation of linear colliders. During this thesis work a combined Transition Radiation (TR) and Diffraction Radiation (DR) monitor has been designed, installed and tested on Accelerator Test Facility 2 beam line at KEK. This accelerator is, indeed, a test facility for future linear colliders providing a small emittance beam that can be focused to sub-micrometre beam sizes challenging present technologies in terms of transverse beam size measurements.

To show the motivation of this thesis work, Chapter 1 introduces the need of such instruments for future linear colliders, such as CLIC. A comparison with other techniques used in instrumentation for particle accelerators is also shown. A comprehensive and detailed overview of TR and DR, where the theoretical aspect of these polarization radiations are described with the specific perspective of beam diagnostics is then presented in Chapter 2. Preparatory calculations, simulation and experiments (such as the study of TR interference in section 2.1.5) performed are also presented. The design and the commissioning of the experimental apparatus developed during this thesis work is given in Chapter 3. Finally, the discussion and the analysis of the experimental data acquired and processed throughout the PhD research is presented in detail in Chapter 4.

1.1 CLIC - Compact Linear Collider

The energy frontier of physics exploration has been pushed forward in the last decades by particle accelerators. One clear example is the Large Hadron Collider (LHC) [1] that has contributed to the verification of the Standard Model and the discovery of the Higgs boson [2]. However, higher energy collisions are needed to study physics beyond the Standard Model. The particle physics community worldwide has expressed a consensus that the results of the LHC need to be complemented by experiments that make use of cleaner collisions could be observed using fundamental particles [3]. A lepton collider in the TeV energy range makes possible the investigation of new physics beyond the Standard Model probing the energy range of the lightest supersymmetric particles, the primary candidates for dark matter and for the testing of the existence of extra dimensions.

One candidate for the next generation multi-TeV electron-positron collider is the Compact Linear Collider (CLIC) [3]. The proposed layout for the accelerator complex designed to provide collisions with a centre-of-mass energy of 3 TeV and a luminosity of $2 \times 10^{34}\, cm^{-2} s^{-1}$ is shown in Figure 1.1. The injection linacs generate and pre-accelerate the Main Beams (MB) which then enter the Damping Rings for emittance reduction. At the exit of the injector complex the desired normalised beam emittances are $500\, nm$ and $5\, nm$ in the horizontal and vertical planes respectively (Table 1.1). The MB are further accelerated in a common booster linac before being transported through the main tunnel to the turnarounds. After this, two main beam linacs with a combined length exceeding 40 km accelerate the MB with an accelerating gradient of $100\, MV/m$ (Table 1.1). An innovative two-beam acceleration scheme is applied in these linacs: the MB are accelerated using a sophisticated approach where RF power typically generated by klystrons is replaced by a Drive Beam (DB). The power to accelerate the MB is extracted from the DB and converted to RF power in special RF devices called PETS (Power Extraction and Transfer Structures). In the 3 TeV layout CLIC is divided into sectors on average $878\, m$ long (Fig. 1.1), each with about 3000 accelerating structures. The Drive Beam consists of bunch trains, each train supplying one sector with RF power. These trains have relatively low energy, 2.4 GeV, but high peak current of about 100 A for a pulse. About 84% of their stored energy is converted to RF power, after which they are dumped at the end of the sector. At this point a new DB bunch train arrives to supply the following main linac section. [3].

The next generation of accelerators, e.g. CLIC, are designed to operate with high charge density beams and transverse beam sizes on the micron-scale (see Table 1.2). This is necessary to achieve high luminosity collisions. In fact the beam after the accelerating sections is finally squeezed down to a few nanometres in the vertical direction and delivered

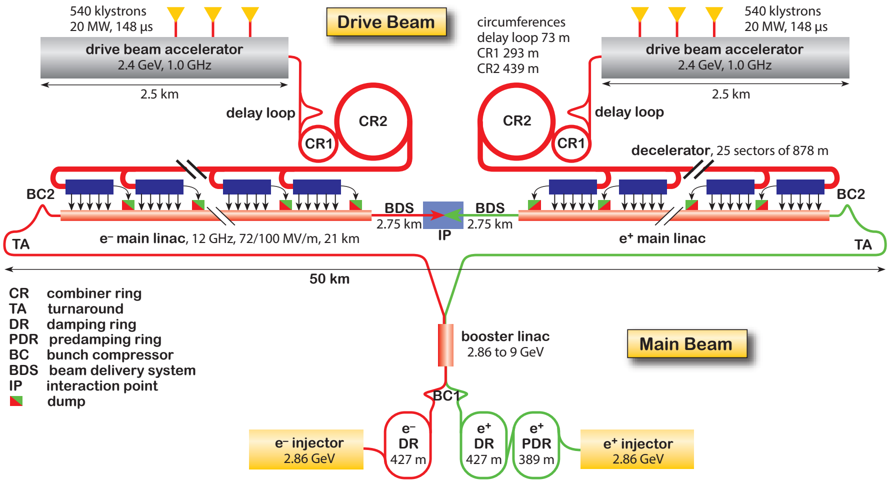

Figure 1.1: CLIC 3 TeV layout: The upper part of the figure shows the Drive Beam generation in two linacs and the successive time compression of the Drive Beam pulses in the Delay Loops and Combiner Rings (CR1 and CR2). This compressed Drive Beam is transported through the Main Linac tunnel to 25 individual turnarounds. The lower part of the figure shows the electron and positron injectors of the Main Beam and the transport lines of the Main Beam to the Main Linac tunnel. The beams collide after a long Beam Delivery Section (BDS) (collimation and final focus) in one interaction point (IP) in the centre of the complex [3].

to the interaction region. The luminosity of two colliding beams can be expressed by the following equation:

$$\mathcal{L} = \frac{\mathrm{N_p^2 n_b f_{rep}}}{\mathrm{A}} \mathrm{H_D}, \tag{1.1}$$

where $\mathrm{N_p}$ is the number of particles per bunch, $\mathrm{n_b}$ is the number of bunches per train, $\mathrm{f_{rep}}$ is the repetition frequency of the trains, A is the effective overlap area of the colliding beams at the interaction point (IP) and $\mathrm{H_D}$ is the overall luminosity enhancement factor [6]. This parameter represents the combined effect of the hour-glass (i.e. the change of beta function in longitudinal direction over the collision region) and the disruption enhancement (due to the attractive force that the two colliding bunches exert on each other) [3,7]. Therefore the transverse beam dimensions must be monitored at every stage of the beam production, acceleration and delivery. Assuming Gaussian bunch distributions and head-on collisions, Eq. (1.1) becomes

$$\mathcal{L} = \frac{\mathrm{N_p^2 n_b f_{rep}}}{4\pi\sigma_\mathrm{x}^*\sigma_\mathrm{y}^*} \mathrm{H_D}, \tag{1.2}$$

where σ_x^* and σ_y^* are the horizontal and vertical beam sizes of the bunch and * denotes the parameters at the IP. One can see that the luminosity can be increased by reducing

Table 1.1: Parameters for the CLIC energy stages [4,5].

Parameter	**Symbol**	**Stage 1**	**Stage 2**	**Stage 3**
Centre-of-mass energy	$\sqrt{\mathrm{s}}\ [GeV]$	380	1500	3000
Repetition frequency	$\mathrm{f}_{\mathrm{rep}}\ [Hz]$	50	50	50
Number of bunches per train	n_{b}	352	312	312
Bunch separation	$\Delta\,\mathrm{t}\ [ns]$	0.5	0.5	0.5
Accelerating gradient	$\mathrm{G}\ [MV/m]$	72	72/100	72/100
Total luminosity	$\mathcal{L}\ [10^{34}\frac{1}{cm^2 s}]$	1.5	3.7	5.9
Main tunnel length	$[km]$	11.4	29.0	50.1
Number of particles per bunch	$\mathrm{N}_{\mathrm{b}}\ [10^9]$	5.2	3.7	3.7
Bunch length	$\sigma_{\mathrm{z}}\ [\mu m]$	70	44	44
IP beam size	$\sigma_{\mathrm{x}}/\sigma_{\mathrm{y}}\ [nm]$	149/2.9	$\sim$ 60/1.5	$\sim$ 40/1
Norm. emitt. (at IP)	$\epsilon_{\mathrm{x}}/\epsilon_{\mathrm{y}}\ [nm]$	900/20	660/20	660/20
Estimated power consumption	$\mathrm{P}_{\mathrm{wall}}\ [MW]$	252	364	589

the transverse beam sizes at the IP.

Requiring high luminosity, not easy to achieve in a linear machine compared to a circular machine due to a lower repetition rate, CLIC is the most challenging project of a lepton accelerator. Due to its demanding requirement in terms of beam charge, repetition rate and beam size any diagnostics developed for this accelerator could be then scaled down and adapted for other machines.

1.2 Beam size diagnostic

Table 1.2 shows an overview of the requirements for transverse profile monitoring. It presents the evolution of the beam size through the CLIC complex with the corresponding expected charge density. The beam energy is also indicated as it may influence the choice of detector technology. The charge densities are mentioned, as they will set an upper limit above which intercepting devices like screens or wire scanners would get damaged. For best thermal-resistant materials like Carbon, Beryllium or Silicon Carbide, the limit corresponds to charge density of $10^6\ nC/cm^2$ [8]. This number refers to the survival of material to single shot pulse, and does not take into account the heat dissipation effects that would need to be considered in the final design (repetition rate of the machine, cooling of the material, etc.). This implies that they can not be used with full beam already after the injector linac where the charge density increase significantly (Table 1.2).

The measurement of the beam size gives a direct measure of the transverse beam emittance. For ultra-relativistic beam energy, it is routinely deducted using either the

Table 1.2: Transverse beam size requirements for CLIC (where MDI is the Machine Detector Interface and RTML is the Ring To Main Linac) [3]

Sub-system	**Energy** [GeV]	**Resolution** [μm]	**Charge density** [nC/cm^2]
	Main Beam		
e^- source & pre-injector complex	0.2	50	$< 5 \times 10^5$
e^+ source & pre-injector complex	0.2	50	$< 5 \times 10^5$
Injector linac (e^-/e^+)	2.86	50	$< 5 \times 10^5$
Pre-Damping Rings (H/V)	2.86	50/10	$< 5 \times 10^6$
Damping Rings (H/V)	2.86	10/1	$< 5 \times 10^8$
RTML (H/V)	2.86→ 9	10/1	$< 5 \times 10^8$
Main Linac (H/V)	9 → 1500	10/1	$< 5 \times 10^8$
Beam Delivery System (H/V)	1500	10/1	$< 5 \times 10^8$
MDI & Post-collision line	<1500	1000	$< 5 \times 10^3$
	Drive Beam		
Sorce and linac	2.37	50	$< 40 \times 10^6$
Frequency multiplication complex	2.37	50	$< 40 \times 10^6$
Transfer to tunnel	2.37	50	$< 40 \times 10^6$
Turn around	2.37	50	$< 40 \times 10^6$
Decelerator	<2.37	50	$< 1.5 \times 10^6$
Decelerator	<2.37	100	$< 1.5 \times 10^6$

4-profiles method [9] or a quadrupole scanning method [10]. The first method relies on the use of multiple beam size monitors installed at different locations along the beamline and the emittance can be deduced knowing the nominal optics of the machine. The other method only requires one profile monitor, where the beam size is measured varying the strength of a focusing element. This latter method is obviously easier to implement, making it in general cheaper as it only requires a single monitor but the beam optic needs to change accordingly, which may lead to unexpected systematic uncertainty. An alternative solution was proposed and tested on the CTF2 [11], scanning five quadrupoles or more in such a way that the beam size stays constant at the profile monitor while the phase advance through the beam line changes. The use of intercepting devices, like screens, degrade the beam emittance due to multiple scattering effects as the beam passes though the screen and for this reason it becomes safer to dump the beam afterwards. The best solution would then be to measure the beam emittance using the 4-profiles method and non-intercepting devices, which is yet to be developed.

Given that the total number of required devices to measure the transverse beam size foreseen for CLIC is 948, corresponding to 3 times the total number of such devices presently in use at CERN in the whole accelerator complex [3], this indicates that the measurements of transverse beam size have become crucial. The beam emittance is significantly reduced in the damping rings and the performance of transverse profile diagnostics become extremely challenging from the damping rings till the end of the beam delivery system, with a 1 micron resolution. In the following subsections several detection systems which can deal with this challenge are presented.

1.2.1 Invasive beam size diagnostics

Diagnostic instruments in accelerators may be divided into two groups: invasive and non-invasive. The first category, whereby measurement of the beam is obtained through the direct interaction of the beam with matter, form the traditional diagnostics: wire scanners [12, 13], Optical Transition Radiation (OTR) monitors [14], fluorescent screens [15] such as YAG or phosphor.

1.2.1.1 Wire scanner

The standard reference device for beam profile measurements in many accelerators is the wire scanner. Since only a small fraction of the particles of a single bunch is intercepted by the wire scanner, they are less invasive than other beam profile techniques. Often they are used to calibrate other instruments present in a machine such as SR monitors [12].

Fig. 1.2 shows the schematics of a typical wire scanner configuration. A thin wire ($10 - 50\,\mu m$) is swept through the beam. Highly energetic radiation is produced when the incoming particle beam interacts with the wire. Scintillation counters of the Cerenkov light produced in air outside of the vacuum chamber are typically used to detect the secondary particles emitted in this interaction [16]. The signal is proportional to the number of particles. The beam profile is obtained recording simultaneously the wire position and signal amplitude [16]. Single bunch beam profile measurements are not possible because of the limited speed of the wire scanner. In fact a wire scanner measures the average beam profile by sweeping through consecutive bunches of the charged particle beam.

The wire can be swept at a very high speed (up to $20\,m/s$) for intense high brilliant beams. To move the wire at such high speed, a circular movement is employed. However this introduces a disadvantage in reducing the position resolution and hence the profile resolution from $10\,\mu m$ to $100\,\mu m$. The speed of the wire is primarily limited due to the stress properties of the surrounding components that can sustain a limited acceleration

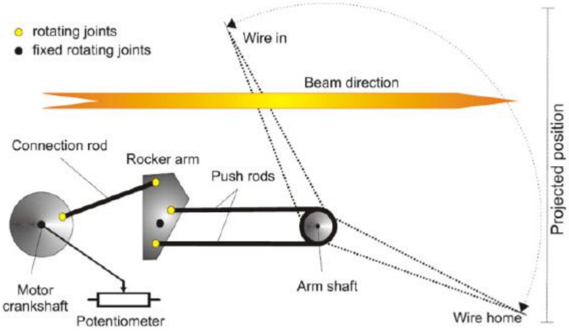

Figure 1.2: Wire scanner schematics [12].

[16].

Although wire scanners are adopted as reference solutions in several machine they presents also some drawbacks. First of all the fragility of such a thin wire: it can break due to the heating caused by the energy deposited by very intense particle beams. Secondly vacuum leakage in the bellows due to wear may also occur. Furthermore inaccuracy of the knowledge of wire position due to vibrations and beam stability over several bunches are additional sources of uncertainty to the beam profile measurements [12, 17].

1.2.1.2 Optical transition radiation imaging systems

Transition radiation (TR) refers to the emission of broad-band electromagnetic radiation that takes place when a charged particle crosses the boundary between two media with different dielectric properties [18]. Monitors based on TR screens, called OTR when the radiation is observed in the optical range of the radiation spectrum, can easily achieve a spatial resolution of $50\,\mu m$, as required from the Main Beam source to the end of the injector linac [3, 19]. Contrary to wire scanners which only give beam profiles over several shots, OTR screens provide images of the beam in a single shot. These technologies have been used for $20 - 30$ years and state-of-the-art devices have even pushed the resolution limit down to few microns [20, 21].

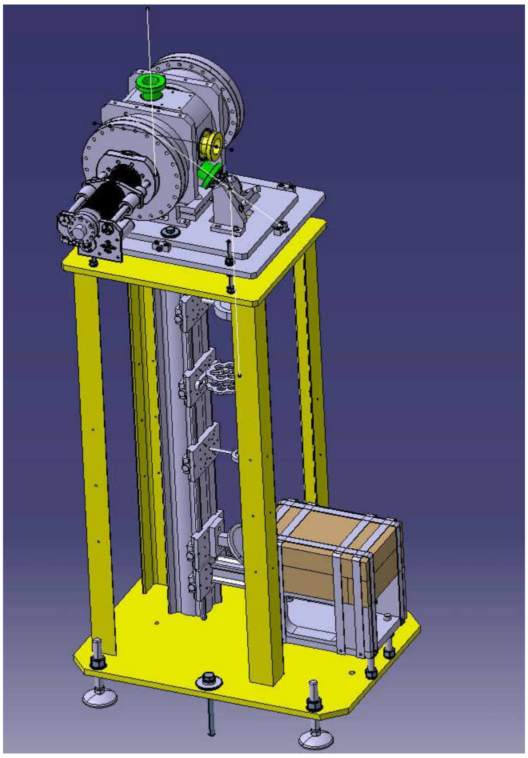

Figure 1.3: Layout of the OTR monitor tested at CTF3: the vacuum tank and actuator of the OTR screen (grey upper part), the optical line sits vertically under the tank, the camera is placed on the bottom over the yellow plate and protected from stray radiation by a shielding (brown bricks) [3].

A typical imaging system, as used on CTF3, is depicted in Fig. 1.3. It is composed of a vacuum tank equipped with a motorized arm, capable of inserting two OTR screens with different reflectivity coefficients and a calibration target. Visible photons are emitted by the screen, reflected vertically downwards and focused onto a CCD camera using a radiation-hard lens. The light intensity is adjustable using a remotely controlled Optical density filter wheel. Lead shielding blocks are installed all around the camera to minimize radiation damage as much as possible [3].

The major limitations for the use of OTR screens in high current beams resides in the beam induced thermal load [3]. This is a strong constraint, which can only be overcome by limiting the number of bunches or reducing the pulse train length.

More recently even very high resolution (better than $1\,\mu m$) monitors based on TR were introduced [22–24]. In these kind of monitors the beam size contribution to the Point Spread Function (PSF) of a standard OTR imaging system is observed. Originally the PSF is an image generated by a point-like source and projected by an optical system on a detector (e.g. CCD camera). The source is provided by optical transition radiation from a conductive target. The PSF must bear information about the source structure, the optical system, and the distribution of electrons (the beam size). It was predicted that the source is non-uniform, but has a minimum in the centre. The width of the PSF (as well as the sensitivity to the transverse beam size) is defined by the optical system, but the visibility is determined by the beam size [3]. As for standard OTR monitors, also in the case of this very high resolution monitor thermal limitations linked to the use of an intercepting device remain true and limit its use to single bunch observation or low intensity beams.

1.2.1.3 Scintillator screen monitors

In the past, fluorescent screens have been widely used to measure the transverse profiles of electron beams at high-energy accelerator facilities [15]. Traditional fluorescent screens based on ZnS produce a bright image but have relatively poor resolution. Phosphors have an individual grain size of $50-100\,\mu m$. Internal scattering of the fluorescence limits the image resolution to the same scale [15]. To overcome this limitation single crystal scintillator was developed, for example Cerium-doped Yttrium-Aluminum-Garnet (YAG:Ce).

For this kind of screen the ultimate spatial resolution is set by both the minimum object size that can be produced by the crystal and by the optical transport of visible light. The minimum object size for high-energy electrons is limited by multiple Coulomb scattering of the beam through the crystal and by the generation of bremsstrahlung. As shown in Fig. 1.4 at high energy this effect is less significant and the dominant limitation is the diffraction limit of the optical system used to image the source.

Another limiting effect is due to the fact that the crystals are transparent to the emitted light so that the beam image is created along the entire depth of the crystal. This produces an extended longitudinal object that must be accurately focused at the plane of the camera, meaning that a thinner crystal has a better intrinsic resolution. At high energy, the resolution for a thin crystal and a carefully designed optical system is ultimately limited by the diffraction of visible light to approximately 1 micron [15].

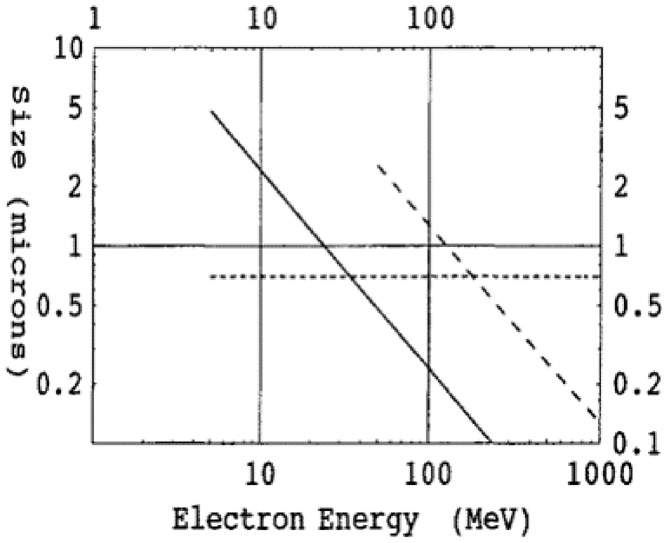

Figure 1.4: The minimun spot size as a function of beam energy for a 0.5 mm YAG crystal: solid line is multiple scattering, dashed line is bremsstrahlung, dotted line is diffraction limit [15].

1.2.2 Non-interceptive beam size diagnostics

1.2.2.1 Synchrotron radiation

CLIC will collide beams with nanometres beam size, which strongly relies on the generation of ultra-low emittances in the damping rings, putting very tight requirements on the spatial resolution of beam size monitors [3]. This problem has been studied in detail during the last 10 years either in the context of performance optimization of 3rd generation synchrotron light sources or in the framework of the CLIC studies with an R&D program performed to prove the feasibility of low emittance generation in damping rings [3]. This work has led to the developments of several techniques, which can provide beam size measurements with resolution of the order of 1 micron. Two of them are based on the use of Synchrotron Radiation (SR) [25].

For highly relativistic particles, the spatial resolution of an SR imaging system is intrinsically limited by diffraction, which can be resolved by using shorter wavelengths. To achieve micron size resolution, imaging systems have been developed in the X-ray wavelength range [26–28]. Other techniques based on the measurements of the PSF on an imaging system have been successfully tested [29, 30]; the SR image is observed as a modulation of the PSF of a simple imaging system and the beam size is extracted obtaining a sub-micron resolution. Another technique, proposed by Mitsuashi [31], has led to the developent of SR interferometers enabling measurement of micron-scale beams via detection of the spacial coherency [32, 33].

Nevertheless SR can only be utilized in circular machines. In linear sections other technologies, which are described below have been developed.

1.2.2.2 Laser wire

One of the most critical issues for transverse profile monitoring is the one-micron resolution beam size measurements in the linear part of a very high current machine where interceptive beam size techniques and SR can not be used. In the CLIC complex, this type of device will be required from the exit of the Damping Ring to the Beam Delivery system. This part covers more than 80 km of beam line and a total of more than 100 devices will be required [3]. Contrary to the rings or turnarounds, where synchrotron radiation could be envisaged as a natural source of light for instrumentation, there is no natural source of photons in a linear accelerator [3]. The use of intercepting devices must be restricted to single bunch mode to prevent any beam-induced damage, as already discussed for intercepting devices.

Laser-wire systems are based on a finely focused laser beam used to scan across an electron beam to measure its transverse profile and thereby determine its emittance [34]. The laser light is scattered off the electron beam because of Compton scattering and the scattered photons (or, at high electron beam energy, the scattered electrons) can be detected downstream [35]. Laser-wires are recognized as the state-of-the-art technology for next generation colliders such as CLIC because they are relatively non-invasive devices that can be used continuously during machine operation. Furthermore they can be used for very high intensity beams, whereas solid wire would be destroyed. They can also be used for beam sizes approaching the wavelength of the laser light [3]. High resolution measurement was performed at ATF2 in KEK, where very small beam profiles, down to $4.8\,\mu m$, have been measured using a Laser Wire Scanner [36].

Another technique based on laser interferometer, proposed by Shintake [37], led to the development of a nm resolution beam size monitor [35,38]. The interference of the two laser beams produces a standing-wave pattern in the direction where the beam is measured. The electron beam is scanned across the standing-wave pattern. When the beam size is large relative to the standing-wave fringe spacing, the core of the beam always intercepts several nulls and peaks of the interference pattern so the number of photons that the beam will Compton scatter is only a weak function of the electron beam position. On the other hand in the case of a beam size very small relative to the fringe spacing, the number of Compton-scattered photons is a strong function of the electron beam position. This means that for an infinitely small beam, the maximum number of photons are scattered when the beam intercepts a bright fringe, whereas no photons are scattered when the beam intercepts a null [35]. This kind of monitor is routinely used to monitor the beam size at ATF2 IP [38] (see section 3.1.5).

1.2.2.3 Diffraction Radiation

Diffraction Radiation (DR) is a polarization radiation that appears when a charged particle moves in the vicinity of a medium [39]. Similarly to the well-known TR, DR is emitted in the specular reflection direction of the incident beam with respect to the medium surface (Backward DR, BDR) and in the direction of the beam (Forward DR, FDR). The main difference between TR and DR is that DR can be used as a non-invasive beam profile measurement technique as the particles pass through a narrow aperture, i.e. a slit or a hole. In the case of DR the beam size information is obtained from its far-field angular distribution [40].

Given these characteristics, DR has been investigated in the last few years as a beam size monitoring technique in different electron accelerators: at the advanced photon source, Argonne [41], at FLASH, DESY [42], at ATF, KEK [43] and on a circular machine at CESRTA [44].

1.3 Motivation

For future linear colliders many profile monitors will be needed: for example as stated in the CLIC design report, the total number of required devices to measure the transverse beam size is 948 [3]. This means that the profile monitors have to be simple to use, robust, and relatively inexpensive to guarantee reliability of the accelerator operations.

One of the technologies that can satisfy these requirements is OTR monitors as TR is a well studied phenomena that can provide single shot small beam (less then one micron) resolution [23]. The main limitation of TR monitors is related to the fact that a TR screen can sustain only a limited number of beam bunches because of the beam induced thermal load [3], limiting the use on a pilot beam with reduced number of bunches or pulse train length.

Non-interceptive techniques are necessary for full beam charge. Laser wire scanners are the state of the art technology to measure small transverse beam size with micron scale resolution [36]. The drawbacks of this kind of monitor is that they measure the average of several bunches and they are expensive to maintain and operate due to the need of several high power laser so difficult and expensive to implement on the large scale needed for future collider. Synchrotron radiation based techniques, that provide another non-intercepting way of extracting information on the beam size can be used only in non-linear sections of the machine, such as dumping rings, adding a strong constraint on their mass use at a linear collider. Diffraction radiation is non-invasive, single shot and based on relatively cost effective technology that can overcome the limitation of the other techniques.

DR experiments mentioned in section 1.2.2.3 were conducted in the visible range showing a sensitivity to the beam size as small as 14 μm [40]. The limited resolution of these systems was due to diffraction limit and to the residual SR contribution. To overcome these problems a study is proposed in the UV range ($250\,nm$) with an upstream mask to block SR light. Furthermore, going down with wavelength is important to reduce the contribution of the coherent component of the DR and TR radiation in the presence of short bunches [45–47].

The aim of this thesis work is to develop a combined TR and DR station for non-invasive beam size monitoring that can overcome the limitations the previous experiment and techniques showed for linear colliders. Combining DR and TR in one instrument, gives possibility of taking advantage of both techniques: observation of sub-micrometre beam sizes using high resolution PSF in TR and using non-invasive DR measurements. Furthermore the idea to observe the position of the beam synchronously with angular pattern of DR far-field light allows the position of the beam inside the DR slit to be monitored (see section 3.4).

Chapter 2

Theoretical Background

Originally predicted by Ginsburg [48] in 1946, TR has been studied experimentally during the last 60 years. TR refers to the emission of broad-band electromagnetic radiation that takes place when a charged particle crosses the boundary between two media with different dielectric properties [18]. The optical frequency band of TR is widely used as a diagnostic technique in particle accelerators [14,49] where the spatial, temporal, or angular characteristics of TR are measured to extract information about the beam. TR is one of the main candidate techniques for the next generation of colliders where beam size will be at the micrometre scale [3] because it can provide very high resolution measurements (even below 1 micron [23]) to resolve such small beam size.

More recently DR has been studied as a transverse beam size monitor technique [40, 50]. Monitors based on DR, a non intercepting technique, are being investigated for high charge beams such as in CLIC [3] or ILC [51]. Since this thesis presents results of studies performed on an electron particle accelerator, focused on the TR and DR emission mostly in the optical and UV wavelength range, descriptions of these two phenomena, from the point of view of the beam diagnostics, are presented in this chapter.

2.1 Transition radiation

TR is produced when a charged particle crosses the interface between two media. The particle interacts with the target surface via its electric fields polarizing it and inducing polarization currents. The radiation is actually emitted by the resulting dipoles present on the surface that start oscillating. In the case that a charged particle crosses a flat boundary between two media with the incident angle, θ_0, TR propagates in two main directions: along the particle trajectory (Forward Transition Radiation, FTR) and in the direction of specular reflection (Backward Transition Radiation, BTR) [43] in both cases with a characteristic opening angle $\theta \approx 2/\gamma$, where γ is the particle Lorentz factor. When the target is a thin foil but its thickness is larger than the skin depth, in this case BTR is produced on the incoming surface and FTR on the outgoing surface as is shown on a simple schematic diagram in Fig. 2.1. The skin depth, l_s, is given by:

$$l_s = \frac{c}{\omega_p} \tag{2.1}$$

where ω_p is the plasma frequency defined as $\omega_p = \sqrt{\frac{n_e e^2}{\epsilon_0 m_e}}$, here n_e is the number density of free electrons, ϵ_0 is the vacuum permittivity and m_e is the electron mass. In the case of Aluminum, a typical material used for OTR the value of l_s is of the order of 12 nm.

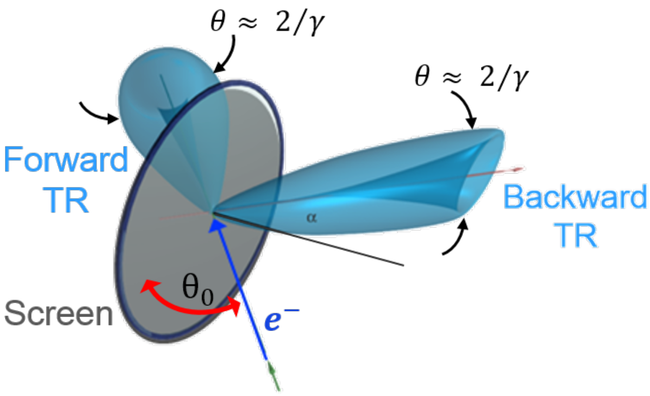

Figure 2.1: Schematic diagram of TR production from an electron e^- crossing a screen (in grey): the cones of emission of Forward TR and Backward TR are represented in light blue, to be noted the minimum in the center and the total aperture $\theta \approx 2/\gamma$. Backward TR is emitted around the reflection angle α.

Models to describe theoretically transition radiation were presented in [52, 53]. In particular the authors of [52] proposed the following approach for better understanding the process of TR. Let a charge, q, move from vacuum into metal (ideal mirror). The electromagnetic field in the vacuum can be represented as the field of charge and the field of its image, −q, which moves toward the charge in the metal (see Fig. 2.2). From the viewpoint of the vacuum, when the charge crosses the first boundary, the charge and its image overlap creating a null effective charge this results in emission of radiation.

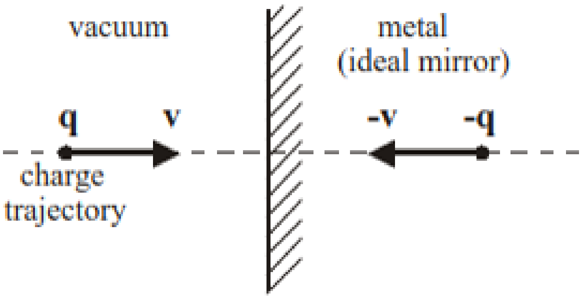

Figure 2.2: TR generation by a charge crossing a boundary between vacuum and ideal conductor (mirror) [43].

In [53] another approach applicable for BTR was proposed. The method is based on the Huygens principle of plane wave diffraction. The field of the charge is represented as a sum of the pseudo-photons. When a particle crosses a boundary, the pseudo-photons are scattered from the surface atoms and propagate in the backward direction. The difference from the plane wave is that the field of the charge depends on the distance from the particle trajectory. The following sections describe the main characteristics of TR of interest for the thesis, using this approach also known as the polarization current approach.

2.1.1 Transition radiation in the far-field

TR is generated by the incident particle field on the surface of a screen. At a given observation wavelength the characteristic dimension of the electric field can be written as $\gamma\lambda/2\pi$, where $\gamma = E/m_e c = \sqrt{1 - v^2/c^2}$ is the charged particle Lorentz factor, λ is the generated photon wavelength, E is the total particle velocity, m_e is the electron mass, c is the speed of light and v is the particle speed. As already introduced in the previous section the particle field polarizes the target surface, therefore, generating a TR source with the same size as the electron field. All points of the source could be treated as independent sources. In the wave zone, all waves propagating from those sources can be considered as plane waves. This approximation is valid if the far-field condition is satisfied. The far-field condition can be written as [54]:

$$\frac{L}{\gamma} \gg \frac{\gamma\lambda}{2\pi} \quad \rightarrow \quad L \gg \frac{\gamma^2\lambda}{2\pi} \tag{2.2}$$

where L is the distance between target and detector and λ is the TR wavelength. This relation indicates that in the far-field, the distance L/γ must be much larger than the effective electric field radius of the charged particle $r_E = \gamma\lambda/2\pi$ [54].

From Eq. 2.2 it is clear that for very high-energy electron accelerators the far-field condition could reach distances from several metres to few kilometres. In this case the theory described in this section might not be applicable. The pre-wave zone effect in BTR or TR at a distance from the target comparable with or shorter than L_f in backward direction is described in the next section.

As is depicted in Fig. 2.3, TR angular distribution is confined within a very narrow cone of order of γ^{-1}. This implies that for FTR the expression of the far-field condition is described by a similar relation to the so-called radiation formation length L_f [54]:

$$L_f = \frac{\lambda}{\pi} \frac{1}{\gamma^{-2} + \theta_x^2 + \theta_y^2} \quad \rightarrow \quad L_f = \frac{\gamma^2 \lambda}{2\pi} \tag{2.3}$$

Here θ_x and θ_y are the radiation observation angles measured either from the mirror reflection direction (for BTR) or from the particle trajectory (for FTR), the approximation $\theta^2 = \theta_x^2 + \theta_y^2 \approx \gamma^{-2}$ is used. The radiation formation length, also called coherence length, has different physical meaning respect the far-field condition. Specifically it indicates that if another photon is produced by the particle at a distance comparable with or shorter than L_f from the target, those two photons are coherent. The real photons and the particle field are completely separated at the distance much larger than the coherence length. In BTR the electron field and the photons are separated at the distance equal to the photon wavelength from the target.

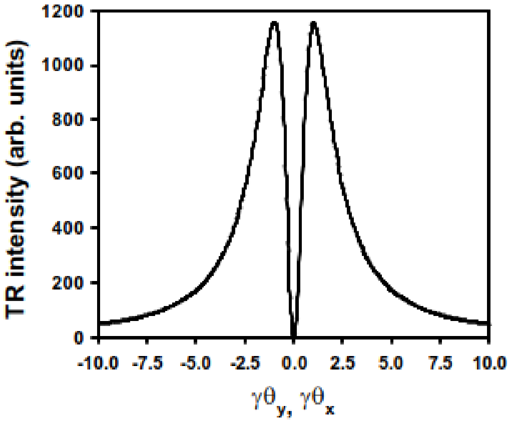

Figure 2.3: Transition radiation angular distribution calculated for $\gamma = 2544$ [43].

The detailed TR theory in the wave zone is well described in literature [52, 53]. The approach for calculating TR from a particle obliquely passing through a boundary between vacuum and an ideal conductor is presented in [53]. Of particular interest there is also a model proposed in [55] where an ultra-relativistic approximation ($\theta_x, \theta_y, \gamma^{-1} \ll 1$) is applied to obtain a much simpler equation for the intensity $\mathrm{W_{TR}}$ for a given photon frequency ω and solid angle Ω:

$$\frac{\mathrm{d}^2\mathrm{W_{TR}}}{\mathrm{d}\omega\mathrm{d}\Omega} = \frac{\alpha}{\pi^2}\frac{\theta_x^2+\theta_y^2}{\left(\gamma^{-2}+\theta_x^2+\theta_y^2\right)^2}\left\{\frac{1}{\left(1-\theta_y\cot\theta_0\right)^2}\right\} \tag{2.4}$$

here α is the fine structure constant and θ_0 is the target tilt angle with respect to the particle trajectory (see, for instance, Fig. 2.1). From here on, unless otherwise stated, the following system of units $\hbar = m_e = c = 1$ is used. TR angular distribution in forward and backward directions coincide in case of an ideal conductor. It is possible to notice that the term before the curly braces in Eq. 2.4 is the TR for the case of normal incidence ($\theta_0 = 0$). The angular distribution for the normal incidence in the case of an electron in ATF2 at energy $E = 1.3\,GeV$ ($\gamma \approx 2544$) is presented in Fig. 2.3. In this case, it is possible to consider the TR angular distribution as an azimuthally symmetric crater-like distribution with a polar angle of the order of γ^{-1}, similar to the TR shown in Fig. 2.1. However, the term in the curly braces in Eq. 2.4 is responsible for TR asymmetry. The percent asymmetry, defined as r, could be estimated in the way presented in [55] derived from Eq. 2.4 considering the peak intensities at $\theta_{x,y} = \gamma^{-1}$ and $\theta_{x,y} = -\gamma^{-1}$:

$$r = \frac{I_R - I_L}{\frac{1}{2}\left(I_R + I_L\right)} = 4\gamma^{-1}\cot\theta_0 \tag{2.5}$$

In Eq. 2.5 I_L, I_R are the intensities of the left ($-\gamma^{-1}$) and right ($+\gamma^{-1}$) maxima (see Fig. 2.3) of the angular distribution in the diffraction plane ($\theta_x = 0$), i.e. in the plane of the particle trajectory and its projection onto the target plane. For example, for the target tilt angle of 45° and beam energy $E = 1.3\,GeV$ ($\gamma \approx 2544$) the asymmetry is of about 0.16%, which is negligibly small. Therefore, the term in the figure brackets in Eq. 2.4 can be neglected in the GeV energy region and for the target tilted angles $\theta_0 \gg \gamma^{-1}$. In this case the TR angular distribution can be considered as azimuthally symmetric [43].

Eq. 2.4 shows also that the TR from an ideal conductor is independent of the radiation wavelength. However, it has to be said that this equation could only be used with a proper accuracy for TR photon energies smaller than the plasmon energy of a substance, which is about $10\,eV$ for a metallic foil. This equation is, therefore, valid for wavelengths longer then $\approx 0.12\,nm$, meaning that it can be used in the visible and UV range.

2.1.2 Transition radiation in the near-field

Development and study of high-energy accelerators is the new frontier for accelerator physics [3, 56]. Increasing beam energy leads to new effects. Some of them are very interesting from the point of view of physics and applications; others set new obstacles in scientific investigations. One of the latter is the pre-wave (or near field) zone effect [43], meaning that TR radiation from ultra-relativistic beams has to be observed before it can reach the far-field condition. The theory of the pre-wave zone effect in FTR and BTR has been address by several authors [20, 57–60].

In this section some aspects of pre-wave zone effect for BTR are presented, as this is the situation we had to deal with in our experiment. The pre-wave zone for BTR can be understood in the following way. When a charged particle crosses a boundary between vacuum and a material, it induces polarization currents on the material surface. The region of the induced currents is the TR source [43]. Actually, that region is determined by the incident particle field radius treated as $\gamma\lambda/2\pi$ (see Fig. 2.4) because this is the characteristic field dimension at a given wavelength of a relativistic particle.

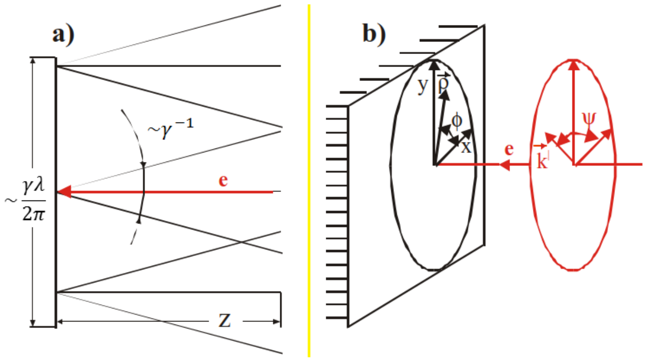

Figure 2.4: a) Schematic of emission cone angle for TR (presented here) and DR for 3 point like sources inside the electron effective field radius b) Schematic of TR source with coordinate reference system [43].

Inside this region all points of the radiation source start emitting radiation. At the close distance to the target the radiation source can not be treated like a single point. The question that may rise is how far the observation point must be in order to obey the far field approximation. To answer this question it is useful to refer to Fig. 2.4b). The TR spot in the detector plane must be much larger than the radiation source size. In other words, if z is the distance from the observation point, to distinguish to different point source then the following condition must be fulfilled:

$$\frac{z}{\gamma} \gg \frac{\gamma\lambda}{2\pi}, \text{ or } z \gg \frac{\gamma^2\lambda}{2\pi} \tag{2.6}$$

where z/γ is a the characteristic dimension of the single point TR as γ^{-1} is the emission angle. This very simple analysis has led to an expression similar to the far-field condition already presented in Eq. 2.2. When the condition in Eq. 2.6 is not fulfilled, the formulae described in the previous section 2.1.1 can not be used.

Since the studies presented in this thesis were performed in GeV energy range, the approach presented in [57] will be described in detail. This is a rather simple approach for calculating the BTR spectral spatial characteristics for an ultra-relativistic case.

Consider a charged particle that normally crosses a boundary between vacuum and an ideal conductor. In the ultra-relativistic case only transverse components of the particle field are essential. The moving charge field can be described by a superposition of pseudo-photons [53], as the electrical field of an ultra-relativistic particle is almost transverse to to the relativistic compression in the longitudinal direction:

$$E_{x,y}\left(k_x^{\perp}, k_y^{\perp}\right) = -i4\pi e \frac{k_{x,y}^{\perp}}{k_x^{\perp 2} + k_y^{\perp 2} + k^2\gamma^{-2}} \exp(-ik_z z). \tag{2.7}$$

In Eq. 2.7 e is the charge of the particle, $k = 2\pi/\lambda$ is the wave number, $k_{x,y}^{\perp}$ are transverse components of the pseudo-photon wave vector determined in the polar coordinate system by the following relations (see Fig. 2.4b):

$$k_x^{\perp} = k^{\perp}\cos\psi,\ k_y^{\perp} = k^{\perp}\sin\psi. \tag{2.8}$$

The radiation field is obtained satisfying the boundary condition for the tangential component. In the coordinate space representation it has the following form:

$$E_{x,y}^{r}\left(\rho_x, \rho_y\right) = -\frac{ie}{\pi}\int_0^{\infty} \frac{k_{x,y}^{\perp} dk_x^{\perp} dk_y^{\perp}}{k^{\perp 2} + k^2\gamma^{-2}} \exp\left(iz\sqrt{k^2 - k^{\perp 2}}\right) \exp\left(ik_x^{\perp}\rho_x + ik_y^{\perp}\rho_y\right) \tag{2.9}$$

where ρ_x and ρ_y are the components of the TR photon wave vector determined in the transverse plane measured in metres as can be seen in Fig. 2.4 by the following relations (see Fig. 2.4b):

$$\rho_x = \rho \cos\phi, \quad \rho_y = \rho \sin\phi. \tag{2.10}$$

At any distances longer than the radiation wavelength, the TR spatial spectral distribution per unit frequency and per unit transverse area can be written in the following form:

$$\begin{aligned} \frac{d^3W}{d\omega dx dy} &= 4\pi^2 k^2 \left[\left|E_x^r\right|^2 + \left|E_y^r\right|^2 \right] = \\ &= \frac{\alpha k^2 z^2}{\gamma^2 \pi^2} \left| \int_0^\infty \frac{t^2 dt}{t^2 + \gamma^{-2}} J_1 \left(\sqrt{x^2 + y^2} \frac{kzt}{\gamma} \right) \exp\left(ikz\sqrt{1 - t^2} \right) \right|^2 \end{aligned} \tag{2.11}$$

where J_1 is the Bessel function of the first order, $x, y = \gamma \rho_{x,y}/z$ and t is the normalized angle defined as $t = \gamma\theta$. It is possible to notice that at large distances from the target x and y coordinates could be considered as the photon emission angles in units of γ^{-1} measured from the mirror reflection direction. In spite of an infinite integration limit the dominant part of the integral is confined within a very small angular range $\Delta t \ll 1$. The calculations can be performed numerically [43].

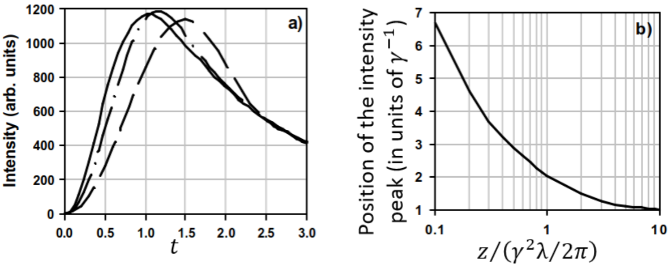

Figure 2.5: a) Transition radiation space distribution in the pre-wave zone calculated for different distances from the target: $z = 10\gamma^2\lambda/2\pi$ - solid line, $z = 4\gamma^2\lambda/2\pi$ - dash-dotted line, $z = 2\gamma^2\lambda/2\pi$ - dashed line; b) dependence of the maximum position as a function of the distance from the target [43].

TR spatial distributions for different distances to the observation point are presented in Figure 2.5. It can be seen that the TR space distribution is different from the far-field angular distribution described in the previous section 2.1.1: the transverse position of the maximum is not at $t = \gamma\theta$. Increasing the distance to the observation point approaching

$z = 10\gamma^2\lambda/2\pi$ the distribution is transformed into the usual distribution in the wave zone and its intensity is saturated to the far field one from an infinite boundary:

$$\frac{d^2W_{TR}^{max}}{d\omega d\Omega} = \frac{\alpha\gamma^2}{4\pi^2} \tag{2.12}$$

Experimentally this effect was observed in [61]. The authors as performed a series of experiments in the pre-wave zone predicted by the theory. Their results are in reasonable agreement with the theoretical approach described above. So far there are a lot of theories developed including the far-field approximation. That is because the approximation allows rather simple formulae to be obtained. However, it might be necessary to revise most of the formulae to be able to perform calculations for highly relativistic electron beams. Otherwise the condition in Eq. 2.6 must be fulfilled, which is difficult for beam energies higher than a few GeV.

For example, using Eq. 2.6 for beam energy of 1.3 GeV (KEK-ATF) and the radiation wavelength of 400 nm the target-to-detector distance must be about 2.5 m to be able to obey far field approximation. However, for the beam energy of 380 GeV (CLIC stage 1 see Tab.1.1) the target-to-detector distance must more than 220 km, which is an unreasonable distance to achieve.

2.1.3 Transition radiation PSF measurements

The resolution of a conventional OTR monitor is defined by the root-mean-square of the so-called PSF [20]. The PSF can be defined as the source distribution generated by a single electron and projected by an optical system onto a detector. In the optical wavelength region the resolution is limited and defined by diffraction and aberration effects of the optical system. Such effects lead to the broadening of the PSF and to a lower resolution. The best resolution achieved by conventional OTR monitors is about a few micrometers [21]. However, in [62] the authors demonstrated that the OTR PSF differs from a conventional PSF of an optical system.

Figure 2.6 shows a measured polarization component of the OTR PSF that has a two-lobe structure. Specifically OTR is radially polarized; in this experiment the vertical polarization was observed because it was in the direction of smallest beam size reachable in the experiment (less then 1 μm). The visibility (I_{min}/I_{max}), defined as the ratio between the minimum I_{min} in between the two lobes and the peak value of the lobe (I_{max}) can

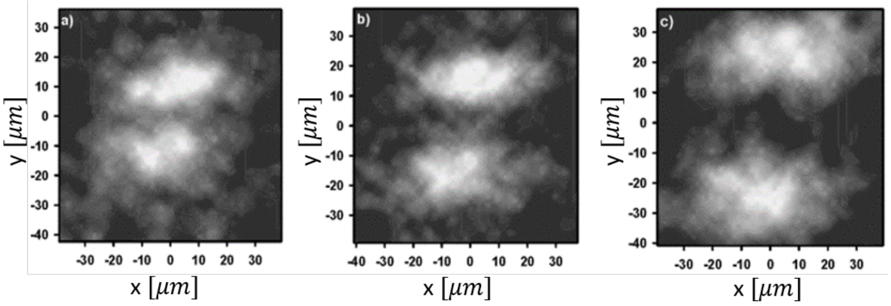

Figure 2.6: TR PSF measured at the Accelerator Test Facility 2 (ATF2 see sec.3.1) for a beam size $\sigma_y = 1.73\,\mu m$, $\sigma_x = 23.04\,\mu m$ for 3 different wavelengths: a) $609\,nm$ b) $558\,nm$ c) $459\,nm$ [62].

be used to monitor vertical beam size with sub-micrometer resolution. This approach has been demonstrated with several measurements performed at the Accelerator Test Facility 2 (ATF2) in [22,23]. Fig. 2.7 shows the change of the dept of the minimum in between the lobes for different beam size, in particular a smaller beam led to a deeper minimum. On the other hand if the beam is flat (much smaller in vertical direction than the horizontal), which is true for linear colliders such as CLIC [3], the horizontal projection of the distribution represents a direct measurement of the horizontal beam size that is much larger than the vertical size. This gives the opportunity to diagnose an electron beam size in two directions in a single shot, avoiding using two different instruments for the purpose.

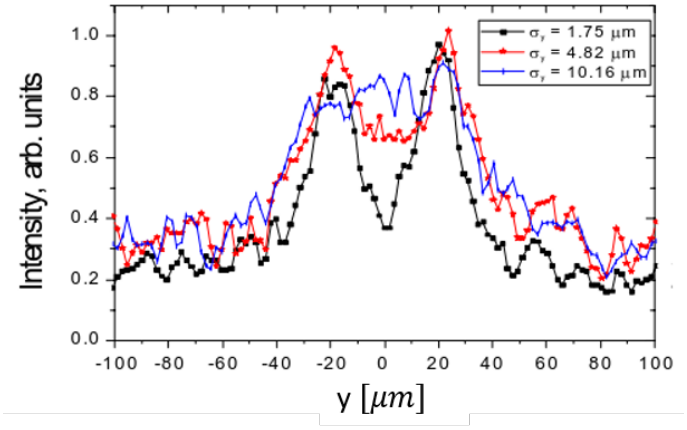

Figure 2.7: Three TR distributions measured with 550nm optical filter for three different vertical beam sizes: $\sigma_y = 1.75\,\mu m$, $\sigma_y = 4.8\,\mu m$ and $\sigma_y = 10.16\,\mu m$ [22].

This particular method of using TR to measure very small beam sizes has been introduced here not only because of the interest in small beams (micrometre scale) for the next generation of colliders, but also because it has been used during the experimental campaign described in Chapter 4 to calibrate DR in the condition of a small beam.

2.1.4 Zemax simulation

Zemax Optical Design Studio is a readily available commercial software package which integrates all the features required to conceptualise, design, optimise and analyse virtually any optical system. Zemax makes use of diffraction calculations to propagate a wavefront through an optical system surface by surface. In this way the wave-like nature of light is fully accounted for [63]. As input to ZEMAX, the approximation of the electric field for the OTR vertical polarization component induced by a single electron on a target surface is used [64], defined by the following equation [65]:

$$\begin{aligned}
&\operatorname{Re}(E_y) = const\frac{Y}{\sqrt{X^2+Y^2}}\left[\frac{2\pi}{\gamma\lambda}K_1\left(\frac{2\pi}{\gamma\lambda}\sqrt{X^2+Y^2}\right)-\frac{J_0\left(\frac{2\pi}{\gamma\lambda}\sqrt{X^2+Y^2}\right)}{\sqrt{X^2+Y^2}}\right] \\
&\operatorname{Im}(E_y) = 0
\end{aligned} \tag{2.13}$$

with X and Y the two orthogonal coordinates of the target surface measured from the point of electron incidence, *const* is a scale constant, K_1 is the modified Bessel function of first order, and J_0 is the Bessel function of order zero.

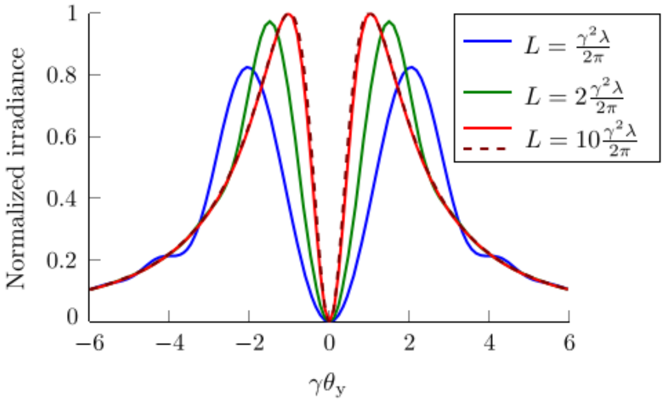

Figure 2.8: Comparison between TR angular distribution theoretical prediction in the far-field (dashed line) and Zemax simulation reaching the far-field condition: L is the distance between the source and the detector plane [63].

This tool has been successfully tested and used to simulate TR in the far-field [63] and in the near-field [65]. For example, in Fig. 2.8, very good agreement between the theoretical TR angular distribution and the Zemax simulation is shown when the detector is placed far enough away from the source (approaching 10 times the formation zone), i.e. when this distance is much larger then the formation length (L_f).

Another example of interest for this thesis is that presented in [65]. That case, illustrated in Fig. 2.9, shows a good agreement between the position of the main peak of TR PSF for the ATF2 in the case of Zemax simulation versus the real measurement performed with a CCD sensor.

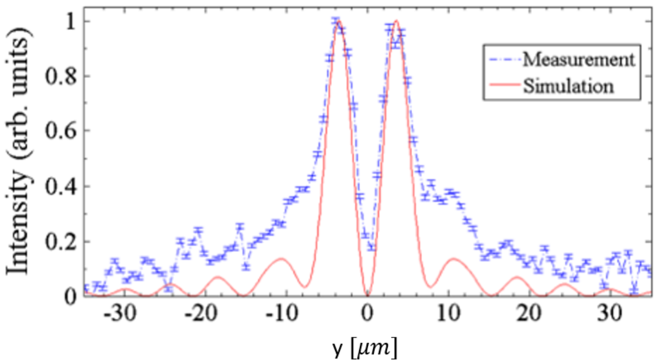

Figure 2.9: Comparison between TR PSF measured and simulated with achromatic lens (DLB-30-120-PM from Sigma-Koki) at the best focus ($\gamma = 2500$ and $\lambda = 550\,nm$) [65].

This kind of simulation were performed during the preliminary studies of this thesis to predict, guide and validate the experimental campaign. In particular an intensive investigation was performed to study TR interference, the results of this study are presented in the next section (2.1.5).

2.1.5 Transition radiation interference

When two or more coherent TR sources are present, it is predicted that radiation from these two sources may interfere. A strong interference take place if the distance between TR sources is comparable or shorter than the formation length L_f. This condition can be written as $\delta < 1$ where δ is defined as d/L_f so the distance between radiators d normalized by formation length [18]. Some aspects of multi-TR emission have previously been studied, e.g., the constructive interference of x-ray TR in a stack of thin foils was investigated theoretically [66] and experimentally [67] in the 1970s. The angular distributions in the far-field region from electrons of 70 MeV and distances between foils down to 2 mm ($\delta =$

1.215) were studied in the pioneering work of Wartski [68] on optical transition radiation interference (OTRI). Several experiments on interferometry [69, 70] were conducted more recently in similar conditions, i.e. with δ values of 323 and 10, respectively. They all reported measurements well in agreement with Wartski's predictions and proposed the use of such an interferometer for beam size, emittance, and energy measurements. More recently, advanced beam diagnostic techniques using both OTR and DR [40, 71, 72] require the use of two thin metallic foils or slits separated by a distance much shorter than the formation length ($\delta \ll 1$). In this case, pronounced suppression of the TR field, also referred to as the shadowing effect [73, 74], is predicted to occur [18].

This phenomenon is of primary interest for an instrument that uses a mask to block any Synchrotron Radiation (SR) contribution that can increase the background and influence the pattern of TR or DR. Because the instrument designed and tested during the experimental campaign object of this thesis, described in detail in Chapter 3, make use of this kind of mask, a preliminary study was performed on CALIFES beam line at CERN. The CALIFES beam line and the experimental set-up are described in detail in Appendix A, where the experiment, which consists of the study of the interference of two TR screens with the possibility to vary the inter-screen distance (d), is presented. The two screen are installed on the same mounter with an angle of 90 degree in between them so that every screen intercepts the beam with an angle of 45 degree respect to the beam longitudinal axis. The inter-screen distance at the location of the beam-screens interaction location can be varied with a range $0 < d < 34\,cm$. For a full description of the experimental set-up the reader can refer to Appendix A; here is reported a schematic of the installation in Fig. 2.10.

Fig. 2.11 and Fig. 2.12 illustrate respectively the results of the Zemax simulations, introduced in section 2.1.4, and the measurement performed. In particular the angular distribution of OTRI at 650 nm is presented, demonstrating a broadening of the two main lobes of the TR distribution decreasing the inter-screen distance to values shorter then the formation length ($\delta << 1$). Such a broadening with respect to a single screen distribution was observed also in [68].

The total intensity recorded at 400 and 650 nm of OTRI is depicted in Fig. 2.13. Here the OTRI intensity curves are normalized to the intensity of the single screen and plotted as a function of the normalized distance δ. Starting from the right-hand side ($\delta > 2.6$ for 400 nm, > 4.2 for 650 nm), where the signal is generated solely by the second

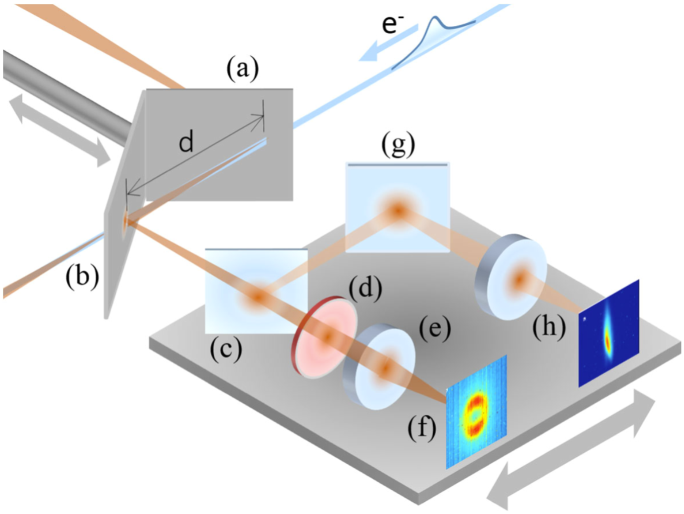

Figure 2.10: OTRI setup at CALIFES [18]:detailed description of the experimental set-up is presented in the Appendix A.

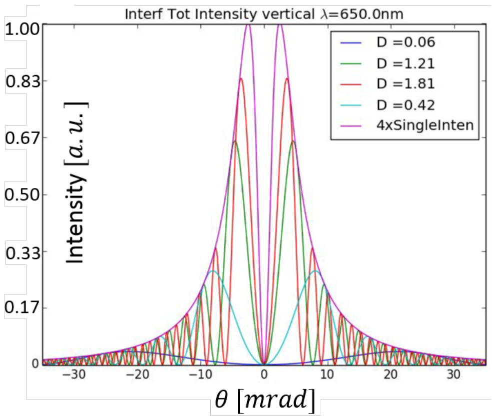

Figure 2.11: OTRI angular distribution simulated with Zemax for different distance D between screens. The envelope corresponding to 4 times the single screen intensity is also reported.

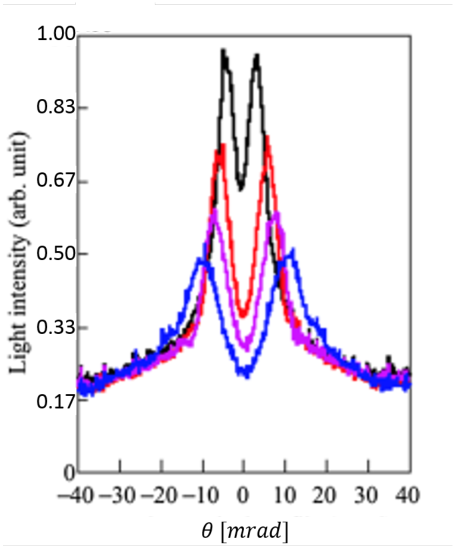

Figure 2.12: Measured OTRI angular distribution for $\delta = 1.11$, 0.47, 0.16, and 0.05 for black, red, magenta and blue respectively [18].

screen (b) in Fig. 2.10, the total intensity reaches twice the reference value as soon as the beam crosses both screens (a) and (b) in Fig. 2.10, as predicted in Ref. [68]. The intensity curves remain approximately constant until $\delta \approx 1$, where a shadowing phenomena starts to appear and the total emitted optical intensity drops abruptly. It has to be remarked that when $\delta = 1$ the radiation field is exactly 1 wavelength ahead of the electron field. At distance $\delta < 1$ the FTR severely interferes with the electron field partially cancelling it out. It results in a reduced effect of polarization at the second target and decrease of the produced light intensity. However, if we compare OTRI intensity at different wavelengths, the curves overlap when plotted as a function of normalized distance. This illustrates that the photon yield is not only reduced but shifted towards higher frequencies [18].

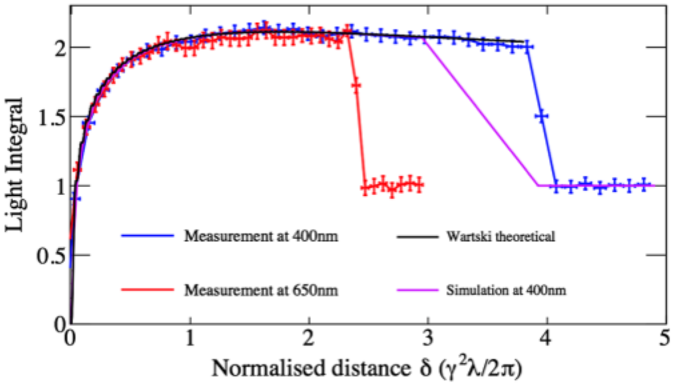

Figure 2.13: OTRI intensity, normalized to the single screen OTR intensity as a function of the normalized inter-screen distance δ, for the wavelengths 400 (blue line) and 650 (red line) nm. Experimental results are compared with analytical results from Ref. [68] (black line) and with Zemax (magenta line) [18].

Experimental data are also compared with analytical formulas for the far-field distribution per unit frequency ω over a solid angle $d\Omega = \sin\theta d\theta d\phi$ [68]:

$$\frac{dI}{d\omega} = F(\omega)\frac{e^2 v^2 \sin^3\theta d\theta d\phi}{\pi^2 c^3 \left[1 - (v^2/c^2)\cos^2\theta\right]^2}\left|1 - e^{-i\delta}\right|^2 \tag{2.14}$$

where $F(\omega)$ is the surface reflectivity, e the elementary charge, c the speed of light in vacuum, v the particle speed, θ and ϕ are the polar and azimuthal angles, respectively. Equation 2.14 attributes the decrease of total emitted power to the progressive destructive interference between the two OTR sources. What is shown on Fig. 2.13 (black solid line) is the integral of Eq. 2.14 over the same experimentally accessible angular range, normalized to the single screen total emission calculated with the same formula. Analytical predictions are in very good agreement with experimental data. This seems to suggest that a model solely based on optical interference between two identical OTR sources separated by a distance d and with a phase relation δ between them can correctly describe this shadowing phenomena. This is remarkable as the physical process *per se* is not the optical interference between the two OTR sources but between the forward OTR emitted by the first screen and the electromagnetic field associated with the electrons [18]. The latter is not a purely transverse electromagnetic field and therefore, only to a degree of approximation can be considered a radiation field (i.e. light). By adopting this approach, shadowing is the interference between the forward OTR photons and the quasi-photons associated with the moving electron (see Refs. [60, 74]). Any radiator downstream of the first screen at a normalized distance of $\delta < 1$ will be in its shadow. At a distance $\delta \ll 1$, the FTR field almost completely cancels out the field of the electron, which is a region where no radiation is produced. At a distance $\delta \gg 1$, the electron field will be completely restored to its original value and is completely separated in time from the FTR field [18].

The validity of a purely optical model for shadowing is further confirmed by optical simulations, performed with Zemax [63, 65], of the propagation of the forward OTR field from the first screen to the second using near-field diffraction formulas. The resulting field is over-lapped with the backward OTR field generated by the beam at the input face of the second screen. The phase shift $e^{i\delta}$ is added to account for the time of flight difference between the particles and the forward OTR field when propagating between the two screens. The integrals of the resulting angular curves over the angular range accessible to the instrument are plotted on Fig. 2.13 (solid magenta line) for 400 nm, showing very good agreement with both the experimental and analytic data [18].

This study clearly shows how a mask present in front of the main target to remove the SR background adds a contribution in the observed pattern, not only in the shape of this pattern but also in the total amount of radiation detectable at a given wavelength. As it is shown later, in case of DR the contribution of forward DR can be neglected if the mask slit is four times larger than the DR slit. However it may not be enough to completely eliminate SR background [75].

2.2 Diffraction Radiation

Another kind of polarisation radiation is Diffraction Radiation (DR). In particular, the atomic electrons of the surface of a medium are excited by the electric field of a charged particle when it moves in the vicinity of this medium. Polarisation currents are produced which are accompanied by the emission of electromagnetic waves i.e. the emission of photons [39]. DR describes photons which are emitted when a charged particle passes through a target aperture. In this case the charged particle does not intersect the boundary of the medium, like in TR, but interacts with the medium via its electric field only. As a result, the particle does not experience any multiple scattering or bremsstrahlung mechanism of energy loss.

As indicated in [43], the DR spectral angular distribution can be calculated using:

$$\frac{d^2W}{d\omega d\Omega} = 4\pi^2 k^2 \left(|E_x|^2 + |E_y|^2 \right) \tag{2.15}$$

where the wave number is defined as $k = 2\pi/\lambda$ and $E_{x,y}$ are the two orthogonal polarisation components of the radiation field integrated over the target surface. The total field of this DR is dependent on the incident charged particle field [43, 55].

Because the electric field of the charged particle depend on the distance from the particle itself, the emission of DR is dependent on the distance between the charged particle trajectory and the medium polarized. The field of a moving charge in vacuum with velocity v, frequency ω and energy $E = \gamma mc^2$, where γ is the Lorentz factor, m is the rest mass of the charged particle and c is the speed of light, can be described by the relation: $E \propto \exp(-d\omega/\gamma v)$ that shows how the field decreases with distance d in the direction perpendicular to the charged particle velocity. Therefore, DR polarisation currents are located in the layer closer to the surface and the properties of DR strongly depend on the properties of this layer. Furthermore, DR does not appear for a charged particle uniformly moving in parallel with an infinite plane surface of a homogeneous ideally conducting medium [39].

The impact parameter h_d defined as:

$$h_d \leq \frac{\gamma\lambda}{2\pi} \tag{2.16}$$

This parameter is explained in Fig. 2.14 where the condition on the distance from the beam to the slit edge for the emission of DR is depicted. This condition is defined by the effective electric field radius of the charged particle $r_E = \gamma\lambda/2\pi$ [54].

Like TR, DR is emitted in two directions as shown in Figure 2.14: Forward Diffraction Radiation (FDR) is emitted in the direction of the charged particle trajectory; Backward Diffraction Radiation (BDR) is emitted in the direction of specular reflection relative to the target.

An important property of DR is that it is considered to be non-invasive. In fact, the energy loss of charged particles due to DR is much smaller than the energy of the

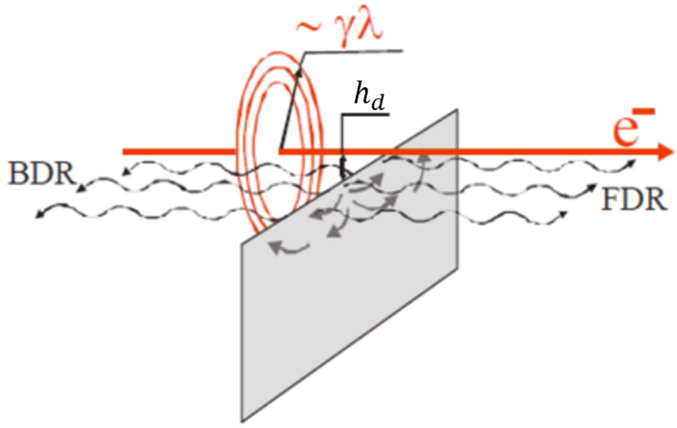

Figure 2.14: Schematic emission of DR from an electron moving in the vicinity of a medium [43].

fast moving charged particle. Therefore, the particle velocity can be treated as constant to a good accuracy [39] and DR, particularly BDR, can be used for non-invasive beam diagnostics in low background conditions.

2.2.1 DR in the far-field and near-field

As already introduced for TR in section 2.1.1, the far-field zone is the region at which the angular distribution of DR is observed. The distance from the target to the observation point is assumed to be so large that it is possible to introduce the DR field as a superposition of plane waves of different amplitude emitted by each elementary source of the target. In this case Fraunhofer diffraction theory can be used [54].

Also for DR, the wave zone is defined by the far-field condition described by the Eq. 2.4; from this condition it is seen that in the far-field the distance z/γ must be significantly greater than r_E. Like TR, the angular distribution of DR is emitted in a cone of order $\theta = \gamma^{-1}$ where $\theta^2 = \theta_x^2 + \theta_y^2$ is the polar observation angle.

The pre-wave zone is the region where the far-field condition is not satisfied. In this case, the DR distribution observed is a spatial-spectral distribution; it not purely angular but includes a spatial contribution determined by the radiation source size.

The radiation source size is equal to the electric field radius which can be treated as the effective radius r_E as shown in Figure 2.14. On the contrary compared to the far-field, for a detector located inside the pre-wave zone, DR photons with different emission angles arrive at the same observation point on the detector plane [54].

The spatial distribution is transformed into the angular distribution in the far-field zone only [54]. As aforementioned, this can be achieved by satisfying the far-field condition for example by using a long-line optical system where the detector is located far away from the DR target.

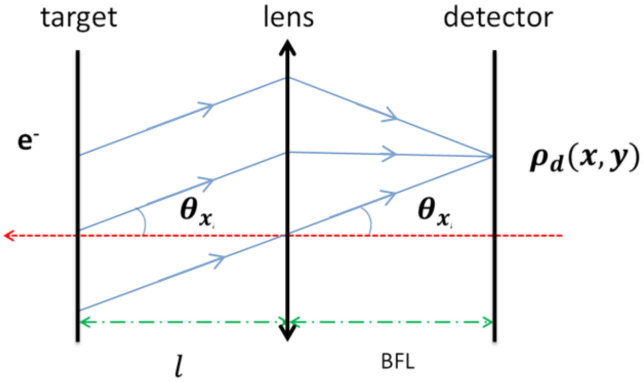

Figure 2.15: Geometry of photon propagation using a thin lens to recreate the far-field condition, where l is the distance from the target to the lens, BFL is the back focal length of the lens and $\rho_d(x, y)$ is the position of emission angle $\theta_{x,y}$ on the detector plane. The dashed red arrow indicate the charged particle trajectory [76].

If the far-field condition cannot be satisfied due to spatial constraints like in a high energy accelerator, where the far-field distance may be reached after several metres, the DR angular distribution may be obtained in the pre-wave zone through the use of a lens where the detector is positioned at the back focal plane. This setup can be considered as an alternative case of Fraunhofer diffraction as described in [77].

The author in [54] presents a detailed report on the methods of pre-wave zone suppression. In this section, the propagation of BDR through a thin lens is reported since this setup was used for the experiment at ATF2 (Section 3.4) due to spatial constraints and the simplicity of installation and alignment in the accelerator tunnel.

Figure 2.15 illustrates the geometry of the photon propagation in the pre-wave zone setup through a thin lens. The lens focus all parallel rays or photons with the same emission angle $\theta_{x,y}$ to a common point on the detector plane $\rho_d(x, y)$ in the case that the detector is positioned at the back focal plane of this lens. In this way, the DR source is effectively shifted to infinity [54].

The lens radius must be sufficiently large to avoid distortions to the DR distribution. First of all, the lens must be larger than the radiation source size to avoid distortions due to diffraction of the photons from the source tails. Secondly, it has to be taken into account that every elementary source contributes to the radiation source spot size emitting a cone with divergence of the order γ^{-1}.

In order to suppress the pre-wave zone without producing distortions to the DR angular distribution the lens must be considered infinite by satisfying the condition [54]:

$$R_l \gg \frac{l}{\gamma} + \frac{\gamma\lambda}{2\pi} \tag{2.17}$$

where l is the distance from the target to the lens and R_l is the lens radius. In Equation 2.17 the first term describes the DR spot size increasing with distance from the target and the second term describes the radiation source spot size, i.e. the effective electric field radius r_E [54].

2.2.2 DR from a slit between semi-planes

Since the main experimental studies of this thesis concern the DR emitted by electron beam moving throw a slit, in this section the equations describing the single particle moving throw a slit are presented.

The convention described in Fig. 2.16 is used: θ_0 is the tilt angle of the screen with respect to the particle trajectory and $\theta_{x,y}$ are the horizontal and vertical angles with respect to the reflection direction.

The spectral angular DR distribution for a single electron passing between two semi-planes is given by [43]:

$$\begin{aligned}\frac{d^2W_{DR}^{slit}}{d\omega d\Omega} =& \frac{e^2\gamma^2}{2\pi^2}\frac{\exp\left(-\frac{2\pi a\sin\theta_0}{\gamma}\sqrt{1+t_x^2}\right)}{\left(1+t_x^2+t_y^2\right)\left(1+t_x^2\right)} \\ &\times\left[\left(1+2t_x^2\right)\cosh\left(\frac{4\pi a_x}{\gamma\lambda}\sqrt{1+t_x^2}\right) - \cos\left(\frac{2\pi a\sin\theta_0}{\gamma\lambda}t_y + 2\psi\right)\right],\end{aligned} \tag{2.18}$$

where a is the slit size, $a/2 < a_x < a/2$ is the offset of the electron with respect to the slit centre in the plane perpendicular to the particle trajectory, θ_0 is the target tilt angle with respect to the incoming electron trajectory, e is the elementary charge constant. In Eq. 2.18 new more convenient variables have also been introduced: $t_x = \gamma\theta_x$, $t_y = \gamma\theta_y$ and $\psi = \arctan\left(t_y/\sqrt{1+t_x^2}\right)$ where $\theta_{x,y}$ are the radiation angles measured from the mirror reflection direction [43].

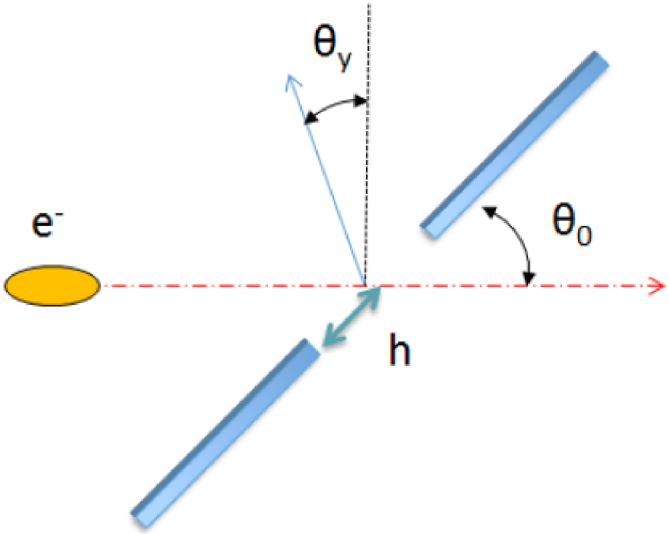

Figure 2.16: DR from a slit: θ_0 is the angle between the incoming particle (e^-) and the screen, θ_y is the angle measured from the reflection angle [76].

Figure 2.17, where the case of an electron at $1.3\,GeV$ moving through a slit used during the experimental campaign (see sec. 3.3) is considered, illustrates how the DR intensity reaches a maximum in the diffraction plane ($t_x = 0$) at $t_y \sim \pm 1$ [43]. Generally, DR intensity exponentially decreases as a function of aperture size. Reducing the target aperture size increases the number of atoms of the target material within the effective electric field radius r_E. This results in a higher yield of photons emitted and is one way in which the DR signal can be increased above background.

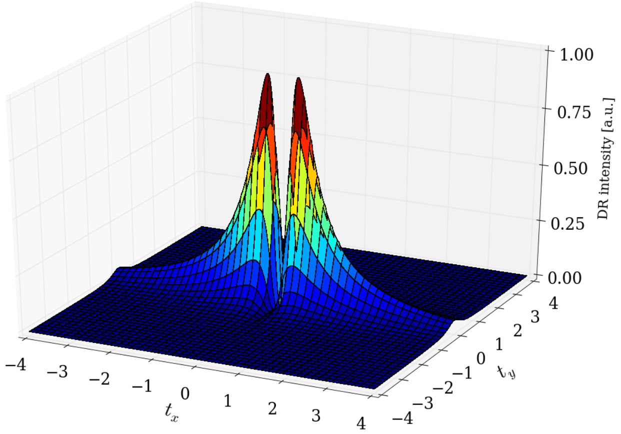

Figure 2.17: Diffraction radiation angular distribution calculated using Eq. 2.18 where $\gamma = 2544$, $a = 50\,\mu m$, $\lambda = 400\,nm$, $\theta_0 = 45°$ and $a_x = 0$.

2.2.3 Beam size effect on DR pattern

In [78] the author has shown that the vertical polarisation component is sensitive to beam size. It is assumed that electron beam has a Gaussian distribution described by

$$G\left(\overline{a_x}, \sigma_y\right) = \frac{1}{\sqrt{2\pi\sigma_y^2}} \exp\left[-\frac{\left(\overline{a_x} - a_x\right)^2}{2\sigma_y^2}\right] \tag{2.19}$$

where σ_y is the rms vertical beam size, a is the target aperture size, $\overline{a_x}$ is the offset of the beam centre with respect to the slit centre and a_x is the offset of each electron of the beam with respect to the slit centre [43].

In [79], the expression for the DR vertical polarisation component convoluted with a Gaussian distribution is:

$$\begin{aligned} \frac{d^2W_y^{slit}}{d\omega d\Omega} &= \frac{\alpha\gamma^2}{2\pi^2} \frac{\exp\left(-\frac{2\pi a \sin\theta_0}{\gamma\lambda}\sqrt{1+t_x^2}\right)}{1+t_x^2+t_y^2} \\ &\times \left\{\exp\left[\frac{8\pi^2\sigma_y^2}{\lambda^2\gamma^2}\left(1+t_x^2\right)\right]\cosh\left[\frac{4\pi\overline{a_x}}{\gamma\lambda}\sqrt{1+t_x^2}\right]\right. \\ &\left. - \cos\left[\frac{2\pi a\sin\theta_0}{\gamma\lambda}t_y + 2\psi\right]\right\} \end{aligned} \tag{2.20}$$

This model is applicable when the TR contribution from the tails of the Gaussian distribution scraping the target is negligible i.e. approximately when $a \geq 4\sigma_y$.

2.2.3.1 Projected vertical polarization component

The Projected vertical Polarisation Component (PVPC) is a technique which takes the vertical projection (y, parallel to the direction of beam dimension is intended to be studied) of the 3-dimensional (θ_x, θ_y, intensity) DR angular distribution. The y-projection is obtained by integrating over the horizontal angle θ_x as shown in Figure 2.18(a) and (b) [40].

The visibility (I_{min}/I_{max}) of the y-projection is sensitive to the beam size of the electron beam and may be measured as shown in plot (b) of Figure 2.18 [79]. The maximum and minimum intensities of the DR angular distribution must be measured accurately. Measuring the maximum intensity (I_{max}) is straightforward ensuring the detector is not saturated, however the minimum intensity (I_{min} at $t_y = 0$) measurement may be limited by background photons. It is also necessary that I_{min} at $t_y = 0$ is above the camera noise.

Figure 2.18 (c) shows how the visibility curves at observation wavelengths of $0.3\mu m$

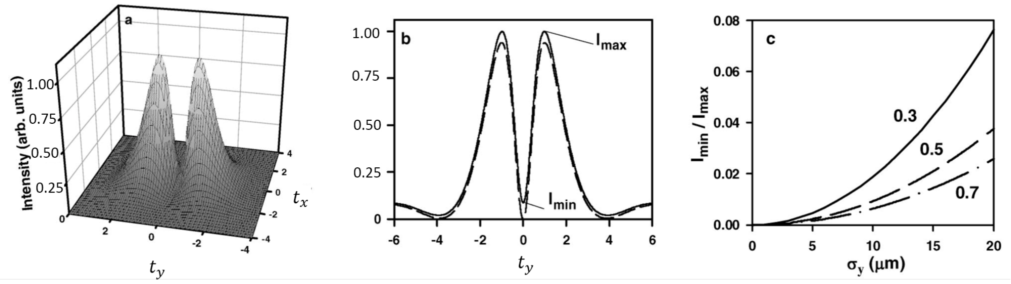

Figure 2.18: A summary of the steps performed in the PVPC technique for beam size measurement [40], a) a 2D intensity distribution of DR vertical polarization from a slit, b) projection along ty, c) plot of the visibility against vertical beam size ω_y.

(continuous line), $0.5 \mu m$ (dashed line) and 0.7 (dashed-dotted line) μm, may be obtained from multiple DR angular distribution images over a range of transverse beam sizes in the case of ATF2 beam parameters ($\gamma = 2544$). Here is it seen that the sensitivity to beam size improves at shorter wavelengths as the change in visibility per micron change in beam size is greater i.e. the gradient of the visibility curve between different beam sizes is steeper [40].

Since the vertical projection is used rather that a single line profile, the PVPC method collects more DR photons emitted from the target. This improves the sensitivity to beam size since the minimum intensity of the DR angular distribution is further displaced from zero above background.

2.2.4 Diffraction radiation interference model

Generally in DR experiments a two-slit setup is implemented where a mask is positioned upstream of the target to reduced unwanted background due to SR. This is also true for the experimental study described in this thesis. However it must not be overlooked that the mask is in effect a secondary target and will also emit DR as the beam passes through the aperture. It is known that FDR produced by the mask interferes with BDR emitted by the target, as observed in the case of TR presented in section 2.1.5. Interference occurs between DR emitted by the mask and target because the separation between the mask and target is comparable to or smaller than the coherence length or formation length already introduced in section 2.1.1.

When this condition is not satisfied, the FDR from the mask must not be ignored. This phenomena, where FDR and BDR, has been described in the literature [80] as Diffraction Radiation Interference (DRI). The model described in this paper is presented here.

The first step of the DRI model considers the field component at the target only. The electric field component with polarisation normal to the slit edge, and parallel to the direction of beam size desired to be measured, is defined as the vertical polarisation field component. The vertical polarisation field component for a single charged particle passing through a slit is represented in the form:

$$E_y = \frac{ie}{4\pi^2 c}\left\{\frac{\exp\left[-\left(\frac{a}{2}+a_x\right)(f-ik_y)\right]}{f-ik_y} - \frac{\exp\left[-\left(\frac{a}{2}-a_x\right)(f+ik_y)\right]}{f+ik_y}\right\} \tag{2.21}$$

where the parameters are defined as follow:

$$\begin{aligned} k &= \tfrac{2\pi}{\lambda}, \\ k_x &= k\sin\theta\cos\phi \approx k\theta_x, \\ k_y &= k\sin\theta\sin\phi \approx k\theta_y, \\ \eta &= \tfrac{k}{\beta\gamma}, \\ f &= \sqrt{k_x^2+\eta^2} \end{aligned}$$

where $k_{x,y}$ are the components of the wave-number k [80]. The DR intensity is obtained from the field component using the relation presented in Equation 2.15 where for simplicity the constants have been omitted.

The polar angles θ and ϕ are defined in Figure 2.19. $\phi = \pi/2$ and a range of θ is chosen to observe the vertical angular distribution. Thereby the vertical angular distribution is obtained, so the observation angle $theta$ may be replaced by θ_y because $\theta_x = 0$ for $\phi = \pi/2$.

In the case of a two-slit setup (mask and target), Equation 2.21 must be modified to include the phase difference between the FDR and BDR amplitudes due to the difference in speed between the charged particle and radiation. This results in an emission delay of BDR at the second target with respect to the FDR wave front emitted at the mask. Including these effects and neglecting the constant coefficient the resulting vertical electric field component produced by two perfectly centred slits can be written as:

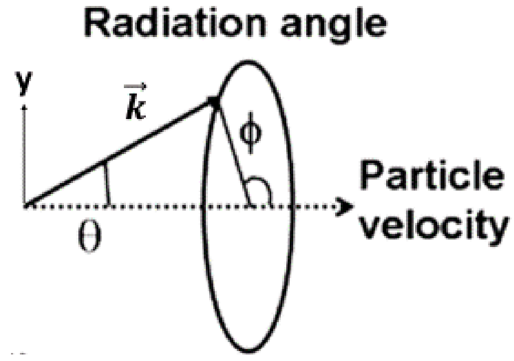

Figure 2.19: Coordinate system used in the DRI model from [80], θ is the angle between the wave-vector ($\vec{k}$) and the particle trajectory, ϕ is the polar angle in the plane of observation.

$$
\begin{aligned}
E_y = \frac{ie}{4\pi^2 c}\Bigg[&\left\{\frac{\exp\left[-\left(\frac{a_1}{2}+z_1\right)(f-ik_y)\right]}{f-ik_y} - \frac{\exp\left[-\left(\frac{a_1}{2}-z_1\right)(f+ik_y)\right]}{f+ik_y}\right\} \\
&- \exp(i\Phi_0)\left\{\frac{\exp\left[-\left(\frac{a_2}{2}+z_2\right)(f-ik_y)\right]}{f-ik_y} - \frac{\exp\left[-\left(\frac{a_2}{2}-z_2\right)(f+ik_y)\right]}{f+ik_y}\right\}\Bigg]
\end{aligned}
\tag{2.22}
$$

where $\Phi_0 = \frac{2\pi d}{\beta\lambda}(1-\beta\cos\theta)$, a_1 is the mask aperture size, a_2 is the target aperture size, d is the distance between the mask and target, z_1, z_2 are the vertical positions of a particle with respect to the centre of the mask and the target slit respectively.

The DRI model describing the vertical, field given in Equation 2.22, makes the assumption that all FDR emitted from the mask is completely reflected by the target. In reality, this is not the case since the target is not a screen but has an aperture through which some FDR photons might pass. Therefore a part of the FDR distribution will be diffracted through the target slit. However, when the mask is larger than the target aperture this effect will be small.

2.2.4.1 DRI simulations

A Monte Carlo approach was implemented to simulate the angular distribution given by a Gaussian beam described by its vertical size and divergence. The vertical positions of particles with respect to the centre of the SR mask (z_1) and the DR target (z_2) slits are dictated by the particles trajectory, which in turn is related to the beam divergence and the longitudinal distance between the mask and the target [81]. A sample of 5000 (z_1, z_2) pairs for a given beam emittance were considered to calculate the distribution of the DR pattern in the far-field. The expression used for the vertical polarisation electrical field (E_y) of a single electron crossing the mask slit of aperture a_1 and the target slit of aperture a_2, located at distance d, taken from the model previously introduced (section 2.2.4), is expressed by Eq. 2.22. Then the intensity distribution of DR emitted by the beam, moving through the mask and target slits, is obtained summing the square modulus of the electrical field of all samples.

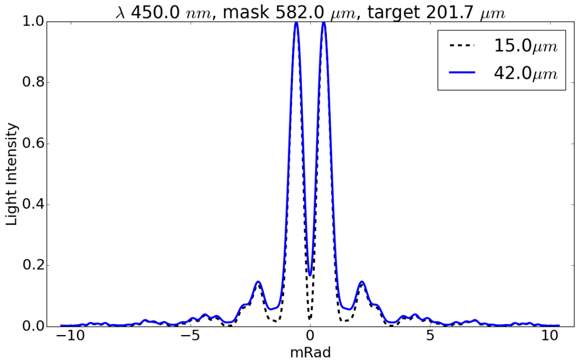

Figure 2.20: PVPC of DRI angular pattern at ATF2 obtained with the DRI model.

Two normalized PVPCs (see section 2.2.3.1) obtained from simulations at $\lambda = 450\,nm$, target slit $= 201.7\,\mu m$ and mask slit size $= 582.0\,\mu m$ are shown in Fig. 2.20. These parameter values were chosen because they reproduce some experimental conditions of the set-up. One may notice that two profiles corresponding to different beam sizes at the target (15 and 42 μm) and with the same beam divergence present the same angular positions for the peaks but a different visibility, defined as the ratio between the value of the centre of the angular pattern and the value of the main peaks (see section 2.2.3.1). With this simulation tool a range of parameters was scanned and the visibility (I_{min}/I_{max}) has been computed as a function of the beam size. The value of the visibility for different beam sizes is depicted in Fig. 2.21 for the usable target slit sizes at the experimental station at ATF2 (section 3.3) for an observation wavelength $\lambda = 400\,nm$.

The points represent simulated values of the visibility and the lines are polynomial fits of second order. It can be seen that the sensitivity increases with decreasing slit size. However, it is also clear that the far-field DR technique has a lower limit of measurable beam size of few microns.

Another very interesting observation about the observation wavelength can be de-

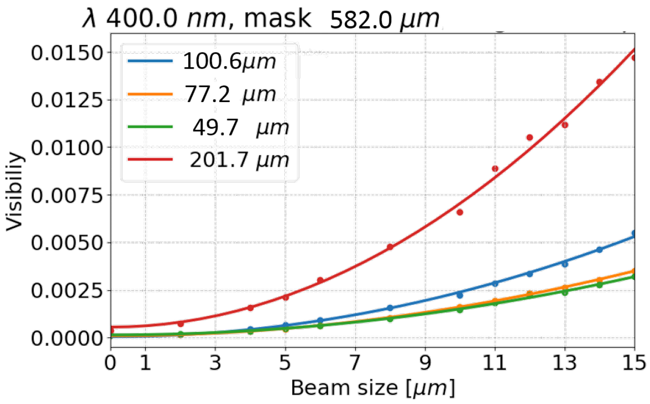

Figure 2.21: Visibility plot of simulated Gaussian beams for different target slit sizes: the wavelength considered for the simulation λ is $400\,nm$, the mask slit size is $582\,\mu m$. The values of mask and target slit sizes chosen for the plot represents the slits used during the experimental campaign (see section 3.4).

ducted from the application of the DRI model as illustrated in Fig. 2.22. Here the tendency of visibility against the beam size for different observation wavelengths is shown. In a similar way of the previous figure, the points represent simulated values of the visibility and the lines are polynomial fits of second order. In particular in Fig. 2.22 it can be seen that decreasing the observation wavelength (from $400\,nm$ to $250\,nm$) the sensitivity increases. This means that moving from the visible range to the UV range increase the sensitivity to small beam sizes allowing the measurement of beams of a few microns.

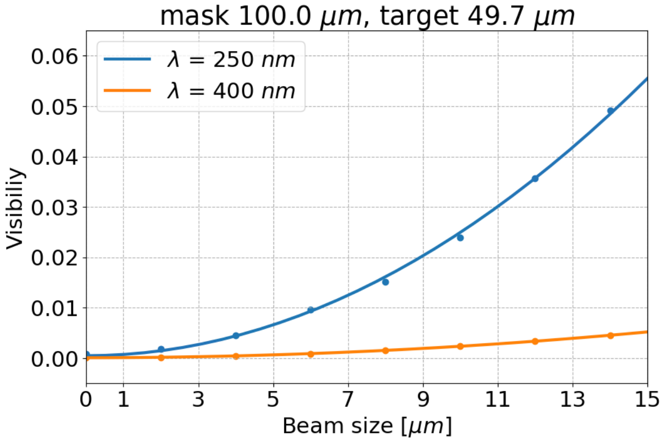

Figure 2.22: Visibility plot of simulated Gaussian beams for different wavelengths in the case of a mask slit size of $100\,\mu m$ ad a target slit size of $49.7\,\mu m$.

Chapter 3

Experimental Station at Accelerator Test Facility 2

The Accelerator Test Facility (ATF) [82], at the High Energy Accelerator Research Organisation (KEK) [83] in Tsukuba (Japan), is a test accelerator focused on generating a super low-emittance beam, that is one of the essential properties needed to realize the next electron-positron linear collider (ILC, International Linear Collider). The ATF is a model of the injector accelerator complex for a linear collider. It consists of a photocathode electron gun, a 1.3 GeV linac, a 1.3 GeV damping ring (small beam storage ring), and an extraction line for beam diagnosis. Initial work on ATF began in 1990. Following the commissioning of the 1.5 GeV linac, operation of the damping ring began in 1997, and the goal for the design low vertical beam emittance was achieved in 2001 [84, 85].

ATF2 is an international project to build and operate a test facility for the final focus system that is envisaged at ILC [51]. This upgrade was built and the first beam test at ATF2 started in December 2008.

3.1 ATF2 layout

The ATF accelerator test facility is composed of a photocathode giving electrons to a linac accelerating the particles to 1.3 GeV followed by a damping ring (see Fig. 3.1).

When in 2008 the facility was upgraded to the ATF2 project [86], the existing machine was extended with a 100 m beam delivery system consisting of an extraction line and final focus line which are an energy-scaled version of the final focus system (FFS) designed for the ILC (described in section 3.1.3). The goals of the ATF2 project are to

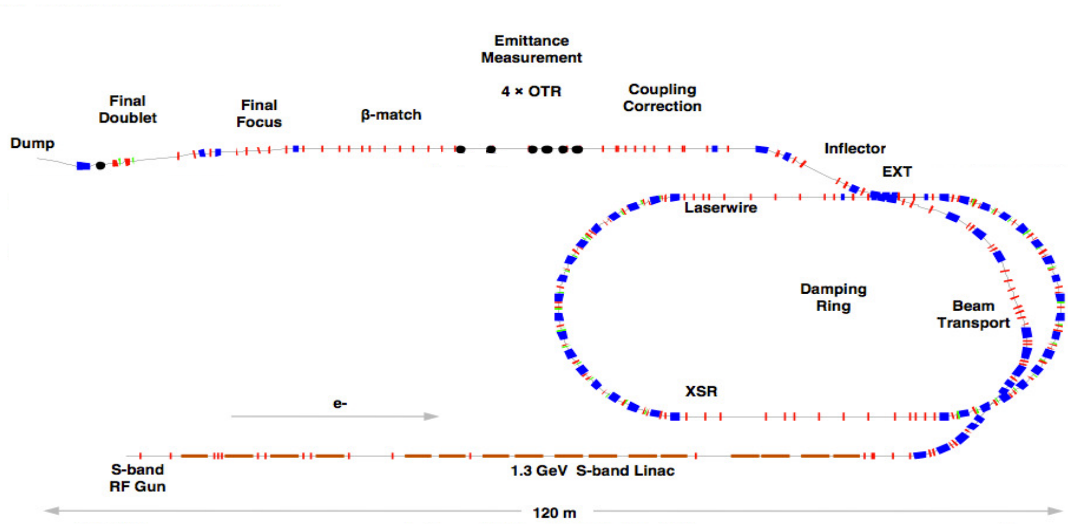

Figure 3.1: Schematic layout of the ATF: on the bottom part the linac, then on the left the dambing ring and top part the extraction line.

achieve a 37 nm vertical beam size at the IP (**goal 1**) and to stabilize the IP beam position at the level of few nanometers (**goal 2**) [86]. The main ATF2 design parameters are given in Table 3.1.

The ATF subsystems are described in detail in the next sub-sections, paying particular attention to ATF2 line, where the experimental station has been installed.

Table 3.1: ATF2 design parameters.

Parameter	**Symbol**	**ATF2 design**
Beam energy	$\sqrt{s}$ [GeV]	1.3
Energy spread	σ_δ [%]	[0.06,0.08]
Final quad to IP distance	L^* [m]	1
Normalized horizontal emittance	$\varepsilon_{x,N}$ [μm]	2.8
Normalized vertical emittance	$\varepsilon_{y,N}$ [nm]	31
Horizontal emittance	ε_x [nm]	2
Vertical emittance	ε_y [pm]	12
Horizontal β function at the IP	β_x^* [mm]	4
Vertical β function at the IP	β_y^* [μm]	100
Horizontal beam size at the IP	σ_x^* [μm]	2.8
Vertical beam size at the IP	σ_y^* [nm]	37
Natural vertical chromaticity	ξ_y	10000

3.1.1 Source and linac

An 18 m long 80 MeV pre-injector section and a 70 m long regular accelerator section with energy compensation structures form the 88 m long ATF linac. The CsTe photocathode driven by a multi-bunch UV laser is coupled with a 1.6 cell S-Band RF gun. The RF gun generates an electron beam with intensities up to 3.2 nC per bunch. The particle trains containing up to 20 bunches of up to 2×10^{10} particles per bunch are accelerated by eight RF units of accelerating gradient of 35.2 MeV/m [87]. The beam energy at the linac exit can reach a maximum energy of 1.54 GeV, while 1.3 GeV is the usual beam energy used during recent operation. To accommodate 5 circulating bunch trains in the damping ring the linac is operated at a repetition rate of 25 pps (pulses per second). The main parameters of the ATF injector linac are shown in Table 3.2 [82].

Beam energy, E_{beam}	$\leq 1.54\,GeV$
Bunch population, N	$\leq 2 \times 10^{10}$
Bunches per train, N_b	≤ 20
Bunch spacing, Δt_{bunch}	2.8 ns
Energy spread full width, σ_δ	$< 1.0\%$ ($90\% \sim beam$)
Normalized emittance, $\varepsilon_{Nx,y}$	$< 3 \times 10^{-4}$ m

Table 3.2: Basic design parameters of the ATF injector linac.

3.1.2 Damping ring

The ATF damping ring has circumference of 138.6 m. It is a storage ring with a race-track shape (Fig. 3.1). The arcs of the ring are based on the FOBO type cells, where B stands for a combined function bending magnet with horizontal defocusing. To reach a small equilibrium emittance the dispersion function is minimised in the bending magnet (see Fig. 3.2) [88]. A 714 MHz RF cavity giving 330 harmonic numbers and 165 buckets with 2.8 ns spacing is used to compensate beam energy loss due to the synchrotron radiation.

In 2004 a vertical normalized emittance of $15\,nm$ ($6\,pm$ of geometrical emittance) was measured for a bunch intensity of 10^{10} particles as reported in [85]. This result was achieved by a precise alignment of components and beam control. During recent beam operation periods usual values of the horizontal and vertical DR geometrical emittance are $< 2\,nm$ and $< 10\,pm$, respectively. The X-ray Synchrotron Radiation (XSR) monitor [89] is used in the damping ring to measure the beam size and therefore reconstruct the emittance. The most useful parameters of the ATF damping ring are summarized in the

Table 3.3.

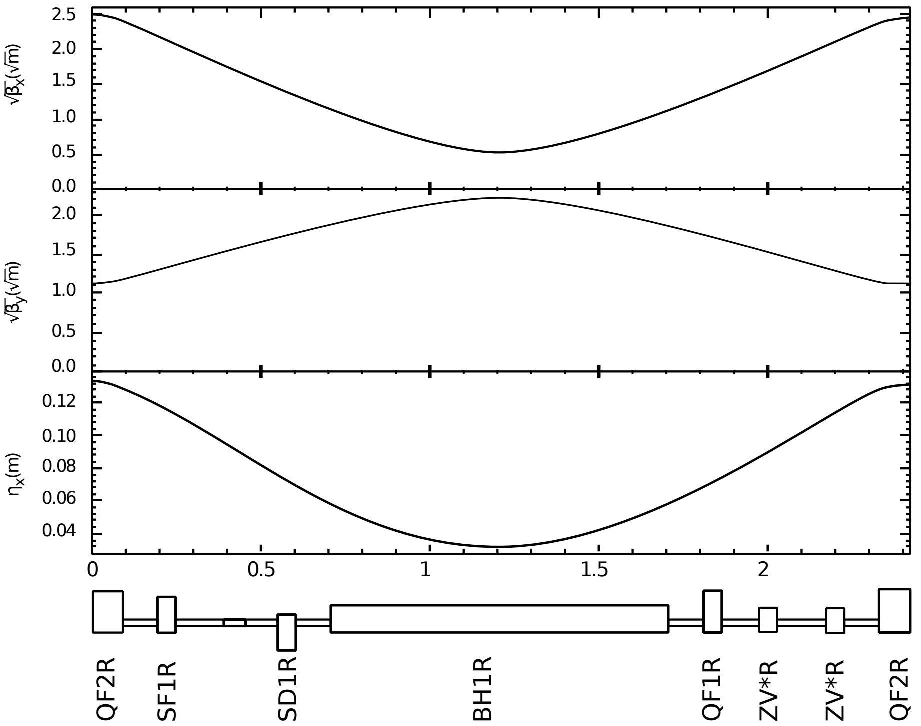

Figure 3.2: Optical functions of a damping ring cell (from [82]).

Circumference	138.6 m
RF frequency	714 MHz
Momentum compaction factor	0.00214
Tune (x/y)	15.17/8.56
Damping time (x/y/z)	17/27/20 ms
Normalized emittance (x/y)	2.8×10^{-6} / 1.0×10^{-8} m
Geometrical emittance (x/y)	1.1×10^{-9} / 4.0×10^{-12} m

Table 3.3: Parameters and achieved performance of the ATF damping ring [88].

3.1.3 Extraction line

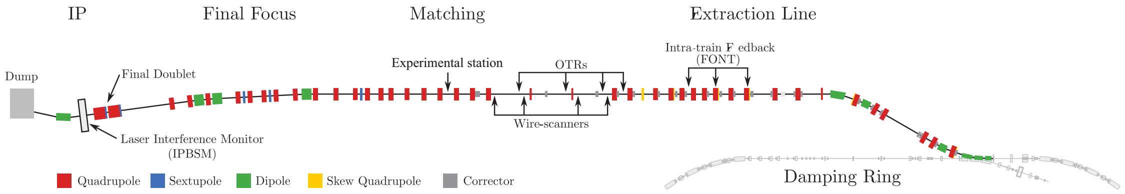

Figure 3.3: Schematic layout of the ATF2 extraction line: the location of the TR/DR experimental station is shown in the Matching section.

The extraction line is presented in Fig. 3.3, showing the location of the DR experimental station.

The beam is horizontally extracted from the damping ring straight section using a pulsed kicker (KEX1) and a current-sheet septum magnet (BS1X). The septum magnet is followed by two strong dipole magnets (BS2X and BS3X) that bend the extracted beam at an angle of about 20°.

Due to undesired magnetic components in the kicker and two DR quadrupoles (QM6R and QM7R) that the extracting beam passes through with a large offset, an x-y beam coupling occurs leading to vertical emittance growth at the extraction location [88].

A *dogleg* inflector is located downstream from the septum dipoles comprising two approximately 10° bends (BH1X and BH2X) that offset the beam by 6 m from the damping ring. The beam is brought parallel to the damping ring straight section by a mirror image of the kicker-septum system composed of two dipole magnets (BH3X and BKX). The BKX dipole replaces the KEX2 kicker that was initially installed in the extraction line. The layout of the inflector system is depicted in Fig. 3.4.

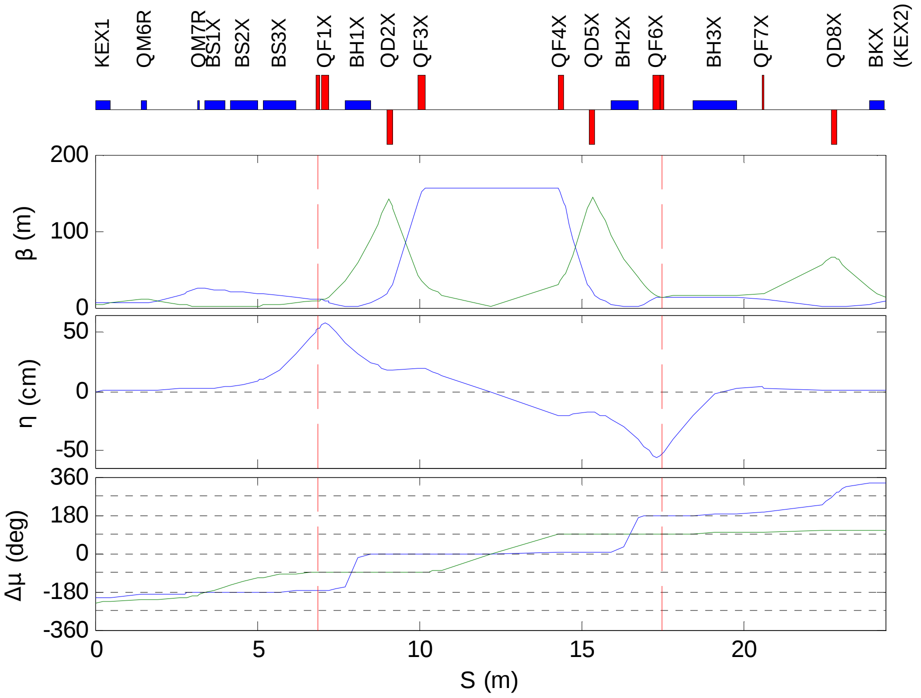

Figure 3.4: Optics of the inflector; horizontal functions are in blue and vertical functions are in green. Upper plot: β function; middle plot: dispersion function; lower plot: phase advance relative to the centre of the inflector. Red vertical lines indicate the position of the quadrupoles QF1X and QF6X (from [88]).

On the extraction line, in a section presents just upstream of the TR/DR experimental station, an emittance diagnostic section is present. The transverse beam emittances are reconstructed by measuring the transverse beam sizes using four Optical Transition Radiation (multi-OTR system) monitors [90] (see Fig. 3.3). These monitors provide fast single-shot measurements with full ellipse-fitting, allowing simultaneous measurement of the projected x and y spot sizes and the x-y tilt of the beam. Beam sizes at the measurement locations for the ATF2 nominal emittances ($\varepsilon_x = 2\,nm$, $\varepsilon_y = 12\,pm$) range from 75 to 155 μm in x, and from 7 to 20 μm in y [88]. However, the multi-OTR system often overestimates the vertical emittance mainly because of the hardware alignment issues and the ambiguity of fitting the beam profile.

The beam orbit diagnostic in the extraction line is handled by 23 beam position monitors (BPMs). There are 12 stripline BPMs, located mainly in the inflector, with a single-shot resolution of about 10 μm, 9 C-band cavity BPMs [91], with sub-micron single-shot resolution and 2 button-type BPMs located near the septum. These BPMs are commonly used during operation to optimize the beam orbit. They were used during the experimental work of this thesis to reduce the Synchrotron Radiation background (see section 4.2).

3.1.4 Final focus system

The final focus system starts with a matching section that adjusts the β functions of the beam coming from the extraction line. The nominal ATF2 optics, referred to as $1\beta_x^* \times 1\beta_y^*$, has $\beta_x^* = 4\,mm$ and $\beta_y^* = 100\,\mu m$. Different optics are referred to with respect to the nominal, for example $10\beta_x^* \times 1\beta_y^*$ optics (see Fig. 3.5). During the experimental campaign performed during this thesis work the $10\beta_x^* \times 1\beta_y^*$ optics was used.

The lattice elements of the ATF2 final focus system are shown in Fig. 3.5. In particular the position of the TR/DR experimental station is indicated by a blue arrow in the picture. This is situated in between quadrupole QM14FF and QM13FF (indicated as QM14 and QM13 in Fig. 3.5). In total the FFS contains 3 dipoles, 4 dipole correctors, 28 quadrupoles, 5 sextupoles and 4 skew-sextupoles.

All quadrupoles and sextupoles are placed on individual movers to allow the beam steering and adjustment of relative alignment in the transverse plane. Adjacent to these magnets, the C-band cavity BPMs [91] with sub-micron single-shot resolution are installed.

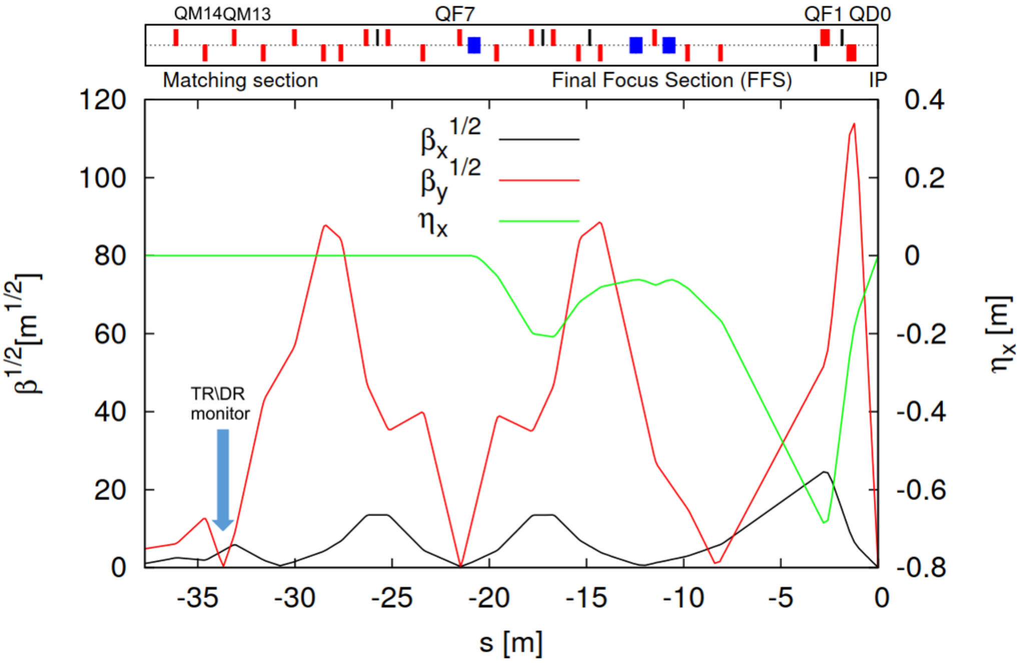

Figure 3.5: Optical functions in the final focus section for $10\beta_x^* \times 1\beta_y^*$ optics. On top is the layout of the ATF2 lattice:dipoles in blue, quadrupoles in red and sextupoles in black. Position of the TR/DR experimental station is indicated by the blue arrow [92].

3.1.5 The interaction point

The ATF2 focal point is called an Interaction Point (IP) in analogy with particle colliders. In fact, the ATF2 provides just one particle beam, so no high-energy collisions occur there. Instead, the ATF2 performance is verified by measuring the IP beam sizes using the so-called Shintake monitor [93, 94]. It is an interference monitor where two laser beams cross in the plane transverse to the electron beam in order to form a vertical standing wave, see Fig. 3.6.

The fringe pattern vertical distribution is modified by changing the phase of one laser path in the optical delay line. The beam size is inferred from the modulation of the resulting Compton scattered photon signal detected by a downstream photon detector, see Eq. (3.1) [35]:

$$\begin{gathered} \mathrm{M} = C\,|\cos\theta|\exp\left[-2\left(k_y\sigma_y\right)^2\right], \\ k_y = \pi/d,\;\; d = \frac{\lambda}{2\sin\left(\theta/2\right)}, \end{gathered} \tag{3.1}$$

where C is the modulation (M) reduction factor which represents the overall systematic effect causing a decrease of the observed modulation due to the monitor imperfections, θ is the crossing angle and $\lambda = 532$ nm is the laser wavelength. Three laser crossing angle

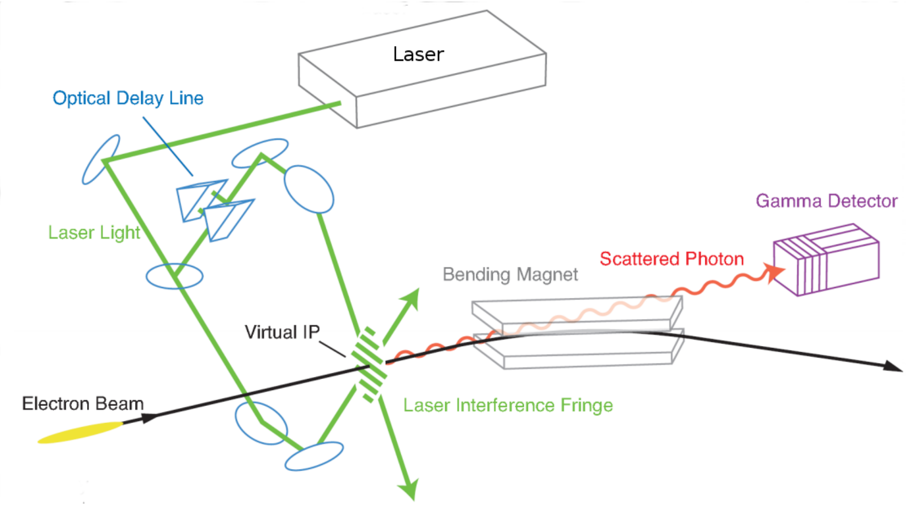

Figure 3.6: Shintake monitor schematic design. The electron beam interacts with a transverse interference pattern generated by two crossing laser beams. The number of scattered photons varies with the fringe size and the particle beam size [35].

modes ($2-8°$, $30°$, $174°$) extend the dynamic range from $1\,\mu m$ to $20\,nm$, where $M > 0.1$, see Fig. 3.7.

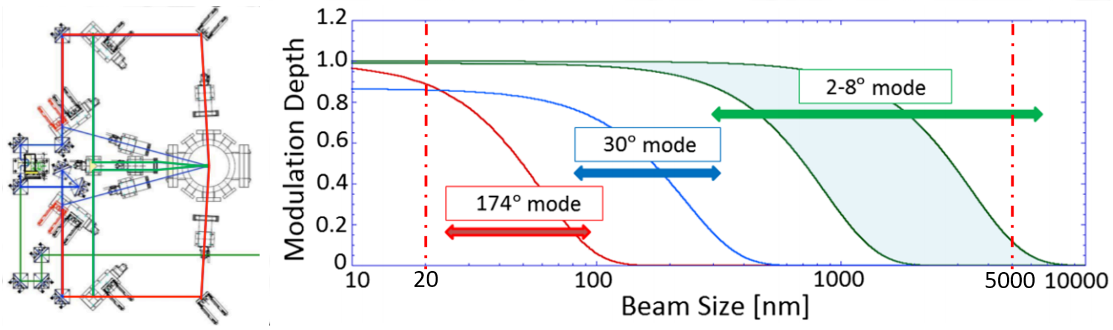

Figure 3.7: (Left) IP beam size monitor laser path over the optical table perpendicular to the beam propagation. (Right) Beam size resolution for the angle modes : $2° - 8°$ in green, $30°$ in blue and $174°$ in red.

Larger beam sizes are measured by a wire scanner installed at the IP. It consists of a carbon wire $5\,\mu m$ in diameter that when moved across the beam generates bremsstrahlung gamma rays. The number of photons is proportional to the charge of the slice interacting with the wire at each position setting. Profiles are constructed from the number of photons as a function of wire position [13].

3.2 Design and installation of the vacuum chamber

The experimental system has been installed in the ATF2 extraction line 3.1.3, in the old laser wire experiment location [95] (between the quadrupoles QM14FF and QM13FF) where the beam can be focused to a vertical size varying from few hundreds of nanometres to tens of micrometres [96]. A flexible experimental set-up was designed to study the impact of different parameters on the DR pattern generated by the beam. It mainly consists of a vacuum chamber, connected to the main beam-line, with different ports to allow the access of the instrumentation from outside and to extract the radiation emitted by the interaction of the target with the beam.

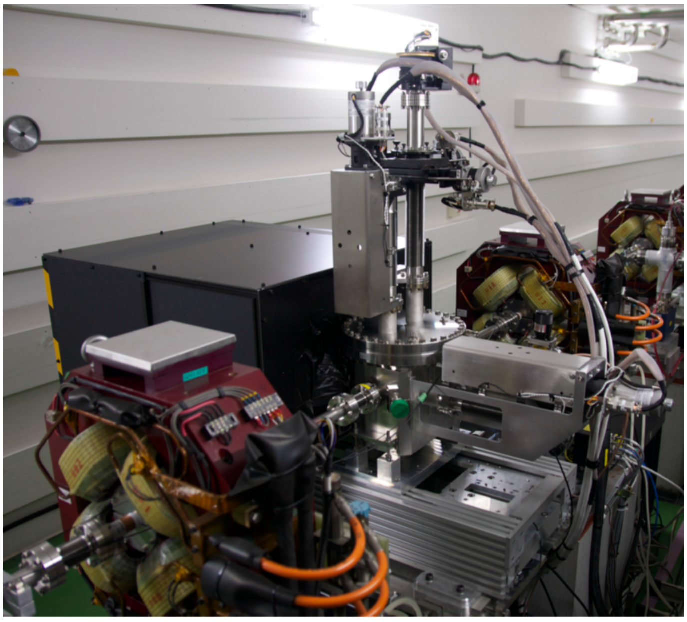

Figure 3.8: ATF2 experimental set-up in the extraction line.

In Fig. 3.8 the whole system installed in ATF2 extraction line is depicted. Fig. 3.9 illustrates the experimental system assembly. As can be seen in the isometric view, the vacuum chamber, on two opposite sides, has two flanges DN40CF (indicated with a blue arrow showing the direction of the electron beam) that allows to connect the tank with the main ATF2 beam line pipe. Two other bigger flanges (DN63CF) present on the front side of the vacuum chamber are equipped with UV-grade fused silica view-ports. These two view-ports are positioned at 40° and 90° with respect to the beam axis as can be seen in the schematic sketch of the tank's internal configuration Fig. 3.10.

As depicted in Fig 3.10, on the upper part of the vacuum chamber two actuators,

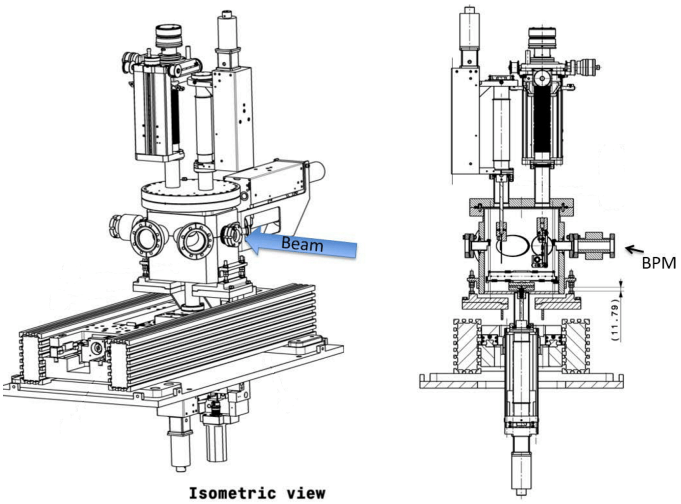

Figure 3.9: Technical drawing of the vacuum chamber as isometric view (left) and viewed from the back (right) showing the replacement chamber (bottom part) and target mechanism (top part).

controlled by stepper motor, are installed on two different flanges to control the vertical insertion of the DR target and a synchrotron light mask. The target and the mask will be described in more detail in section 3.3. On the opposite side of vacuum chamber to the 2 UV-grade fused silica view-ports, another actuator allows the horizontal insertion of another synchrotron light mask. On the same side, are located a couple of small view-ports (DN16CF), tilted with angles of 45° and 135°. These two view-port, with the help of a laser, can be used to align the target and the external optical lines (described in the section 3.4) present on the other side of the chamber.

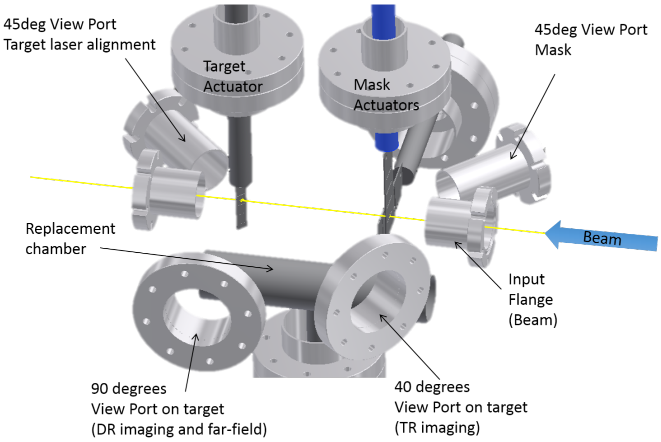

Figure 3.10: ATF2 Tank internal configuration.

Another important element of the design, presented both in Fig 3.9 and Fig 3.10, is the replacement chamber. When the DR target and mask are not inserted in the beam line, this element can be raised upward from underneath the chamber to reduce the wake-field effect of the incoming beam. This is obtained firstly using for the replacement chamber a pipe with the same inner diameter as the main ATF2 beam-pipe and secondly, when the replacement chamber is in the upward position (aligned with the beam axis) is connected through copper RF contact gaskets to the main beam line.

To obtain a micrometre precision in the movement of all component the actuators are controlled with stepper motors and encoders throw a control system that will be described in detail in section 3.5.

3.3 Target design and production

The DR target consist in a 1mm thick silicon substrate cut with a rectangular shape ($20\,mm \times 75\,mm$) from a silicon wafer, as shown in Fig. 3.11 where the target and SR mask are depicted in grey installed on the holders that allow the suspension on the actuators shaft. Both on the target and on the SR mask, 4 rectangular slits, with different vertical aperture size, were produced on the silicon substrate through chemical wet anisotropic etching based on use of potassium-hydroxide (KOH) [97–99]. All the slits have an horizontal size of 8 mm. The 4 slits on the target have the following vertical dimensions: 201.7 μm, 100.6 μm, 77.2 μm and 49.57 μm. The mask slits were designed to be a factor 2 bigger than the target sits: 399 μm, 198.9 μm, 149.2 μm and 100 μm. The dimensions where precisely measured after the production with a microscope Appendix B.

On the DR target a surface of $2\,mm \times 2\,mm$ on the two side of every slit is coated with aluminum ($30nm$ thickness) to locally increase the reflectively, whereas the remaining part of the target is sandblasted to increase the diffusion of the light. This solution was designed following the outcome of DR experiments performed by our team at Cornell Electron-Positron Storage Ring [100], where it was observed that this target surface configuration helps to decrease the SR light background [44]. On the other hand the front surface of the mask is completely coated with aluminum to obtain a mirror to increase the reflection of the SR light coming from upstream part of the beam line.

Furthermore, the bottom part of the front surface of the DR target (1 cm below the smaller slit) is covered with a $4\,mm \times 2\,mm$ aluminum coating ($100\,nm$ thickness) to create a mirror that can be used as an OTR source, this part of the target was used for sub-micron beam size measurement using PSF technique [23] using an in-vacuum lens very close to the target due to his short focal length (30 mm).

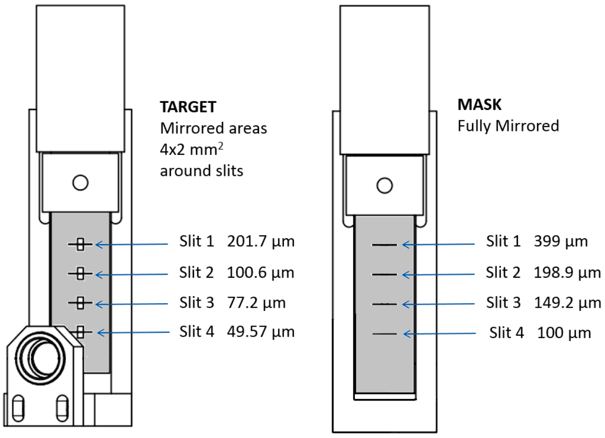

Figure 3.11: ATF2 target and mask: the left drawing represents the target and his support, the sketch on right is the mask and his support. On both illustration are indicated the size of the slits presents.

Fig 3.12 shows how the particle beam passing through one slit on the target, vertically inserted at the right depth, produces backward DR. This radiation points to the view-port at 90° thanks to the tilt angle of the target. The actuator controls the tilt and the insertion with micrometre precision to select the desired slit, to centre it around the beam and to send the radiation to the centre of the view-port.

A horizontal mask, made of steel, is also present. This mask is bigger than the vertical mask and it has 3 horizontal slits with sizes: 2, 4 and 6 mm. Both vertical and horizontal masks can be inserted with stepper motor actuators. When the particle beam passes through the slits of the masks not only is most of the upstream-produced SR blocked but also forward DR is produced. This DR is reflected on the target and it interferes with the backward DR modifying the angular pattern thereby allowing a smaller minimum in between the two main DR peaks to be reached because it removes the majority of SR.

3.4 Optical line

The far-field distribution of a light source is observed by placing the imaging sensor in the back focal plane of a lens [54]. The light is extracted through the 90° view-port, passes through a polarizer (UVT260A-25 from Moktek [101]) to select the desired polarization,

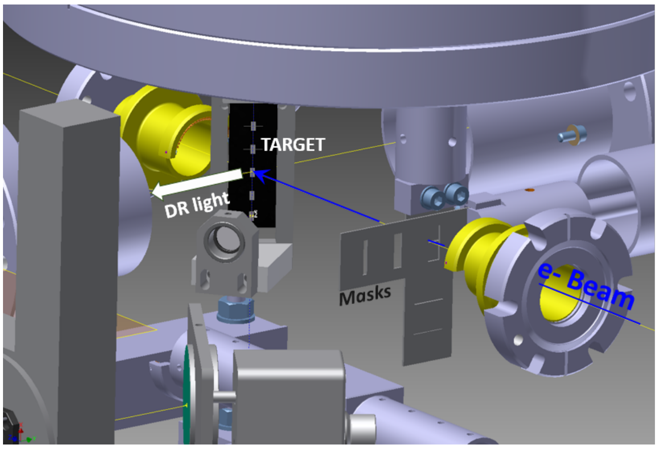

Figure 3.12: Functional view of vacuum chamber: the blue line represents the particle beam trajectory, the white arrow represents the backward DR light direction of propagation.

and, thanks to an optical pellicle beam-splitter (BP208 from Thorlabs [102]), is detected by two independent optical lines: one to create an image of the source, the other to observe the DR angular distribution (Fig. 3.13) as the sensor is placed in the backfocal plane of a lens. This setup allows both imaging and DR angular dristibution to be recorded at the same time [81]. The imaging line is used as an optical BPM, with the beam position deduced from the intensity imbalance between the two slit edges [103].

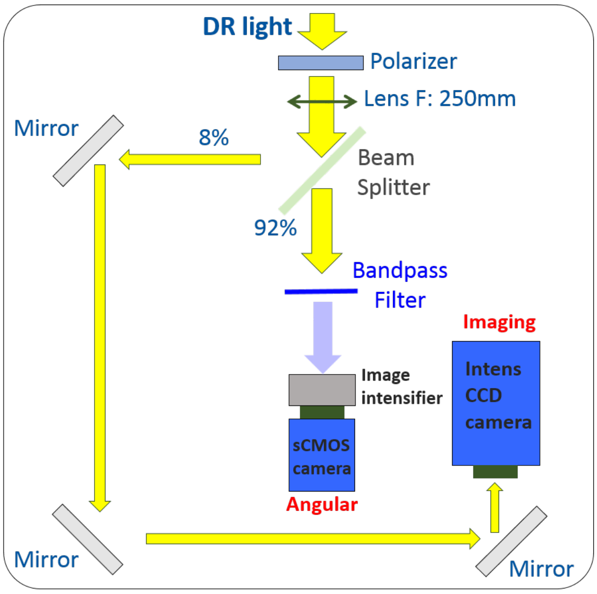

Figure 3.13: ATF2 optical line schematics: the yellow arrows indicate the DR light path in the optical line.

Fig. 3.13 and Fig. 3.15 show how a 2-inch diameter lens with focal of 250 mm (LA4538 from Thorlabs [104]) is installed before the beam-splitter so that it is used for both optical lines. The lens chosen is made of UV fused silica without any coating to allow light transmission ($> 90\%$, see Fig. 3.14) from the UV (200 nm) to the visible wavelength range up to 700 nm.

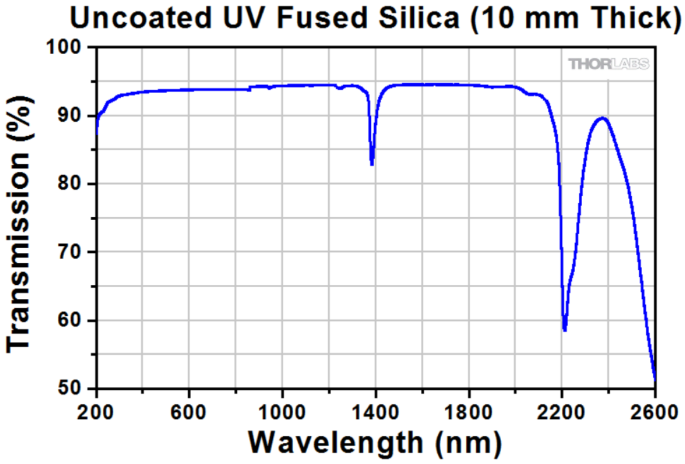

Figure 3.14: Transmission of LA4538 lens for different wavelengths from [104].

The imaging optical line consists of three 2-inch UV enhanced aluminum mirrors (PF20-03-F01 from Thorlabs [105]) that collect the light reflected by the beam-splitter (8%), to direct the radiation to a gated intensified CCD camera (dicam pro with GaAs photocathode from pco [106]). The mirrors, suitable for 250 nm to 700 nm spectral range, were chosen to increase the distance between the lens and the camera in the limit of the optical table dimensions to have the desired magnification on the CCD ×1.8 after de-magnification due to the internal intensifier CCD optical coupling. In fact, inside the intensifier sits a Micro Channel Plate (MCP); on the back surface of the MCP a phosphorus screen is coupled with the CCD with 3:2 optical ratio.

The angular distribution optical line has a the detection system directly in front of the beam-splitter so that it can collect 92% of the radiation transmitted. A remotely controlled filter wheel (FRM 40-6-D25-HSM from OWIS [107]) with a set of 1 inch band-pass filters were installed just before the detector to select different observation wavelengths and bandwidths. The filters used during data acquisition are the following: Thorlabs FB400-10 (center peak wavelength 400 nm, FWHM bandwidth 10 nm), Thorlabs FB400-40 (center peak wavelength 400 nm, FWHM bandwidth 40 nm, Thorlabs FB600-40 (center peak wavelength 600 *nm*, FWHM bandwidth 40 *nm*) [108], eSource optics 25250FBB (center peak wavelength 250 nm, FWHM bandwidth 40 *nm*) [109] and Andover 232FS10-25 (center peak wavelength 232 *nm*, FWHM bandwidth 10 *nm*) [110]. The detector is an gated image intensifier unit coupled with sCMOS camera. The intensifier (C9547-04 from Hamamatsu [111]) is a double stage MCP with a multi-alkali photocathode sensible down to 200 *nm* wavelength. The camera, chosen for the very low readout noise (a mean value 0.8 electrons), is a scientific CMOS from pco (edge 4.2LT) [112]. The camera and the intensifier, coupled with a relay lens A11669 from Hamamatsu, are installed on remotely controlled translation stage (T-LSR150B-KT04 from Zaber Technologies [113]) to scan across the direction of the incident light to find the back focal plane of the lens for the different observation wavelengths. Since the image intensifier technology is based on an MCP tube, they can be gated to very short time window (20 *ns* the pco and 5 *ns* the hamamatsu). This allows the background noise to be significantly reduced, thereby increasing the signal to noise ratio.

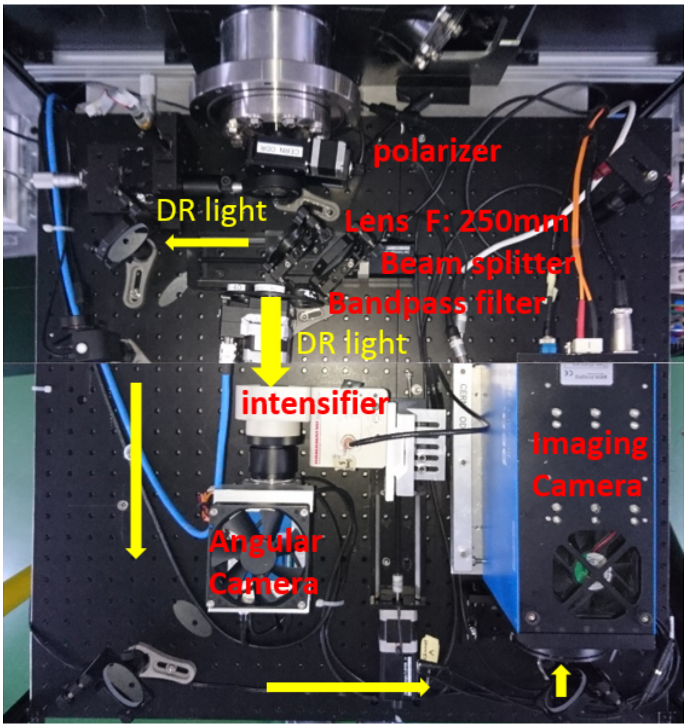

Figure 3.15: ATF2 optical line picture: the yellow arrows indicate the DR light path in the optical line. The Angular camera is the CMOS camera (pco edge 4.2LT [112]), the Imaging camera is the intensified CCD (pco dicam pro [106])

3.5 Data acquisition and hardware control

The experimental station was designed to study the effect of several parameters, as already mentioned, so the possibility to move different elements of the system remotely is a key point of the design. This led to the presence of 4 vacuum actuators for target, masks and replacement chamber manipulation; 2 optical translation stages; a motorized filter wheel; and a motorized rotational stage for the polarizer. All of them are controlled with stepper motors (7 for the vacuum actuators, 4 for the optical mover) because they allow very good precision and reproducibility. To increase the accuracy of the target and mask actuators, limited by the backlash down to the micron level, and needed by the dimension of the slits, magnetic encoders (LA11 and LM13 from Renishaw) are used.

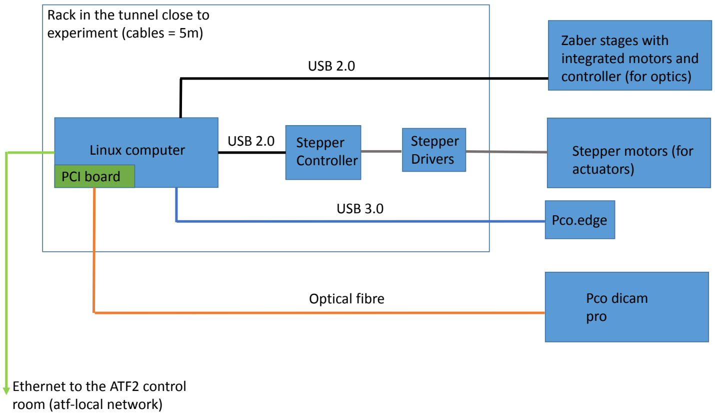

Figure 3.16: Hardware control system schematics: pco edge [112] is the camera to record the DR angular distribution, pco dicam pro [106] is the camera used to image the DR target

In Fig. 3.16, a block-diagram that illustrates the schematics of the hardware control chain is presented. A rack-mount industrial computer (operating Linux version Cern Centos 7) is installed close to the experimental set-up in the ATF2 accelerator tunnel. Inside the same rack the stepper motor controller and drivers (ZMX+ from Phytron) are present and controlled by the computer via USB. This specific configuration was chosen as it is the standard solution implemented by the BE-BI-PM section at CERN. The sCMOS camera (pco edge 4.2 LT) communicates via USB 3.0 with the computer. The CCD camera (pco dicam pro) has an optical fiber connection using a PCI board installed on the linux computer. To synchronize with the beam the gate time window, the intensifier and the cameras receive a reference trigger signal from the ATF2 timing system thanks to coaxial cables. The stepper motors installed on vacuum actuators and on the filter wheel are controlled by the stepper driver in the rack, the translation stages and the polarazier stepper (from zaber) integrate a controller so that they are connected directly to the computer via USB. Finally the computer is connected on the local ATF2 technical network through Gigabit ethernet.

3.5.1 Software

The data acquisition system was developed in C++, using the open source QT libraries [114] to create a Graphic User Interface to control simultaneously both cameras. The 2D images acquired with the cameras are saved in FITS format allowing to register also information about the beam and the instrument inside the image header. The software make use of the Experimental Physics and Industrial Control System (EPICS) [115] a control system in use at ATF2. The software to control the stepper motor of the experimental station control, written with Python language at CERN, was modified to communicate also through EPICS. Thanks to EPICS it is possible to record with the data (in the header of the image) not only beam parameters, from other instrument present on the beam-line (e.g. beam charge), but also hardware control parameters of the experimental station. This information is really useful for post-acquisition data analysis. Furthermore, controlling the system through EPICS allows the implementation of automated scans of beam-line elements (e.g. Quadrupole scan) while collecting data.

The offline data analysis has been performed with Python scripts, developed for this thesis, to analyse 2D images to extract information about DR and TR radiation. Specifically, for each image the experimental background, obtained form the portion of the image where the TR or DR are not present, is subtracted. Furthermore vertical and horizontal integrated projections, as figures presented in the next chapter, can be calculated, plotted and processed to obtain visibility values for every DR or TR image.

Chapter 4

Experimental Results and Discussion

In this Chapter the results of the experimental study for small beam size (micrometre scale) measurements using DR and TR in the visible and UV range are presented. The first part describes the commissioning phase of the DR/TR monitor, in particular the alignment and the calibration of the optical lines described in Chapter 3. All the optimizations performed during data recording shifts at ATF2 such as the studies to minimize the SR contribution are also presented here. DR measurements were obtained using single shot images, meaning recording the DR pattern produced by a single bunch of electron (energy $1.3\,GeV$). If averaging or summation of multiple images from a single buch was used in the post-acquisition analysis this is indicated in the text. The single electron bunch charge was always between $0.4\,nC$ and $0.6\,nC$, recorded for every data point as explaind in section 3.5. The main results presented are for DRI measured successfully in the UV range where a sensitivity down to beam size as small as $3\,\mu m$ is shown.

4.1 Commissioning of the experiment

Measuring micrometre size beam requires a careful alignment of every element of the experiment. As already introduced in the previous Chapter (section 3.2), the DR target and mask can be moved during beam operation with a micrometre precision, thanks to remotely controlled stepper motor and encoders. However, all optical elements must be aligned just after the installation, knowing nothing else but the expected position of the beam. Here the procedure to align and prepare the optical line in the tunnel to be able to observe directly an image during the beam operations without scanning too many position of movers is described in detail in the following sections. Furthermore the calibration procedures of the optical lines are also described.

4.1.1 Alignment laser

To align all optical elements previously described in section 3.4 an alignment system was used. This alignment system, formerly used for another experiment at ATF2 [50] was adapted to the new DR monitor. As depicted in in Fig. 4.1, the alignment system consists of a laser system and a vacuum mirror. The laser system consists of a laser stage, a He-Ne Continuous Wave (CW) laser ($\lambda = 632.8\,nm$) from Melles-Griot, a spatial filter, and a focusing lens [50].

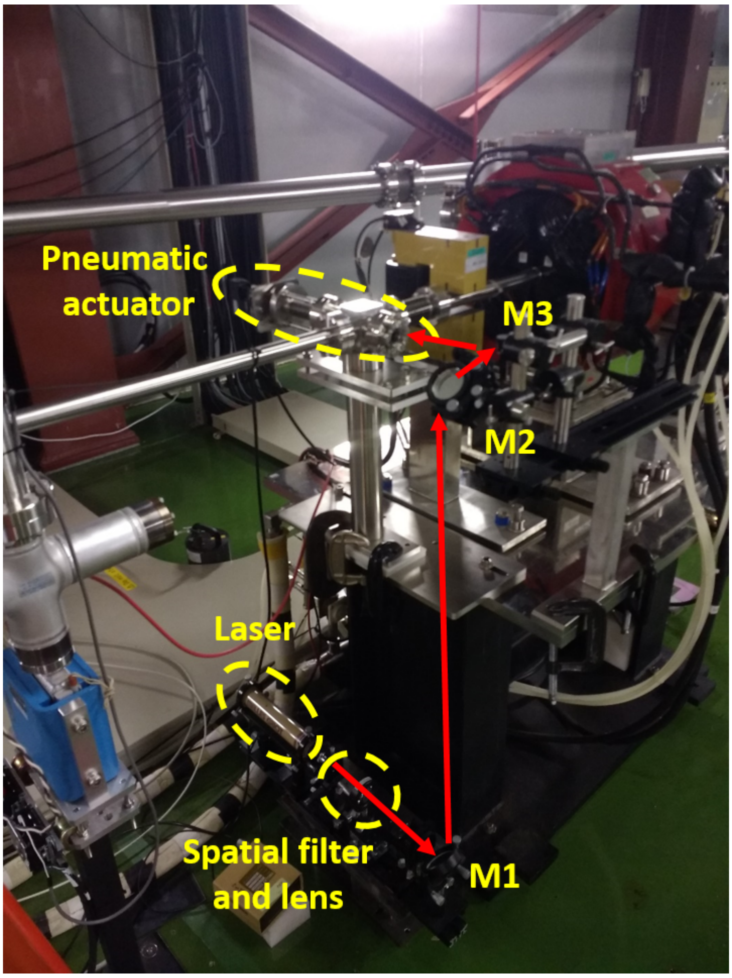

Figure 4.1: Alignment laser: the laser is installed underneath the beam line, the light emitted follows the red arrow in the picture. It passes through a spatial filter, a focusing lens, the periscope mirrors (M1 and M2) and the last mirror (M3) before entering the beam pipe and being reflected in the beam direction thanks to the in-vacuum mirror.

Changing the distance between the spatial filter and the lens, the laser can be focused at any point of the experimental setup. The laser is placed below the beam line (Fig. 4.1). Two periscope mirrors (M1 and M2 in Fig. 4.1) bring the laser up to the level of the beam orbit. Another mirror (M3 in Fig. 4.1) sends the light in the beam line. The in-vacuum mirror, inserted in the beam line by a pneumatic actuator, reflects the laser light along the beam line. The laser spot is observed on the imaging line detector because it is reflected by the mirrored surface of the DR target inserted at the center of the beam pipe (section 3.3).

The pneumatic actuator and the laser are remotely controlled, allowing the system to be switched on and off during accelerator operation to control the relative position of the laser with respect to the electron beam on the target. In the case when they do not coincide, the laser direction can be corrected using the two periscope mirrors. Once the optimal position is found, every element of the detection optic is precisely aligned with respect to the laser spot. It has been demonstrated experimentally that the alignment accuracy is better than $1/\gamma = 0.4\,mrad$, which is more than enough for our purpose.

4.1.2 Slits alignment and magnification calibration of the imaging optical Line

Once the DR target is aligned with the electron beam position, as described in the previous subsection, the vertical position of each slit is found by controlling the vertical translation mechanism of the target. Using the laser, also the mask slit is precisely aligned with respect to the target slit using a similar technique: the target is kept in the desired position and the shadow of the mask created by a sufficiently large laser spot ($5\,mm$ radius) passing through the mask is observed with the imaging line.

Figure 4.2(a) presents an image of the $201.7\,\mu m$ target slit (see section 3.3) recorded with the CCD camera on the imaging line. The aperture of the slit on the imaging camera is measured observing the two edges of the vertical projection of the image shown in Fig. 4.2(b).

The target has 4 DR slits, as explained in section 3.3 of the previous Chapter. This fact allows all the slits to be used to measure the magnification simply using different target vertical insertion positions. Specifically, several measurements are collected for each target slit and a plot of the slit sizes on the object plane (real slit) versus slit sizes measured on the CCD is shown in Fig. 4.3. The data are described by a linear fit $y = Mx$, where y is the slit size on the CCD (image plane), x is the real slit size (object plane) and

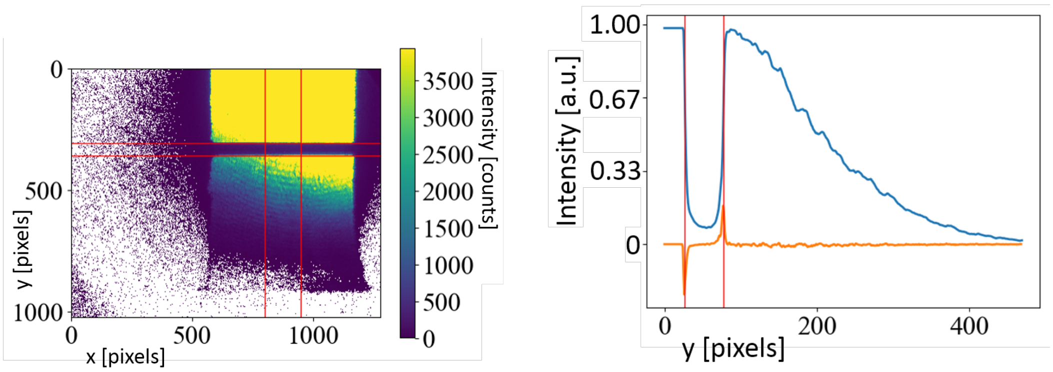

(a)

(b)

Figure 4.2: Target slit imaging calibration: (a) 2D image of the 201.7 μm slit; (b) blue curve is a part of the vertical projection (between the two vertical red line in image (a)) of the slit, the orange profile is the derivative of the blue curve and the two vertical red lines are the position of the maximum and minimum values of the orange curve. The measured slit size from the image is the number of pixel measured between the two red lines multiplied by the pixel size (6.7 μm in this case).

M is the magnification. The magnification measured is $M = 1.82 \pm 0.01$, that gives an equivalent pixel size on the magnified image of 3.72 μm considering the fact that the real CCD pixel is 6.7 μm.

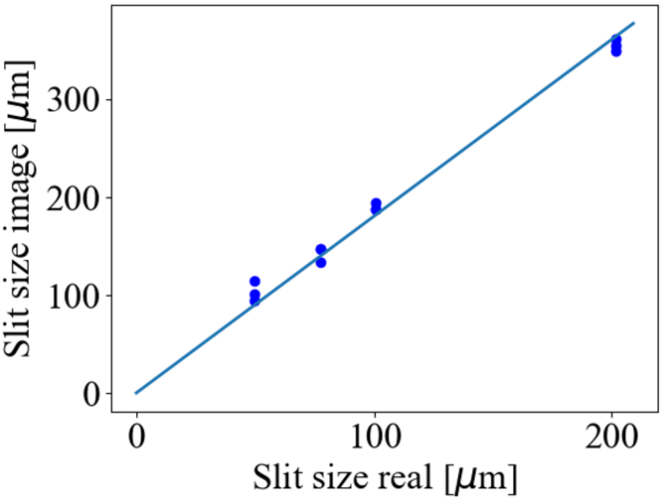

Figure 4.3: Target slit imaging calibration curve size of the different slits on the camera versus real slit sizes: blue dots are recorded points, light blue line is a linear fit $y = Mx$.

4.1.3 Calibration of the angular optical line

The angular optical line measures the angular distribution of TR or DR from the target, as introduced in section 3.4. Since the lens used to recreate the far-field condition is not achromatic, the position of the back-focal plane changes for different wavelengths in particular a significant shift of $\approx 2\,cm$ can be observed passing from the visible light at $450\,nm$ to the UV at $250\,nm$. The practical technique of imaging a light source very far from the lens was used, because the back-focal plane of the lens can be found by minimizing the spot size of focused light coming from an infinite distance. The light source was positioned at the end of the ATF2 tunnel giving a source to lens distance of $\approx 35\,m$. This distance was verified with Zemax simulation to be a good approximation of an infinite distance: the back focal plane of the lens, found minimizing the spot size on detector plane, from parallel rays coming from infinite distance and from $35\,m$ was the same within 0.1%. For all visible wavelengths filters ($400\,nm$ and $600\,nm$) a broad-band white source was used. On the other hand for the UV filters ($250\,nm$ and $230\,nm$) an AlGaN based deep UV LED Lamp (UVCLEAN255-5 from QPhotonics) was chosen.

The angular optical line needs to be carefully calibrated to be able to know the corresponding angular size of a single pixel for every position of the back-focal plane (different wavelengths). This calibration is obtained rotating the target around its vertical axis, the rotation is measured with the rotational encoder (resolution $\approx 32\mu rad$) on the actuator. At the same time, an image of the vertical polarization of the TR angular profile with the angular line camera (see section 3.4) is recorded. This procedure is repeated for 9 different angles inside the field of view of the optical system for every wavelength. Then the relative rotation is associated to the pixel position on the CMOS sensor of the horizontal centre of TR angular pattern.

To explain this procedure the reader can refer to Fig. 4.4(a) which shows a 2D image of the vertical polarization of the TR angular distribution taken at $400\,nm$. The horizontal projection of this image, depicted in Fig. 4.4(b) (blue curve), is fitted to find the pixel corresponding to the horizontal centre position of the TR pattern (red vertical line in Fig. 4.4(b)). This position is then plotted in Fig. 4.5 against the rotation angle in $mrad$. Finally a linear fit is applied to obtain a calibration of $51.0 \pm 0.1\,\mu rad$ per pixel at $400\,nm$ and $56.0 \pm 0.1\,\mu rad$ per pixel at $250\,nm$. These values are not expected to be equal as the lens is not achromatic so it has a different focal length (i.e. magnification) for such different wavelengths.

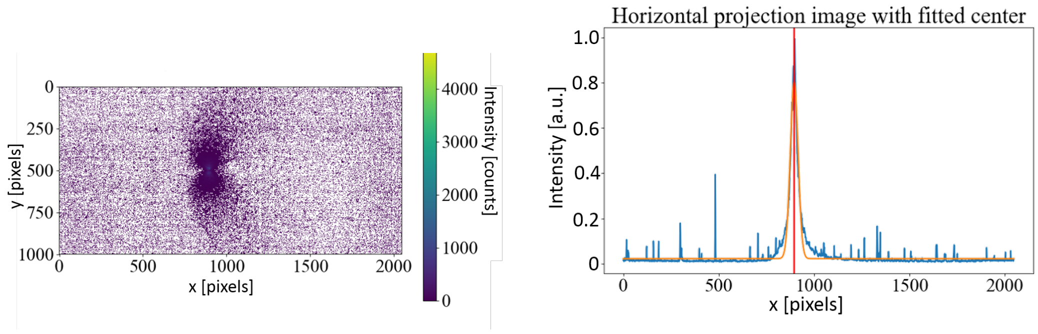

(a) (b)

Figure 4.4: Angular calibration: (a) 2D image of the TR angular pattern recorded with the 400 nm filter; (b) the blue curve is the horizontal projection of image (a) with a fit (orange curve) to find maximum, the red vertical line indicates the pixel of the orange curve maximum value.

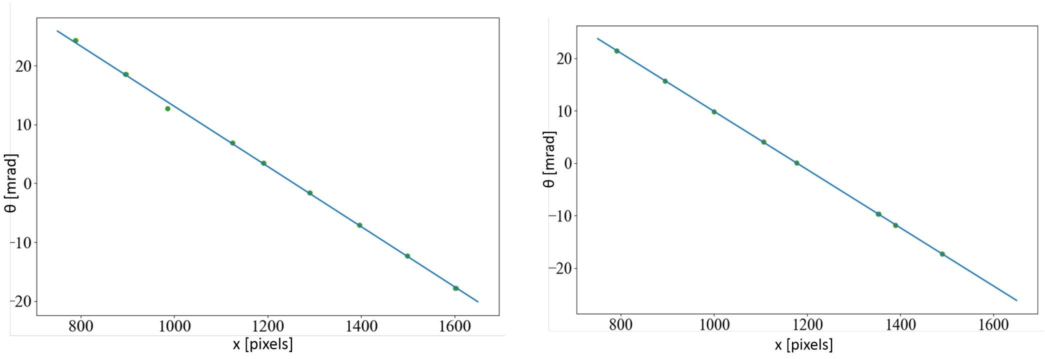

(a) (b)

Figure 4.5: Angular calibration curves for two different wavelengths: the target rotation θ versus the horizontal centre position x of TR (see Fig. 4.4) in pixel; (a) 400 nm filter; (b) 250 nm filter. Measured points are represented by dots and linear fitting curve by the blue line.

4.2 Synchrotron radiation suppression

Synchrotron Radiation is the electromagnetic radiation emitted when charged particles are radially accelerated. The SR acts as an undesired background in DR measurements because the SR intensity can be similar to or higher than DR [116]. In particular the SR produced upstream and reflected from the beam pipe arrives collinear with the beam, so in the angular distribution created in the back-focal plane of the lens it is concentrated in the centre of the DR pattern increasing the value of the minimum (see section 2.2.2) causing an overestimation of the beam size.

In particle accelerators SR is generated not only in dipole magnets but also in quadrupole magnets where an off-centre beam experiences a dipole deflection. This deflection is routinely used in accelerators for beam based alignment techniques [117], to align quadrupoles with respect to the beam orbit centre.

For these reasons the SR experimental conditions have been studied at ATF2 since they are related to many parameters, mainly the orbit, the current of the magnets (so the strength of the radial acceleration) and the effect of the mask. This study, summarised in the next sections, led to an operational procedure to minimize the SR contribution before any DR measurements.

4.2.1 Beam orbit

The first step of the SR suppression procedure consists of optimizing the beam orbit using all the steering (corrector) magnets present along the beam line before the DR/TR experimental station to reduce the bending radius locally and the off-centre position of the beam with respect to every quadrupole. The aim is to obtain a “flat” orbit monitoring the ATF2 Beam Position Monitors (BPMs), meaning an orbit that is in every point as close as possible to centre of the beam pipe. Fig. 4.6 shows the orbit in the vertical and horizontal planes recorded with ATF2 BPMs after the optimization process. It is seen that the absolute position of the beam is always below 600 μm with respect to the field center of the BPMs.

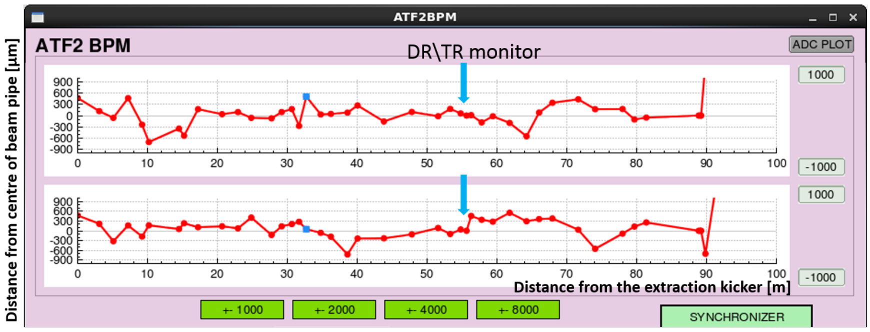

Figure 4.6: Beam orbit from ATF2 BPMs: upper plot is the vertical plane, lower is the horizontal plane. The horizontal scale is in metres from the extraction kicker, the position of the DR monitor is indicated by blue arrows. The vertical scale is in micrometres from the center of the beam pipe.

During the operation of the beam orbit optimization an important step is alignment of the quadrupoles QM14FF and QM15FF that are the closest optical elements present before the experimental station. This is necessary not only to reduce the SR background but also to have a stable position of the beam in the target slit varying the quadrupole current. In fact varying the QM14FF current changes the focusing strength of the magnet itself producing a variation of the vertical beam size at the DR monitor. Therefore to align the beam to the quadrupole centre the beam based alignment is performed, observing the deflection of the beam on the target, inserted to produce TR, through the imaging line.

The SR reduction obtained with this technique is clearly shown in Fig. 4.7, where the PVPC of the TR angular distribution is measured before and after the orbit optimization. The TR angular pattern has a well known two lobe structure with a deep minimum in the centre (see Fig. 2.3 in section 2.1.1). In our set-up, the minimum level is increased by the SR concentrated in the centre of the pattern by the lens; this contribution is reduced by the orbit optimization [81].

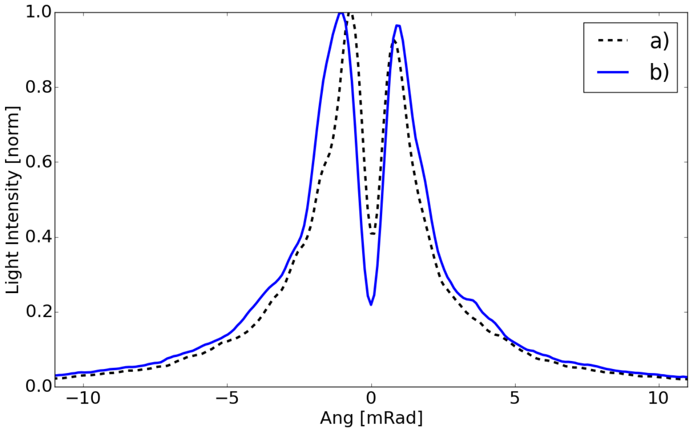

Figure 4.7: PVPC of TR angular distribution before (a) and after (b) orbit optimization. The value of the minimum in centre of the TR angular distribution is ≈ 20% lower after the orbit optimization.

4.2.2 Mask

Another important contribution to the reduction of the SR is the mask present in the experimental station. Indeed the use of the mask removes part of the SR generated upstream in the beam line. As for the orbit optimization effect, the presence of the mask was studied thanks to the well-known TR far-field distribution. Figure 4.8 compares two 2D images of the vertical polarization of the far-field distribution of TR recorded by the angular optical line. The presence of a spot in the middle of the pattern (focused SR) is clearly visible without the mask (Fig. 4.8(a)), which is removed when the mask (in this case the mask slit used was $399\mu m$) is inserted (Fig. 4.8(b)) [81].

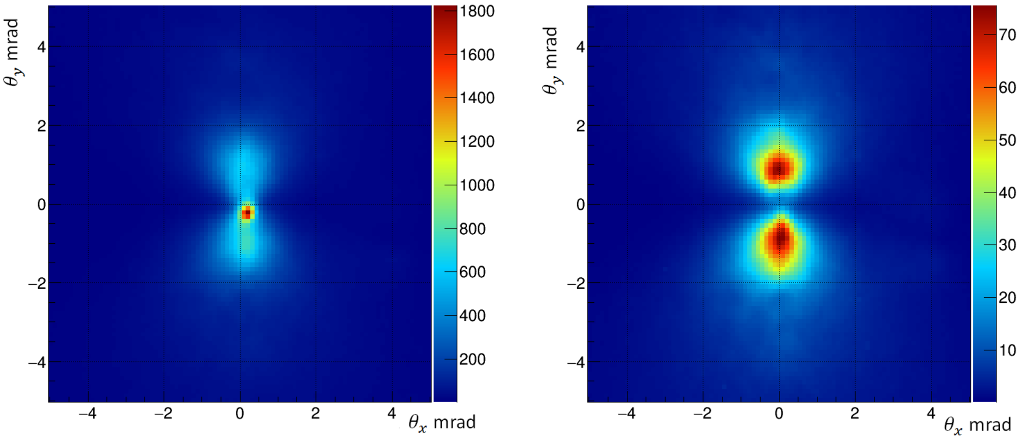

(a) (b)

Figure 4.8: TR angular pattern without (a) and with mask (b). In (a) the SR spot is present in the middle of the two lobe structure characteristic of TR vertical polarization.

4.3 DR beam position monitoring at ATF2

A precise knowledge of the position of the beam on the DR target is fundamental to perform beam size measurements. Indeed as it was introduced in Chapter 2, the DR angular pattern depends on the position of the centroid inside the slit (see Eq. 2.20 in section 2.2.3). For this reason the experimental station was designed to allow a synchronous acquisition of the target image and the far-field distribution as presented in Chapter 3. Figure 4.9(a) shows a single shot image of the $49.7\mu m$ slit recorded with the CCD intensified camera. The vertical profile (integrated between the two red lines) of this image is presented in Fig. 4.9(b).

The asymmetry between the two peaks of the DR profile can be defined as follows:

$$Asym = \frac{A_{top} - A_{bottom}}{A_{top} + A_{bottom}} \tag{4.1}$$

where A_{top} and A_{bottom} are respectively the amplitude of higher and lower peak [103], for instance the right peak and the left in Figure 4.9(b). It is easy to understand that this

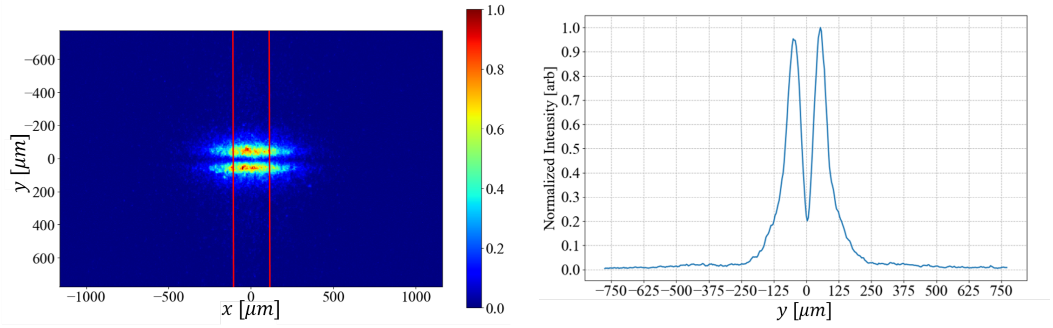

(a) (b)

Figure 4.9: Single shot DR image of the $49.7\mu m$ slit obtained with the imaging line: (a) 2D image, (b) vertical profile integrated between the red line of the image (a).

parameter gives information about the position of the beam inside the slit. In fact if the beam is closer to one side of the slit, the electrical field experienced by this side will be higher compared to the side more distant from the beam. Therefore more intense DR will be emitted at the closer side of the slit of the beam.

The response of the DR image profile asymmetry was measured scanning the beam inside the slit by means of steering magnets. The relative position of the beam into the target aperture was extracted from steering magnet currents and compared with the DR asymmetry ratio. Steering magnet current was calibrated with the TR image measuring the shift of the beam centroid versus steering current at the beginning of the shift giving a result of $11.5\mu m/A$. The zero crossing is found when the two DR lobes have the exact same amplitude. The beam position dependence presented in Fig. 4.10 was recorded scanning the beam into the $49.7\,\mu m$ target slit, and using the $600\,nm$ band-pass filter (bandwidth $40\,nm$).

According to the measurement, the asymmetry to position response is quite linear. The sensitivity is about 4% asymmetry variation per micron. The data are overlapped with the linear response simulated calculating the DR electrical field on the two side of the slit using the relation described in [65] already presented in section 2.1.4. The slight deviation from the linear response of the data is due to the hysteresis of the steering magnet since the expected beam position was extracted from the magnet current.

The presented measurements show how imaging DR source can be used as an optical beam position monitor. This allow to center precisely the beam inside the slit during angular data acquisition. Furthermore the possibility to continuously monitor the position

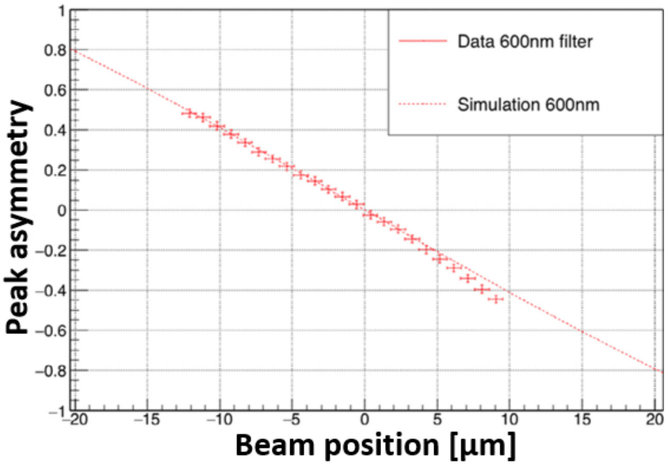

Figure 4.10: Beam position in μm versus asymmetry of DR peaks imaging the $49.7\mu m$ target slit showing a good agreement between simulation and measurements [103].

allow to correct the beam size data in case of drift during temporally long data acquisition shifts.

4.4 Beam size measurement at ATF2

During a data acquisition shift it is possible to record DRI far-field images after the optimization procedure. A cross calibration with TR PSF (see sec. 2.1.3) measurements is performed to check the sensitivity of DRI to small beam sizes (micrometres). The TR data are recorded with the same beam optics just before any DRI measurements to have reference beam size. This cross-calibration is described in the following section.

4.4.1 Calibration with transition radiation PSF

The target is inserted so that the beam intercepts the aluminum mirror to the side of the slit. TR radiation is therefore emitted and observed by the same optical system used for the DRI measurements. For example, Fig. 4.11 shows an image of TR vertical polarization (thanks to the polariser, see section 3.4) recorded when the beam is strongly focused vertically by magnet QM14FF. In this image it is clearly visible that there is the two-lobes structure of TR PSF introduced in section 2.1.3.

A procedure similar to that described in [23] and [22] is applied to extract the beam size and described in this section. In particular, an automated quadrupole scan (thanks

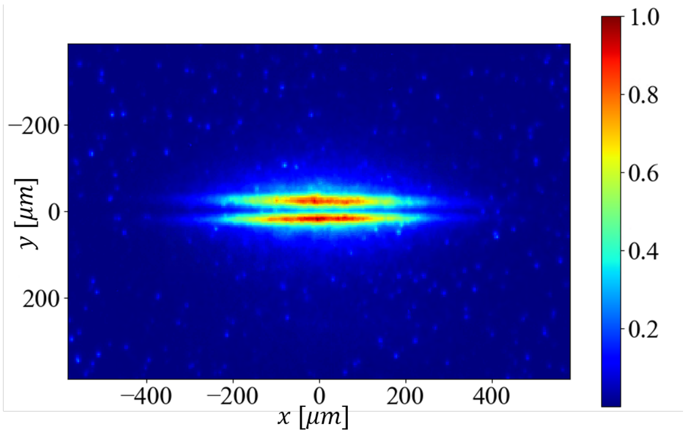

Figure 4.11: Image of TR 2D PSF recorded during the experimental study for a measured vertical beam size of 1.5 μm.

to the developed control system described in section 3.5) is performed with QM14FF: the current is varied over a large quadrupole current range (from -90 Amps to -50 Amps) and for each step of current an image of TR is recorded. Then the TR PSF PVPC with minimum visibility is selected, defined as the ratio between the minimum between the peaks and the maximum I_{min}/I_{max} (see section 2.1.3). Since the intensity of the peaks is not equal, the maximum is calculated as the average values between the two peaks. This difference between the two peaks (less then 5%) can be explained by an optical misalignment of the order of few microns. The TR profile of minimum visibility is the closest to the expected form of an ideal zero-size particle beam. Then this profile is convoluted with different rms Gaussian profiles that represent real beam sizes, as depicted in Fig. 4.12(a).

It is possible, in this way, to obtain a calibration curve of the visibility, measured on these convoluted profiles, against the added beam size, as shown in Fig. 4.12(b). In particular, blue points are calculated with the convolution of different width Gaussian distributions, representing the beam, with single particle TR PSF; the orange curve is obtained with a third order polynomial fit of the blue points. It is seen that the curve saturates (reaching a plateau for a visibility 0.4) for small beam sizes of around 1 μm, showing the limit of the optical system in measuring very small beams. This limit come from the fact that the system was designed to find the position of the beam with respect to the smallest DR of slit of 49.7 μm. Nevertheless such resolution of 1 μm was sufficient for our purpose. The third order polynomial used in Fig. 4.12(b) to fit the curve, $V = A\sigma_y^3 + B\sigma_y^2 + C\sigma_y^2 + D$ where V is the visibility, A,B,C,D the fit parameters and σ_y the

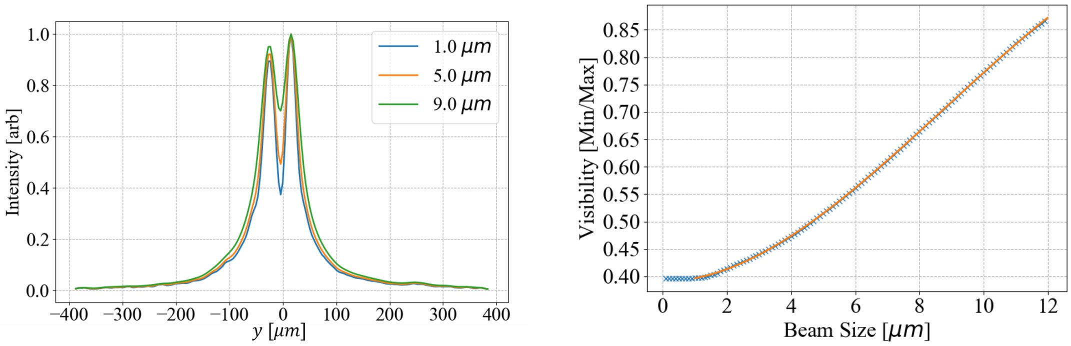

(a) (b)

Figure 4.12: TR calibration. In (a) PSF PVPC convolution with different Gaussian beam sizes: $1\,\mu m$ blue curve, $5\,\mu m$ orange curve, $9\,\mu m$ green curve. In (b) the curve obtained for the vertical beam size versus PSF PVPC visibility. Blue points are calculated with the convolution of different width Gaussian distributions, representing the beam, with single particle TR PSF, the orange curve is obtained with third order polynomial fit of blue points.

vertical beam size, provide a relation between visibility and beam size.

The relation found between visibility and beam size allows us to associate a beam size to the measured visibility of the TR PSF during the quadrupole scan. Fig. 4.13(a) shows the single shot visibility versus the QM14FF current measured from the TR PSF PVPC: the error bars are the error on the mean of the visibility distribution over 100 images. The centre value is the mean value of the distribution. As can be seen the errors are bigger closer to visibility value of 1. In fact the visibility is 1 when the maximum has the same value as the minimum meaning that there is not a two-lobe structure anymore. So in the cases close to 1 it is practically very difficult to define the peaks and this increases the error due to the peak fitting procedure.

Finally, starting form the TR data acquired, it is possible to plot the beam size against the quadrupole current (Fig. 4.13(b)) thanks to the relation found between the visibility values and the beam size. This allows us to know the beam size for a given QM14FF current, so that when the DR angular profile is recorded under the exact same conditions, it can be compared to the expected beam size.

The consistency of the TR PSF cross calibration data was verified comparing the vertical beam size at the location of the experimental station with SAD [118] simulation. The beam optics during data acquisition was saved and used as input for SAD simulation. The results of this comparison is presented in Fig. 4.14, it is seen that TR PSF are in

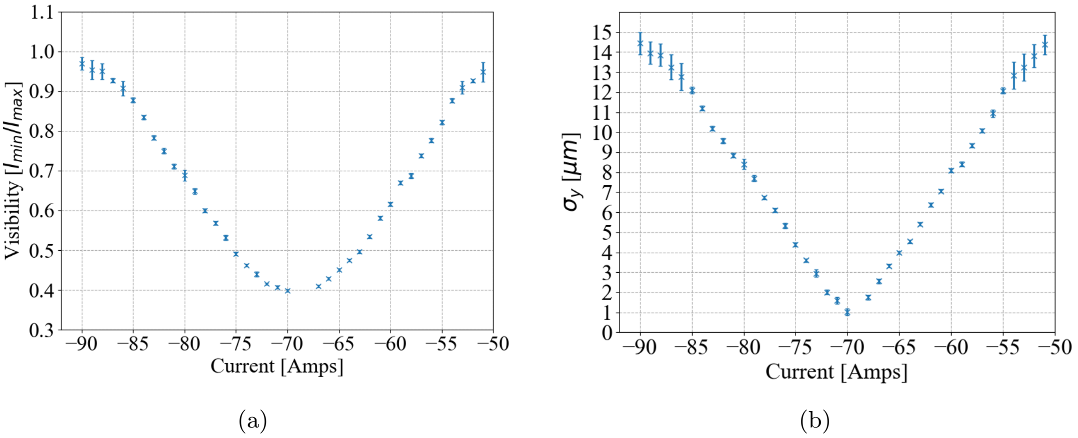

Figure 4.13: TR PSF quadrupole scan (a) showing the variation of visibility as function of QM14FF current. In (b) the vertical beam size versus magnet current.

good agreement with the simulated beam size.

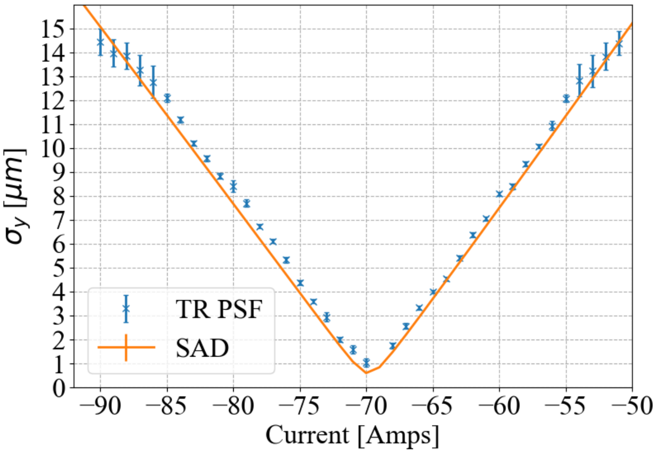

Figure 4.14: TR vs SAD comparison, showing a very good agreement for the performed quadrupole scan.

The vertical beam emittance used for the simulation is 34 pm. The emittance is also measured with the TR PSF through a parabolic fit of the beam size squared versus the magnet current, depicted in Fig. 4.15 using the well known method described in the literature [119, 120]. A second order polynomial fit $x^2 = a(1/f)^2 - 2ab(1/f) + (c + ab^2)$ is used where x^2 is the beam size squared, $1/f$ is the inverse of the focal-length or the quadrupole strength (kLq) and a, b, c fit parameters. The measured emittance is therefore calculated as $\sqrt{ac}/d^2$ where d is the distance between the TR screen and the quadrupole. From this fit a value of 33 $\pm$ 3 pm is obtained for the emittance that is in very good agreement with the simulated beam emittance.

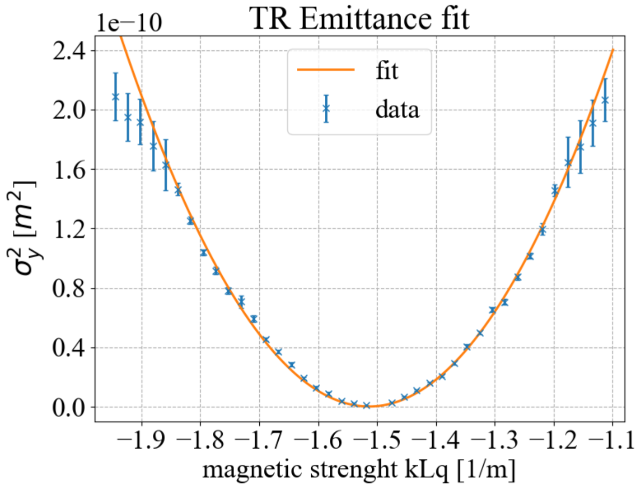

Figure 4.15: TR emittance parabolic fit: on the vertical axis the beam size squared, on the horizontal axis the magnetic strength of the quadrupole QM14FF.

4.4.2 DRI measurements

The first set of measurements collected during operation was in the visible range, specifically at 400 nm. This wavelength was chosen because despite being in the visible spectrum it is shorter compared to 600 nm. Therefore it is expected to provide a better sensitivity to small beam size as explained in section 2.2.4. Furthermore thanks to the wide commercial availability of optical components for visible light it was possible to use a very narrow-band filter that helps to reduce the background.

In Fig. 4.16(a), an image of DRI vertical polarization angular pattern measured with a 400 nm filter is shown. The PVPC image of this 2D image is presented in Fig. 4.16(b), showing a typical DRI angular pattern as presented in 2.2.4. In the case depicted in this image, the beam was strongly focused in the vertical direction by QM14FF leading to a very small visibility, thanks also to the small SR contribution that would otherwise have increased the minimum value.

Thanks to the careful choice of every component of the optical line (see section 3.4), in particular the intensifier of the angular line with a good sensitivity to wavelengths down to 200 nm, it was also possible to acquire data in the UV at 250 nm. In Fig. 4.17(a) an image of vertical polarization DRI angular pattern saved in the far-UV, is acquired with

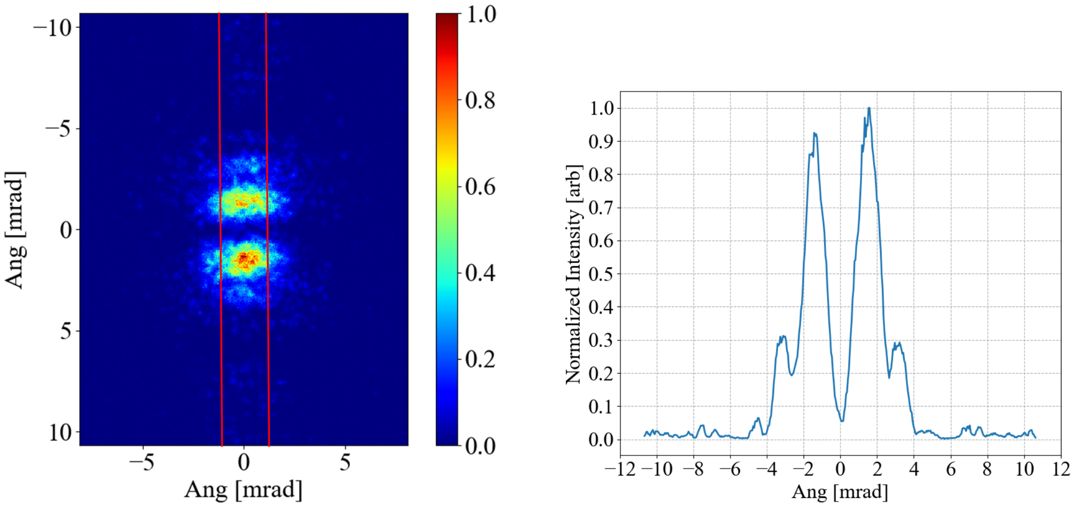

(a) (b)

Figure 4.16: Single shot 2D DRI angular pattern (a). PVPC (b) calculated between the two red lines in (a). DR is produced from target slit 49.7 μm and mask 100 μm at 400 nm with QM14FF current −70 Amps ($\sigma_y = 3 \mu m$).

the same beam conditions as in Fig. 4.16(a), showing a slightly smaller DR pattern with respect to the visible wavelength. The contraction of the DR pattern with respect to the visible light leads to an increased sensitivity to smaller beam sizes as already discussed in section 2.2.4. In this case the PVPC, illustrated in Figure 4.17(b), presents a larger value of the minimum in between the two peaks meaning a better sensitivity to this beam size.

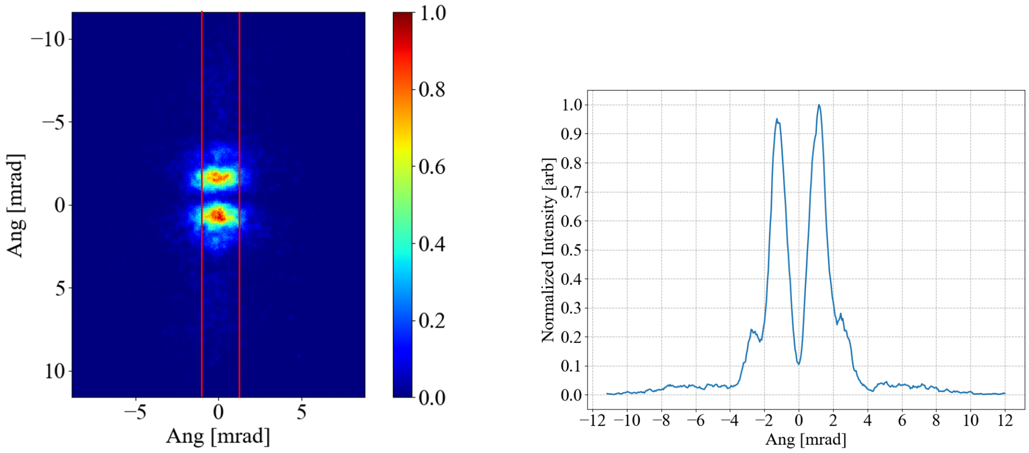

(a) (b)

Figure 4.17: Single shot 2D DRI angular pattern (a). PVPC (b) calculated between the two red lines in (a). DR is produced from target slit 49.7 μm and mask 100 μm at 250 nm with QM14FF current −70 Amps ($\sigma_y = 3 \mu m$).

During the data taking, as in the case of the TR measurements, automated quadrupole scans were performed to record the DRI patterns for different vertical beam sizes. The results of these scans are presented in Figure 4.18. The visibility of the PVPC is plotted against the magnetic current, i.e. the magnetic strength, of QM14FF. In particular the distribution of the single shot measured visibility. From the comparison of Fig. 4.18(a) and Fig. 4.18(b), the reader can notice that the sensitivity to the change of vertical beam size is much higher in the UV observation.

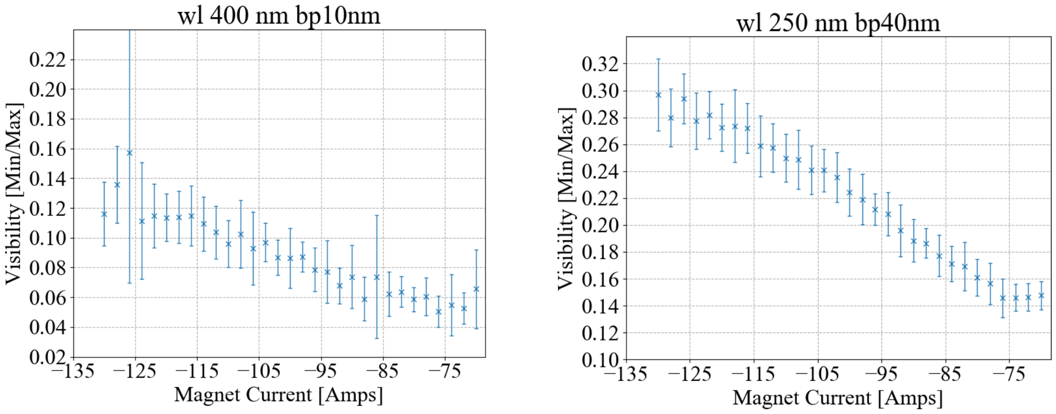

(a) (b)

Figure 4.18: DR quadrupole scan at $400nm$ (a) and at $250nm$ (b). The error bar are here the rms of distribution of 20 images (a) and 25 images (b) for each magnet current point.

Considering the cross-calibration obtained with TR PSF explained in the previous section 4.4, the current of the magnet can be converted to the expected beam size allowing a plot of the visibility as a function of the beam size to be made. This graph is shown for both wavelengths in Fig. 4.19. It is seen that the UV DR have a better sensitivity to beam size. A linear fit is plotted over the two set of data to show the sensitivity for different wavelengths. It has to be remarked that on one hand the 400 nm data show how ODR measurement has an intrinsic limit around 5 μm, below this value the visibility reach a plateau of ≈ 0.050 meaning that even if the beam is smaller (as it is known from the TR measurements) it can not be measured with the DR technique. On the other hand the UV observations at 250 nm show how this limit is pushed down to about 3 μm where the visibility is ≈ 0.125.

As during the QM14FF scan we are varying the vertical beam size at the screen location passing through a beam waist, from the data acquired it is possible to extract the vertical beam emittance. Specifically the technique previously described in section 4.4.1

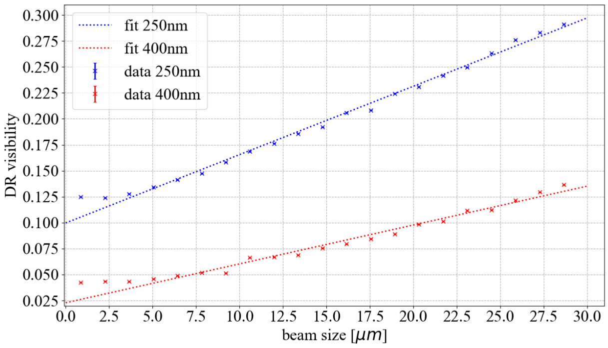

Figure 4.19: DR beam size sensitivity at 400 nm and 250 nm. Error bar on the data point represent the error on the mean. The smallest beam size from which we visibility starts to increase for an increasing beam size is 5 μm for 400 nm and 3 μm for 250 nm.

based on a parabolic fit is applied. The data and the fit are presented in Fig. 4.20 for visibile (400 nm) and UV (250 nm). The measured emittance is 33 ± 13 pm and 32 ± 5 pm respectively for 400 nm and 250 nm providing a very good agreement with the emittance measured with TR PSF and simulated with SAD. The fact that the visible data lead to a larger error on the emittance (i.e. a worse fit shape) compared to the UV measurements, is due to the saturation effect at small beam sizes as can be seen in Fig. 4.19.

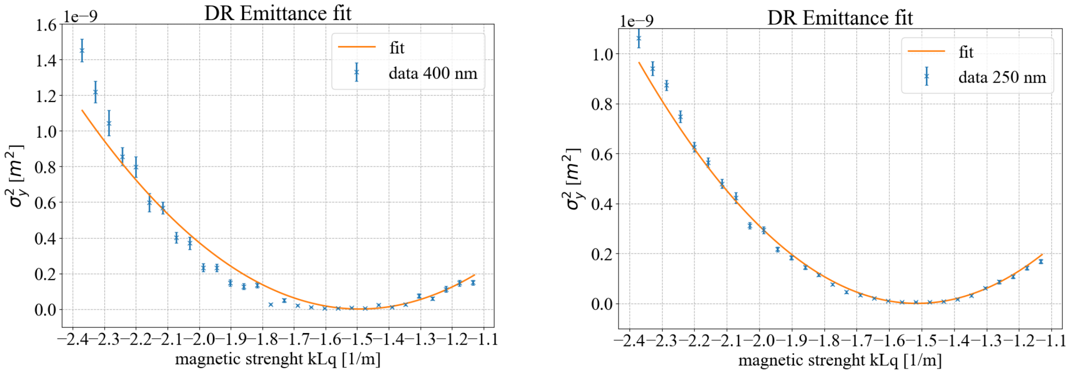

(a) (b)

Figure 4.20: Beam size squared versus magnetic strength for DR quadrupole scan at 400 nm (a) and at 250 nm. Data with statistical error bar (error of the mean) over 20 images (a) and 25 images (b) and the parabolic fits are shown. In (a) the saturation effect for small beam sizes is evident: the minimum of the parabola is flat.

Chapter 5

Conclusion

5.1 Main results and achievements

The main aim of this thesis was to develop a combined transition and diffraction radiation station for non-invasive beam size monitoring for linear accelerators, specifically for the future generation of linear colliders. The interest in this kind of technology for linear collider applications has been discussed in the introductory chapter 1. Therefore, during this thesis work a TR/DR combined monitor has been designed, installed and tested on ATF2 beam line at KEK. This accelerator is, indeed, a test facility for future linear colliders, in particular for the ILC final focus, providing a small emittance beam that can be focused to sub-micrometre beam sizes challenging present technologies in terms of transverse beam size measurements.

A comprehensive and detailed overview of TR and DR is presented in chapter 2, where the theoretical aspect of these polarization radiations are described with the specific perspective of beam diagnostics. Furthermore, to understand the effect of the presence of a mask to block the contamination by Synchrotron Radiation background an innovative experimental study on the shadowing phenomenon is presented in the same chapter. This study, experimentally conducted at CALIFES at CERN during my PhD, shows how the interference between the target generated radiation and the upstream mask one has to be taken into account for a mask installed within the radiation formation length.

The work carried out during the thesis period was divided in two main parts. The first was the design and the installation of the TR/DR monitor. The experimental apparatus have been carefully designed, following the experience matured in our research team on previous DR and TR experiments. For instance, as presented in Chapter 3 the target was designed with a limited mirrored area to minimize the SR reflection and the target slits size was chosen to maximize the DR emission and to produce sensitivity to small beam size. Furthermore, the innovative design of the optical line allows synchronously direct high resolution (less then $1\,\mu m$) images of the target surface and angular distribution distribution of DR or TR in visible or UV wavelength range to be acquired.

The second part of the thesis work was focused on the commissioning of the experimental apparatus and on the data acquisition and processing. As presented in details in Chapter 4, the study show that the instrument is capable to measure micrometre scale transverse beam size thanks to the TR PSF technique. Furthermore, as predicted by the theory, the sensitivity to beam size for DR measurements increased with UV wavelengths ($250\,nm$). The system was proven to detect a beam size as small as $5\,\mu m$ much smaller then the previous lower limit of this technique of $14\,\mu m$ present in literature [40]. Vertical emittances of $32 \pm 5\,pm$ and $33 \pm 13\,pm$ were also measured with quadrupole scans.

In conclusion this study proved that non-invasive DR measurements performed in the UV region can measure micron scale beams. Furthermore, combining this system with a very high-resolution TR monitor, it is possible to have an instrument that not only can measure low intensity and very small beams, e.g. pilot beams of linear collider with a limited number of bunches or short pulse train lengths, but also can monitor the beam size during standard operation at full charge. In addition, the instrument can measure the beam size (with micron precision) at the monitor location thanks to synchronous acquisition of imaging and angular distributions.

5.2 Future studies

As presented in [121–123], another non-invasive technique based on polarization radiation is the Cherenkov diffraction radiation (CDR). This is the radiation emitted through the Cherenkov effect by particles travelling at a distance h from the surface of a dielectric, also called the impact parameter. In particular, the use of Incoherent Cherenkov radiation for beam instrumentation purposes is really interesting for the expected high total number of photons emitted and its highly directional emission [123]. This can allow discrimination of CDR signal from the SR background, contrary to DR where SR is the limiting background source. With a properly designed target, similar to that described in [122], and an adapted optical line, the TR/DR station can be modified to study CDR. In particular, as the location at ATF2 allows exploitation of sub-micrometer beam sizes that are difficult to find in other accelerators, the lower limit of the CDR resolution can be investigated.

Appendix A

OTRI at CALIFES

The OTRI experiment, indrodued in Chapter 2 was conducted in the CALIFES beam line insdie the CLEX complex of the CLIC Test Facility 3 (CTF3) at CERN. Here the electrons are accelerated up to an energy of 205 MeV, with a corresponding formation length in the optical region of $L_f(\lambda = 500\,nm) \approx 13\,mm$ from Eq. 2.3.

Fig. A.1 presents the CALIFES beam line. The beam is produced in a Cs_2Te photo-injector pulsed by an UV ($262nm$) laser which delivers up to $270\,nJ$/pulse. This energy can be reduced using a hard aperture to produce a bunch charge up to $0.6\,nC$ with a bunch frequency of $1.5\,GHz$ [124]. The accelerator can run with trains ranging from 1 to 300 bunches. The acceleration is provided by a single klystron delivering pulses of 45 MW to power the gun, a buncher structure and two accelerating structures [125]. Using a compression cavity the pulse peak power is increased to $130\,MW$ during $1.2\,\mu s$, the necessary time to fill the accelerating structures. An attenuator and a phase shifter located before the gun provide flexibility tuning bunch extraction from the photo-cathode [125]. The phase of the buncher can be independently controlled using a specially developed power phase shifter thereby operating the structure close to the zero crossing, thus shortening the bunch length via velocity bunching. The whole acceleration system of the injector can provide a beam with kinetic energy up to $210\,MeV$ with an energy spread $< 2\%$. The energy spread can be increased by changing the timing of the laser pulse versus the RF pulse to produce a train of pulses scaled in energy if needed. A system of solenoids around the accelerating cavities keep the beam emittance below $10\pi \cdot mm \cdot mrad$; this can be measured by quadrupole scan using a quadrupole triplet and a screen downstream the last accelerating cavity. Finally a spectrometer line located downstream the injector enables energy measurements [125].

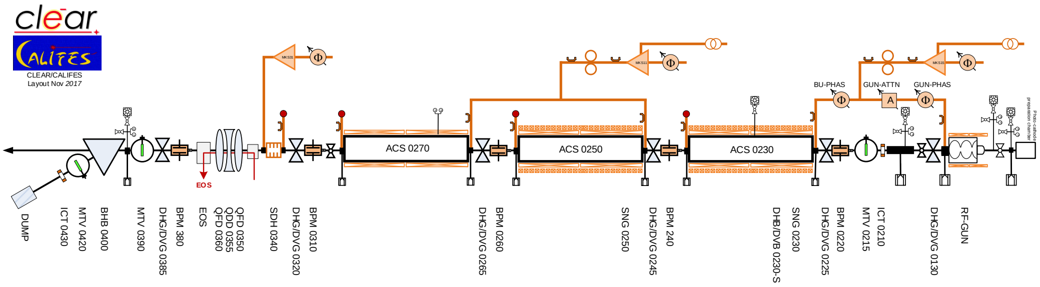

Figure A.1: CALIFES beam line [126].

The OTRI experiment was installed after the spectrometer line, a focusing triplet (QFD0510,QDD0515,QFD0520), a BPM (BPM530) and a gate-valve (DHJ/DVJ0540), in the beam line now called CLEAR, as can been seen in Fig. A.2. Here the right end part of the line is the outcoming beam line of CALIFES depicted in left part of Fig. A.1.

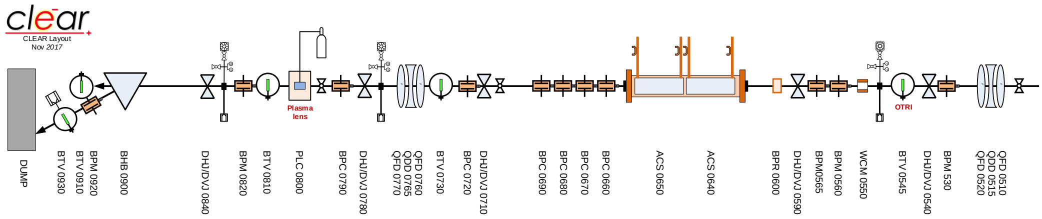

Figure A.2: CLEAR beam line [126].

A schematic drawing of the setup is shown in Fig. A.3. A 100 μm thick aluminum foil (a) and a 200 μm thick aluminum-coated silicon screen (b) are mounted on a linear actuator that moves the screen assembly across the beam path. The assembly is designed to have an angle of 90° between the screens so that the distance traveled by the particle beam between the two screens d can be changed depending on the position of the screen assembly within a range $0 < d < 34\,mm$. Screen (b) is longer than (a) by $9\,mm$, allowing the particle beam to solely cross screen (b), therefore producing backward single-screen OTR as a reference [18]. Because of the 45° orientation of both screens with respect to the electron beam, the TR signal is emitted orthogonally from the beam path through a borosilicate glass view-port (not shown in Fig. A.3). The whole optical setup is mounted on a motorized translation stage allowing the control of its transverse position with respect to the target assembly. Indeed, when the screen assembly is moved across the beam, the area where screen (b) intercepts the beam (that is the OTR source) moves along the beam path. Given the narrow (of the order of $1/\gamma = 2.5\,mrad$) angular distribution of OTR light, to avoid any optical distortion the typical conical light emission of OTR must coincide with the optical axis of the instrument. Therefore, a transverse scan of the optical imaging system until the light intensity reaching the sensor is maximized is needed whenever the distance between screens is changed [18]. Figure A.3 shows the setup for angular measurements. A 12 bit, 1/3 of inch CCD sensor (f) is placed in the backfocal plane of a $f = 40\,mm$, $1''$ diameter air-spaced doublet (e) to reproduce far-field,i.e. angular distribution of the incoming radiation, after passing through a set of band pass filters (400 or $650\,nm$; bandwidth $40\,nm$) (d). The focus is adjusted prior to the experiment, by sending a laser centered inside the beam pipe following the electron beam path. The system is designed to record an angular range $-42 < \theta < 42\,mrad$, with a resolution of $\approx 94\,\mu rad/pixel$. A pellicle beam-splitter (c) sends approximately 3% of the light, through a lens to create an image, to a camera for monitoring purposes (h) [18].

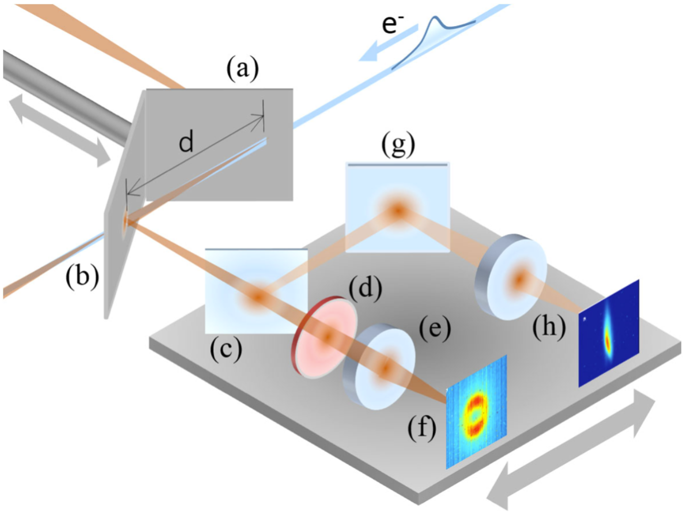

Figure A.3: OTRI setup at CALIFES [18].

Appendix B

Target and Mask slits

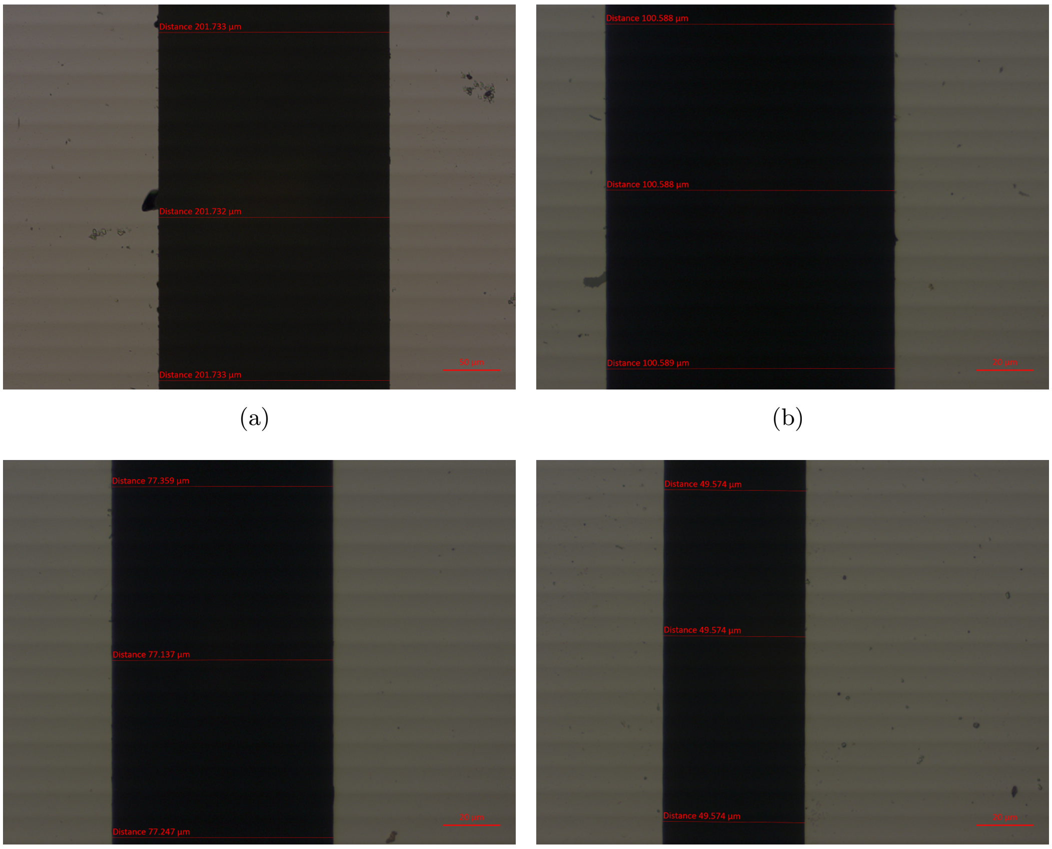

(a) (b)

(c) (d)

Figure B.1: Measurement of DR target slits size with microscope: (a) 201.7 μm slit ; (b) 100.6 μm slit; (c) 77.2 μm slit; and, (d) 49.57 μm slit.

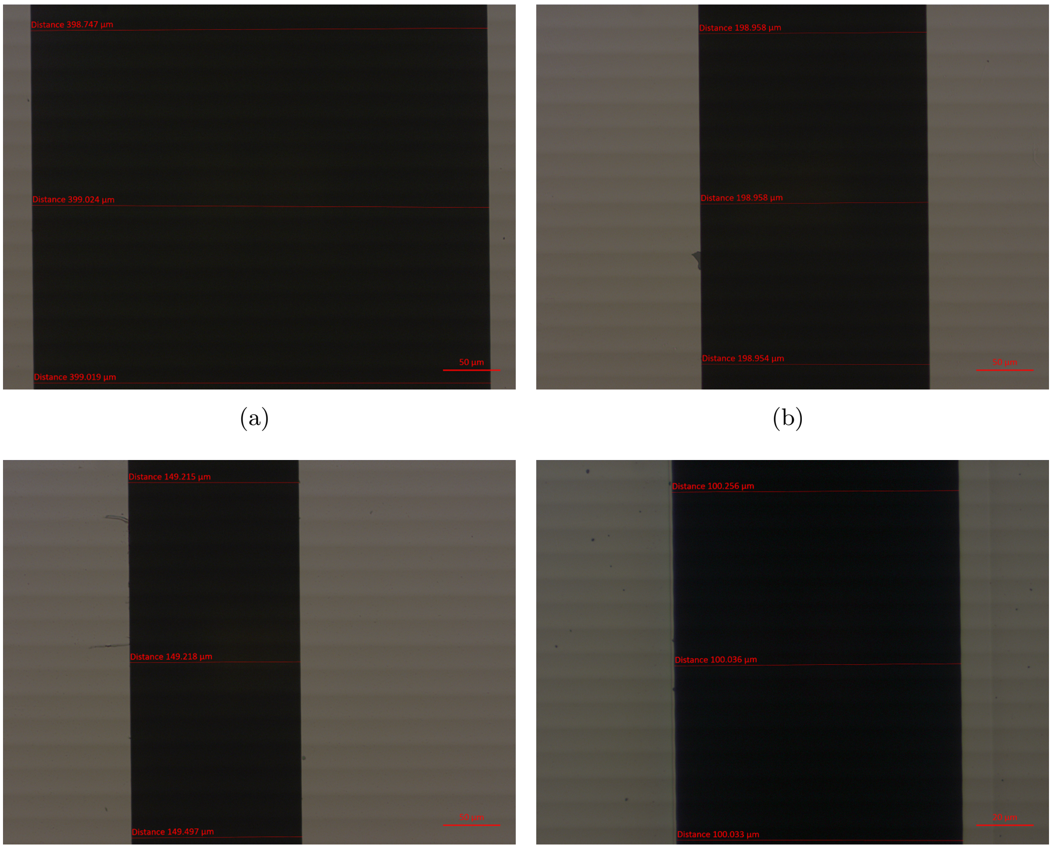

(a) (b)

(c) (d)

Figure B.2: Measurement of SR mask slits size with microscope: (a) 399 μm slit ; (b) 198.9 μm slit; (c) 149.2 μm slit; and, (d) 100 μm slit.

Abbreviations

ATF2 Accelerator Test Facility 2

BDR Backward Diffraction Radiation

BPM Beam Position Monitor

BTR Backward Transition Radiation

CCD Charge-Coupled Device

CLIC Compact Linear Collider

CMOS Complementary Metal-Oxide Semiconductor

CTF3 Clic Test Facility 3

DB Drive Beam of CLIC

DR Diffraction Radiation

DRI Diffraction Radiation Interference

FDR Forward Diffraction Radiation

FTR Forward Transition Radiation

FWHM Full Width Half Maximum

ILC International Linear Collider

IP Interaction Point

LHC Large Hadron Collider

MB Main Beam of CLIC

MDI Machine Detector Interface

OTR Optical Transition Radiation

OTRI Optical Transition Radiation Interference

PSF Point Spread Function

PVPC Projected Vertical Polarization Component

RF Radio Frequency

RTML Ring To Main Linac of CLIC

sCMOS scientific Complementary Metal-Oxide Semiconductor

SR Synchrotron Radiation Interference

TR Transition Radiation

UV Ultraviolet

YAG Yttrium-Aluminum-Garnet

Bibliography

[1] O. Brüning, H. Burkhardt, and S. Myers, *The large hadron collider*, Progress in Particle and Nuclear Physics **67**, 705 (2012).

[2] G. Aad *et al.*, *Observation of a new particle in the search for the Standard Model Higgs boson with the ATLAS detector at the LHC*, Physics Letters B **716**, 1 (2012).

[3] M. Aicheler *et al.*, *A Multi-TeV linear collider based on CLIC technology: CLIC Conceptual Design Report*, CERN Report No. CERN-2012-007, 2012.

[4] M. Boland *et al.*, *Updated baseline for a staged Compact Linear Collider*, CERN Report No. CERN-2016-004, 2016.

[5] P. Burrows *et al.*, *CLIC Project implementation Plan*, CERN Report No. CERN-2018-010-M, 2018.

[6] F. Zimmermann, *Accelerator Physics and Technologies for Linear Collider, Lecture Note on the Beam delivery System* (University of Chicago, Chicago, Illinois, 2002).

[7] J. Delahaye, G. Guignard, T. Raubenheimer, and I. Wilson, *Scaling laws for e+/e- linear colliders*, Nuclear Instruments and Methods in Physics Research Section A: Accelerators, Spectrometers, Detectors and Associated Equipment **421**, 369 (1999).

[8] E. Bravin, T. Lefevre, and C. Vermare, *OTR studies for the high charge CTF3 beam*, in *Particle Accelerator Conference, 2003. PAC 2003. Proceedings of the* Vol. 4, pp. 2464–2466, IEEE, 2003.

[9] C. Bambade *et al.*, *4D Emittance Measurements Using Multiple Wire and Waist Scan Methods in the ATF Extraction Line.*, in *Proc. Particle Accelerator Conference (EPAC08)*, pp. 1257–1259, 2008.

[10] C. Limborg, S. Gierman, and J. Power, *A modified quadscan technique for emittance measurement of space charge dominated beams*, in *Proc. of the Particle Accelerator Conference 2003* Vol. 4, pp. 2667–2669, IEEE, 2003.

[11] H. H. Braun *et al.*, *Nulling emittance measurement technique for CLIC Test Facility*, in *Proc. of the 1997 Particle Accelerator Conference* Vol. 1, pp. 479–481, IEEE, 1997.

[12] G. Baud *et al.*, *Performance Assessment of Wire-Scanners at CERN*, CERN Report No. CERN-ACC-2013-0308, 2013.

[13] H. Hayano, *Wire Scanners for Small Emittance Beam Measurements in ATF*, in *Proc. Linac 2000*, p. 146, 2000.

[14] D. Rule, *Transition radiation diagnostics for intense charged particle beams*, Nuclear Instruments and Methods in Physics Research Section B: Beam Interactions with Materials and Atoms **24**, 901 (1987).

[15] W. Graves, E. Johnson, and S. Ulc, *A high resolution electron beam profile monitor and its applications*, in *AIP Conference Proceedings* Vol. 451, pp. 206–213, AIP, 1998.

[16] K. Wittenburg, *Specific instrumentation and diagnostics for high-intensity hadron beams*, arXiv preprint arXiv:1303.6767 (2013).

[17] M. Koujili *et al.*, *Fast and high accuracy wire scanner*, CERN Report No. CERN-BE-2009-021, 2009.

[18] R. Kieffer *et al.*, *Experimental Observation of Shadowing in Optical Transition Radiation*, Physical review letters **120**, 094802 (2018).

[19] K. Honkavaara *et al.*, *Design of OTR beam profile monitors for the TESLA Test Facility, phase 2 (TTF2)*, in *Particle Accelerator Conference, 2003. PAC 2003. Proceedings of the* Vol. 4, pp. 2476–2478, IEEE, 2003.

[20] M. Castellano and V. A. Verzilov, *Spatial resolution in optical transition radiation beam diagnostics*, Phys. Rev. ST Accel. Beams **1**, 062801 (1998).

[21] M. Ross *et al.*, *Very high resolution optical transition radiation beam profile monitor*, in *AIP Conference Proceedings* Vol. 648, pp. 237–247, AIP, 2002.

[22] A. Aryshev *et al.*, *A novel method for sub-micrometer transverse electron beam size measurements using optical transition radiation*, Journal of Physics: Conference Series **236**, 012008 (2010).

[23] K. Kruchinin *et al.*, *Sub-micrometer transverse beam size diagnostics using optical transition radiation*, Journal of Physics: Conference Series **517**, 012011 (2014).

[24] D. Xiang and W.-H. Huang, *Theoretical considerations on imaging of micron size electron beam with optical transition radiation*, Nuclear Instruments and Methods in Physics Research Section A: Accelerators, Spectrometers, Detectors and Associated Equipment **570**, 357 (2007).

[25] A. Hofmann, *The Physics of Synchrotron Radiation (Cambridge Monographs on Particle Physics, Nuclear Physics and Cosmology)* (Cambridge University Press, 2004).

[26] S. Takano, M. Masaki, and H. Ohkuma, *X-ray imaging of a small electron beam in a low-emittance synchrotron light source*, Nuclear Instruments and Methods in Physics Research Section A: Accelerators, Spectrometers, Detectors and Associated Equipment **556**, 357 (2006).

[27] M. Kocsis and A. Snigirev, *Imaging using synchrotron radiation*, Nuclear Instruments and Methods in Physics Research Section A: Accelerators, Spectrometers, Detectors and Associated Equipment **525**, 79 (2004).

[28] K. Iida *et al.*, *Measurement of an electron-beam size with a beam profile monitor using Fresnel zone plates*, Nuclear Instruments and Methods in Physics Research Section A: Accelerators, Spectrometers, Detectors and Associated Equipment **506**, 41 (2003).

[29] Å. Andersson, O. Chubar, M. Rohrer, A. Streun, and V. Schlott, *Electron Beam Profile Measurements with Visible and X-ray Synchrotron Radiation at the Swiss Light Source*, in *Proc. 10th European Particle Accelerator Conf., 26-30 June 2006, Edinburgh, Scotland, UK (2006)*, p. 12231225, 2006.

[30] M. Sjöström, H. Tarawneh, and E. Wallén, *Characterisation of the MAX-II Electron Beam: Beam Size Measurements*, in *Proc. 10th European Particle Accelerator Conf., 26-30 June 2006, Edinburgh, Scotland, UK (2006)* Vol. 60626, pp. 1193–1195, 2006.

[31] T. Mitsuhashi *et al.*, *Spatial coherency of the synchrotron radiation at the visible light region and its application for the electron beam profile measurement*, KEK preprint/National laboratory for high energy physics (Tsukuba) **97**, 56 (1997).

[32] T. Naito and T. Mitsuhashi, *Very small beam-size measurement by a reflective synchrotron radiation interferometer*, Physical Review Special Topics-Accelerators and Beams **9**, 122802 (2006).

[33] T. Mitsuhashi, *Measurement of small transverse beam size using interferometry*, in *Proc. of DIPAC* Vol. 1, 2001.

[34] I. Agapov, G. Blair, and M. Woodley, *Beam emittance measurement with laser wire scanners in the International Linear Collider beam delivery system*, Physical Review Special Topics-Accelerators and Beams **10**, 112801 (2007).

[35] P. Tenenbaum and T. Shintake, *Measurement of small electron-beam spots*, Annual Review of Nuclear and Particle Science **49**, 125 (1999).

[36] S. T. Boogert *et al.*, *Micron-scale laser-wire scanner for the KEK Accelerator Test Facility extraction line*, Physical Review Special Topics-Accelerators and Beams **13**, 122801 (2010).

[37] T. Shintake, *Proposal of a nanometer beam size monitor for e+ e- linear colliders*, Nuclear Instruments and Methods in Physics Research Section A: Accelerators, Spectrometers, Detectors and Associated Equipment **311**, 453 (1992).

[38] T. Suehara *et al.*, *A nanometer beam size monitor for ATF2*, Nuclear Instruments and Methods in Physics Research Section A: Accelerators, Spectrometers, Detectors and Associated Equipment **616**, 1 (2010).

[39] A. P. Potylitsyn, M. I. Ryazanov, M. N. Strikhanov, and A. A. Tishchenko, *Radiation from Relativistic Particles*, in *Diffraction Radiation from Relativistic Particles*, pp. 1–28, Springer, 2010.

[40] P. Karataev *et al.*, *Beam-size measurement with optical diffraction radiation at KEK accelerator test facility*, Physical Review Letters **93**, 244802 (2004).

[41] A. Lumpkin, W. Berg, N. Sereno, D. Rule, and C.-Y. Yao, *Near-field imaging of optical diffraction radiation generated by a 7-GeV electron beam*, Physical Review Special Topics-Accelerators and Beams **10**, 022802 (2007).

[42] E. Chiadroni *et al.*, *Non-intercepting electron beam transverse diagnostics with optical diffraction radiation at the DESY FLASH facility*, Nuclear Instruments and Methods in Physics Research Section B: Beam Interactions with Materials and Atoms **266**, 3789 (2008).

[43] P. Karataev, *Investigation of optical diffraction radiation for non-invasive low-emittance beam size diagnostics*, PhD thesis, PhD Thesis, Tokyo Metropolitan University, 2004.

[44] L. Bobb *et al.*, *Feasibility of diffraction radiation for noninvasive beam diagnostics as characterized in a storage ring*, Physical Review Accelerators and Beams **21**, 032801 (2018).

[45] Y. Shibata *et al.*, *Observation of coherent diffraction radiation from bunched electrons passing through a circular aperture in the millimeter-and submillimeter-wavelength regions*, Physical Review E **52**, 6787 (1995).

[46] Y. Shibata *et al.*, *Diagnostics of an electron beam of a linear accelerator using coherent transition radiation*, Physical Review E **50**, 1479 (1994).

[47] Y. Shibata *et al.*, *Observation of coherent transition radiation at millimeter and submillimeter wavelengths*, Physical Review A **45**, R8340 (1992).

[48] V. Ginzburg and I. Frank, *Radiation of uniformly moving electron at transition from one media into another one*, Sov. Phys. JETP **16**, 15 (1946).

[49] M. Castellano *et al.*, *Analysis of optical transition radiation emitted by a 1 MeV electron beam and its possible use as diagnostic tool*, Nuclear Instruments and Methods in Physics Research Section A: Accelerators, Spectrometers, Detectors and Associated Equipment **357**, 231 (1995).

[50] P. Karataev *et al.*, *Experimental observation and investigation of the prewave zone effect in optical diffraction radiation*, Physical Review Special Topics-Accelerators and Beams **11**, 032804 (2008).

[51] *International Linear Collider*, `https://ilc.kek.jp/ATF2/`.

[52] V. Ginzburg, *Transition radiation and transition scattering*, Physica Scripta **1982**, 182 (1982).

[53] M. L. Ter-Mikaelian, *High energy electromagnetic processes in condensed media* (Wiley, 1972).

[54] P. Karataev, *Pre-wave zone effect in transition and diffraction radiation: Problems and solutions*, Physics Letters A **345**, 428 (2005).

[55] A. P. Potylitsyn, *Transition radiation and diffraction radiation. Similarities and differences*, Nuclear Instruments and Methods in Physics Research Section B: Beam Interactions with Materials and Atoms **145**, 169 (1998).

[56] T. Behnke *et al.*, *The International Linear Collider Technical Design Report-Volume 1: Executive Summary*, arXiv preprint arXiv:1306.6327 (2013).

[57] V. Verzilov, *Transition radiation in the pre-wave zone*, Physics Letters A **273**, 135 (2000).

[58] N. Shul'ga, S. Dobrovol'sky, and V. Syshchenko, *On transition infrared radiation by relativistic electrons in a thin layer of matter*, Nuclear Instruments and Methods in Physics Research Section B: Beam Interactions with Materials and Atoms **145**, 180 (1998).

[59] N. Shul'ga and S. Dobrovol'sky, *About transition radiation by relativistic electrons in a thin target in the millimeter range of waves*, Physics Letters A **259**, 291 (1999).

[60] S. Dobrovolsky and N. Shulga, *Transversal spatial distribution of transition radiation by relativistic electron in the formation zone by the dotted detector*, Nuclear Instruments and Methods in Physics Research Section B: Beam Interactions with Materials and Atoms **201**, 123 (2003).

[61] M. Castellano *et al.*, *Search for the prewave zone effect in transition radiation*, Physical Review E **67**, 015501 (2003).

[62] P. Karataev *et al.*, *First observation of the Point Spread function of optical transition radiation*, Physical review letters **107**, 174801 (2011).

[63] T. Aumeyr *et al.*, *Advanced simulations of optical transition and diffraction radiation*, Physical Review Special Topics-Accelerators and Beams **18**, 042801 (2015).

[64] M. Castellano, A. Cianchi, G. Orlandi, and V. Verzilov, *Effects of diffraction and target finite size on coherent transition radiation spectra in bunch length measurements*, Nuclear Instruments and Methods in Physics Research Section A: Accelerators, Spectrometers, Detectors and Associated Equipment **435**, 297 (1999).

[65] B. Bolzon *et al.*, *Very high resolution optical transition radiation imaging system: Comparison between simulation and experiment*, Physical Review Special Topics-Accelerators and Beams **18**, 082803 (2015).

[66] X. Artru, G. Yodh, and G. Mennessier, *Practical theory of the multilayered transition radiation detector*, Physical review d **12**, 1289 (1975).

[67] L. C. Yuan, C. Wang, H. Uto, and S. Prünster, *Formation-zone effect in transition radiation due to ultrarelativistic particles*, Physical Review Letters **25**, 1513 (1970).

[68] L. Wartski, S. Roland, J. Lasalle, M. Bolore, and G. Filippi, *Interference phenomenon in optical transition radiation and its application to particle beam diagnostics and multiple-scattering measurements*, Journal of Applied Physics **46**, 3644 (1975).

[69] A. H. Lumpkin *et al.*, *Optical-transition radiation measurements for the Los Alamos and Boeing free-electron laser experiments*, Nuclear Instruments and Methods in Physics Research Section A: Accelerators, Spectrometers, Detectors and Associated Equipment **285**, 343 (1989).

[70] C. Couillaud, A. Loulergue, and G. Haouat, *Electron beam transverse emittance measurement using optical transition radiation interferometry*, in *Proc. of the Fifth European Particle Accelerator Conference, Sitges (Barcelona)*, 1996.

[71] A. Cianchi *et al.*, *First non-intercepting emittance measurement by means of optical diffraction radiation interference*, New journal of physics **16**, 113029 (2014).

[72] R. Fiorito and D. Rule, *Diffraction radiation diagnostics for moderate to high energy charged particle beams*, Nuclear Instruments and Methods in Physics Research Section B: Beam Interactions with Materials and Atoms **173**, 67 (2001).

[73] X. Artru and C. Ray, *Interference and shadow effects in the production of light by charged particles in optical fibers*, Nuclear Instruments and Methods in Physics Research Section B: Beam Interactions with Materials and Atoms **266**, 3725 (2008).

[74] G. Naumenko, Y. Popov, and M. Shevelev, *Direct observation of a semi-bare electron coulomb field recover*, in *Journal of Physics: Conference Series* Vol. 357, p. 012005, IOP Publishing, 2012.

[75] K. Lekomtsev, *Investigation of Coherent Diffraction Radiation from a dual target system at CTF3 and its application for longitudinal bunch profile diagnostics*, PhD thesis, Royal Holloway, University of London, 2012.

[76] L. Bobb, *Feasibility of Diffraction Radiation for Noninvasive Micron-scale Transverse Beam Size Measurement in Circular Machines*, PhD thesis, Ph. D. Thesis, Royal Holloway, Univ. of London, 2016.

[77] M. Born and E. Wolf, *Chapter VIII - Elements of the Theory of Diffraction*, in *Principle of Optics*, pp. 370–458, New York: Pergamon Press, 1980.

[78] M. Castellano, *A new non-intercepting beam size diagnostics using diffraction radiation from a slit*, Nuclear Instruments and Methods in Physics Research Section A: Accelerators, Spectrometers, Detectors and Associated Equipment **394**, 275 (1997).

[79] P. Karataev *et al.*, *Application of optical diffraction radiation to a non-invasive low-emittance high-brightness beam diagnostics*, in *Quantum Aspects Of Beam Physics 2003*, pp. 111–118, World Scientific, 2004.

[80] A. Cianchi *et al.*, *Nonintercepting electron beam size monitor using optical diffraction radiation interference*, Physical Review Special Topics-Accelerators and Beams **14**, 102803 (2011).

[81] M. Bergamaschi *et al.*, *JACoW: Diffraction Radiation for Non-Invasive, High-Resolution Beam Size Measurements in Future Linear Colliders*, in *Proceedings of the Eight International Particle Accelerator Conference, Copenhaghen*, 2017.

[82] S. Kawabata *et al.*, *ATF Accelerator Test Facility: design and study report* (KEK, Tsukuba, 1995).

[83] KEK: High Energy Accelerator Research Organisation. `http://www.kek.jp/en/`.

[84] ATF Collaboration, K. Kubo *et al.*, *Extremely Low Vertical-Emittance Beam in the Accelerator Test Facility at KEK*, Phys. Rev. Lett. **88**, 194801 (2002).

[85] Y. Honda *et al.*, *Achievement of Ultralow Emittance Beam in the Accelerator Test Facility Damping Ring*, Phys. Rev. Lett. **92**, 054802 (2004).

[86] H. Braun *et al.*, *ATF2 Proposal: v.1*, CERN Report No. CERN-AB-2005-035, 2005.

[87] H. Hayano, *ATF Linac Commissioning*, KEK Report No. KEK-96-112, 1996.

[88] T. Okugi *et al.*, *ICFA Beam Dynamics Newsletter, No 61* (ICFA, 2013).

[89] H. Sakai *et al.*, *Improvement of Fresnel zone plate beam-profile monitor and application to ultralow emittance beam profile measurements*, Phys. Rev. ST Accel. Beams **10**, 042801 (2007).

[90] J. Alabau-Gonzalvo *et al.*, *The ATF2 Multi-OTR System: Studies and Design Improvements*, in *International Beam Instrumentation Conference*, 2012.

[91] Y. I. Kim *et al.*, *Cavity beam position monitor system for the Accelerator Test Facility 2*, Phys. Rev. ST Accel. Beams **15**, 042801 (2012), 1301.5561.

[92] P. Bambade *et al.*, *Present status and first results of the final focus beam line at the KEK Accelerator Test Facility*, Physical Review Special Topics-Accelerators and Beams **13**, 042801 (2010).

[93] T. Shintake *et al.*, *Design of laser-Compton spot size monitor*, in *Proceedings of the XVth International Conference on High-Energy Accelerators, Int. J. Mod. Phys. A (Proc. Suppl.) A* Vol. 2, pp. 215–218, 1993.

[94] J. Yan, *Precise Measurement of Nanometer Scale Electron Beam Sizes Using Laser Interference by Shintake Monitor*, Ph.D. thesis, University of Tokyo, 2015.

[95] A. Aryshev *et al.*, *Micron size laser-wire system at the ATF extraction line, recent results and ATF-II upgrade*, Nuclear Instruments and Methods in Physics Research Section A: Accelerators, Spectrometers, Detectors and Associated Equipment **623**, 564 (2010), 1st International Conference on Technology and Instrumentation in Particle Physics.

[96] B. I. Grishanov *et al.*, *ATF2 proposal Vol 2*, arXiv preprint physics/0606194 (2005).

[97] S. Franssila, *Anisotropic Wet Etching*, in *Introduction to microfabrication*, pp. 237–254, John Wiley & Sons, 2010.

[98] G. Kaminsky, *Micromachining of silicon mechanical structures*, Journal of Vacuum Science & Technology B: Microelectronics Processing and Phenomena **3**, 1015 (1985).

[99] G. T. Kovacs, N. I. Maluf, and K. E. Petersen, *Bulk micromachining of silicon*, Proceedings of the IEEE **86**, 1536 (1998).

[100] *Cornell Electron/Positron Storage Ring Test Accelerator*, `https://www.classe.cornell.edu/Research/CesrTA/WebHome.html`.

[101] *UV-visible polarizer*, `http://www.moxtek.com/wp-content/uploads/pdf-downloads/optics/datasheets/ProFluxUV1008.pdf`.

[102] *Pellicle beam splitter*, `https://www.thorlabs.com/thorproduct.cfm?partnumber=BP208`.

[103] R. Kieffer *et al.*, *Optical diffraction radiation for position monitoring of charged particle beams*, Nuclear Instruments and Methods in Physics Research Section B: Beam Interactions with Materials and Atoms **402**, 88 (2017).

[104] *Lens with focal = 250 mm*, `https://www.thorlabs.com/thorproduct.cfm?partnumber=LA4538`.

[105] *UV enhanced mirror*, `https://www.thorlabs.com/thorproduct.cfm?partnumber=PF20-03-F01`.

[106] *CCD intensified camera*, `http://pdf.directindustry.fr/pdf-en/pco-ag/dicam-pro/29533-93103.html`.

[107] *Motorized filter wheel*, `https://www.owis.eu/en/products/motorized-positioning-systems/produktgruppe/filterraeder/produkt/148/`.

[108] *Bandpass filters from Thorlabs*, `https://www.thorlabs.com/newgrouppage9.cfm?objectgroup_id=1001&pn=FB400-10#5413`.

[109] *Bandpass filter from eSource*, `http://www.esourceoptics.com/catalog/item/8093856/8732032.htm`.

[110] *Bandpass filter from Andover*, `https://www.andovercorp.com/products/bandpass-filters/standard/193-299nm/`.

[111] *Image intensifier unit C9547-04*, `https://www.hamamatsu.com/eu/en/product/type/C9547-04/index.html`.

[112] *sCMOS camera*, `https://www.pco.de/fileadmin/user_upload/pco-product_sheets/pco.edge_42_lt_data_sheet.pdf`.

[113] *Linear Stage 150mm*, `https://www.zaber.com/products/linear-stages/T-LSR/details/T-LSR150B`.

[114] *Qt Libraries*, `https://www.qt.io/what-is-qt/`.

[115] *EPICS*, `https://epics.anl.gov/`.

[116] G. A. Naumenko, *Synchrotron radiation contributions to optical diffraction radiation measurements*, Nuclear Instruments and Methods in Physics Research Section B: Beam Interactions with Materials and Atoms **201**, 184 (2003).

[117] P. Tenenbaum and T. Raubenheimer, *Resolution and systematic limitations in beam-based alignment*, Physical Review Special Topics-Accelerators and Beams **3**, 052801 (2000).

[118] *SAD, Strategic Accelerator Design*, `http://acc-physics.kek.jp/SAD/`.

[119] S. Bernal and D. Stratakis, *Emittance Measurement: Quadrupole Scan* (U.S. Particle Accelerator School 2008, University of Maryland, College Park, 2008).

[120] A. Green and Y.-M. Shin, *Implementation of Quadrupole-scan Emittance Measurement at Fermilab's Advanced Superconducting Test Accelerator (ASTA)*, in *Proc. IPAC 15*, 2015.

[121] R. Kieffer *et al.*, *Direct observation of incoherent Cherenkov diffraction radiation in the visible range*, Physical review letters **121**, 054802 (2018).

[122] T. Lefèvre *et al.*, *JACoW: Cherenkov Diffraction Radiation From Long Dielectric Material: An Intense Source of Photons in the NIR-THz Range*, in *Proc. IPAC 17*, 2017.

[123] T. Lefèvre *et al.*, *Non-invasive Beam Diagnostics with Cherenkov Diffraction Radiation*, in *Proc. 9th Int. Particle Accelerator Conf.(IPAC'18), Vancouver, BC, Canada, April 29-May 4, 2018*, pp. 2005–2008, JACOW Publishing, Geneva, Switzerland, 2018.

[124] J. Brossard, M. Desmons, B. Mercier, C. Prevost, and R. Roux, *Construction of the Probe Beam Photo-injector of CTF3*, in *Proc. of 10th European Particle Accelerator Conference" EPAC'06"*, pp. 828–830, 2006.

[125] J. N. Quirante *et al.*, *Califes: A multi-purpose electron beam for accelerator technology tests*, in *Proc. LINAC*, pp. 121–123, 2014.

[126] *CLEAR @ CLEX*, `https://clear.web.cern.ch/content/beam-line-description`.